Helically-Driven Dynamics in Granular Media

by

Andrew Thoesen

A Dissertation Presented in Partial Fulfillment
of the Requirements for the Degree
Doctor of Philosophy

Approved October 2019 by the
Graduate Supervisory Committee:

Hamidreza Marvi, Chair
Spring Berman
Heather Emady
Andrew Klesh
Hyunglae Lee

ARIZONA STATE UNIVERSITY

December 2019

ABSTRACT

Vehicles traverse granular media through complex reactions with large numbers of small particles. Many approaches rely on empirical trends derived from wheeled vehicles in well-characterized media. However, the environments of numerous bodies such as Mars or the moon are primarily composed of fines called regolith which require different design considerations. This dissertation discusses research aimed at understanding the role and function of empirical, computational, and theoretical granular physics approaches as they apply to helical geometries, their envelope of applicability, and the development of new laws. First, a static Archimedes screw submerged in granular material (glass beads) is analyzed using two methods: Granular Resistive Force Theory (RFT), an empirically derived set of equations based on fluid dynamic superposition principles, and Discrete element method (DEM) simulations, a particle modeling software. Dynamic experiments further confirm the computational method with multi-body dynamics (MBD)-DEM co-simulations. Granular Scaling Laws (GSL), a set of physics relationships based on non-dimensional analysis, are utilized for the gravity-modified environments. A testing chamber to contain a lunar analogue, BP-1, is developed and built. An investigation of straight and helical grousered wheels in both silica sand and BP-1 is performed to examine general GSL applicability for lunar purposes. Mechanical power draw and velocity prediction by GSL show non-trivial but predictable deviation. BP-1 properties are characterized and applied to an MBD-DEM environment for the first time. MBD-DEM simulation results between Earth gravity and lunar gravity show good agreement with theoretical predictions for both power and velocity. The experimental deviation is further investigated and found to have a mass-dependant component driven by granular sinkage and engagement. Finally, a robust set of helical granular scaling laws (HGSL)

are derived. The granular dynamics scaling of three-dimensional screw-driven mobility is reduced to a similar theory as wheeled scaling laws, provided the screw is radially continuous. The new laws are validated in BP-1 with results showing very close agreement to predictions. A gravity-variant version of these laws is validated with MBD-DEM simulations. The results of the dissertation suggest GSL, HGSL, and MBD-DEM give reasonable approximations for use in lunar environments to predict rover mobility given adequate granular engagement.

ACKNOWLEDGMENTS

I would first like to acknowledge my advisor, Professor Hamidreza Marvi, for his patience and guidance in transforming my dissertation into something I can be proud of. He helped me become an independent researcher, elevate my writing to an academic level, and execute my ideas with greater precision. Without him, I undoubtedly would not have completed my graduate studies and I am grateful he gave me the opportunity to do so. I would also like to thank the other members of my committee: Professor Spring Berman, Professor Heather Emady, Dr. Andrew Klesh, and Professor Hyunglae Lee for their feedback and helpful comments during my dissertation work. I acknowledge fellow PhD students Hosain Bagheri, Mahdi Ilami and Reza Ahmed and the other members of the BIRTH Lab for the support I received at various times over the last few years. I thank my wonderful undergraduates who joined the various projects which contributed to this work: Sierra Ramirez, Teresa McBryan, Darwin Mick, Marko Green, and Justin Martia. Their tireless dedication helped make this possible.

Countless colleagues from across the country during this journey have been instrumental to shaping my outlook as a researcher. I thank all of the members of NASA Kennedy Space Center's Swampworks Lab for the experience of working with RASSOR to learn about lunar mining robotics and for the BP-1 which made later experiments possible. Gratitude is also given to Caltech's Jet Propulsion Laboratory, particularly their Machine Learning and Instrument Autonomy Group and Robotic Vehicles Group. I am indebted to Jack Lightholder for the opportunity to experience JPL firsthand and his advice regarding that esoteric landscape. I thank Dr. Lukas Mandrake for our varied conversations but especially those regarding physics. His appreciation for exactness influenced my view of terramechanics and brought me to

emphasize the later approaches in this work. Thanks also goes to Kalind Carpenter for our discussions about screw propelled vehicles and his enthusiasm for unique robotic craft. A final professional thank you goes to the School of Earth and Space Exploration and then-Director Elkins-Tanton, who gave me a research home for two years and allowed me to learn and enjoy the wonders of space robotics.

My encounters with the general public have been formative as well; in particular, I thank the Arizona Space Grant Consortium for funding the ASU-NASA Spacegrant Fellowship which gave me an opportunity to teach science to that public. I thank Heidi Cocco, my mother-in-law and teaching partner, for her classroom leadership in making that project possible. The two 8th grade classes at Greenway Middle School deserve my gratitude as well, for their enthusiasm and excitement. You've reminded me that science ought to be done in service to others. You are incredible students, and I know you are capable of great things. I would also like to thank every barista, too numerous to list, I encountered at Cartel Coffee Lab and Maverick Coffee over the past six years for our various discussions about both science and life. These places became a haven to me, as indispensable to writing and thought as the laboratory became to experiments.

I want to thank my family for the love and support I've been given over the last 32 years. The people I count as family has grown beyond count, and for that I am fortunate. Thank you Aunt Cindy, Uncle Russ, Conor, and Grandma Thoesen for your support, and especially my parents Rebecca and Daniel Mahoney. You instilled the spirit of caring and the spirit of hard work in me. As a new father, I now understand the challenge I gave you and am grateful for what you did for me. My friends from Chesterton High School, Purdue University, and ASU have all helped me in some way during this journey but I want to particularly thank my oldest friend, Brandon

Patterson, for everything during the last few decades and especially his assistance in attending and navigating graduate school. I thank my in-laws Heidi Cocco, Hikmat Ahmad, and Oma for their love and assistance with my son, without which this dissertation would have never been finished.

Finally, I acknowledge the love and support of my wife, Omaya Ahmad. Our serendipitous meeting on that August day has assuredly changed my life and myself for the better. From the first day of graduate school to my defense, I've had your selfless support. You have been my rock during this entire process and I am grateful every day to have you in my life. You're my favorite. I am grateful for our son, Osiris Hikmat Thoesen, and I thank him for the boundless drive and energy he has given me. He reminds me what all of this is for: a better life for him and every member of future generations.

TABLE OF CONTENTS

LIST OF TABLES

LIST OF FIGURES

Figure Page

Figure Page

Figure Page

Chapter 1

INTRODUCTION

1.1 Space Vehicles and Screw-Propelled Vehicles

There is a long-standing interest to better understand mobility for granular environments within both the robotics and granular physics community. Robotic limbed intruders and mobile craft often have to contend with physical laws which seem to blur the line between solid and liquid surfaces and are not well defined. This complexity is further compounded by the variety of granular materials which exist. Characteristics such as particle size, angularity, and homogeneity of mixture can result in significant changes to observed laws and require fit parameters. Improvement of robot and craft performance in granular media relies mostly on experimental observation. The field of space exploration in this area continues to develop, encompassing the advancement of mining and transportation machinery. Landers on bodies with similar gravity to Earth, such as Mars or the Moon, have a high rate of success. Historically, lander mobility solutions have often used wheeled or tumbling approaches in these environments. This work addresses the static forces and dynamic movement of bladed geometries in simulation and experiments for geologically similar environments to space bodies. It also applies analytical methods from the literature in reduced gravity simulations and with geologically similar environments. The result is an expansion of understanding craft dynamics in both Earth systems and off-planet.

The transportation of granular material and vehicles through granular media is often referred to as Terramechanics. It is a discipline which encompasses various

sectors. Bladed geometry can provide either material transport, such as pharmaceutical powders and mining materials, or craft transport itself, such as in the arctic, marshes, or clay fields. In these applications, helical blades dynamically transform a rotational force into a translational one, propelling matter in otherwise difficult situations. Although experimental data for each individual application often exists, there remains a need for investigation into broader analytical and simulated design solutions. The field of focus for this work is space and the second half of the dissertation examines results in BP-1, a physical lunar simulant obtained from NASA Kennedy Space Center, which provides an opportunity to evaluate granular physics laws in a lunar analogue. An additional difficulty in grain-geometry interaction is applying established granular physics law to atypical shapes or materials. Much of terramechanics is empirical, based upon wheeled movement, and imposes certain limitations which restrict utility for smaller wheels, smaller craft, or certain environmental characteristics. Expanding generalized granular physics to atypical characteristics will aid in design of future rovers.

1.2 Empirical, Theoretical, and Computational Mobility Models

Advancements in computational power have made detailed simulations of mobile craft in granular media a more realistic possibility. A class of software called discrete element method (DEM) models each individual particle. Combined with multi-body dynamics (MBD) software, it provides an opportunity for designing and testing robotic craft. However, there are few studies which experimentally compare MBD-DEM results with data for dynamic, moving craft. This dissertation addresses the work of creating applicable data with characterizable difference in environmental conditions between

experiment and simulation. The work does so while using the three-dimensional helical intruder of a screw and with the technique of Young's modulus reduction. This contrasts with the many uniform intruders tested in the literature because helical objects have a significant asymmetrical component of shear force and movement. The two analytical methods evaluate are Resistive Force Theory (RFT) and Granular Scaling Laws (GSL). RFT uses a generalized model of empirical trends applied to simple intruders in granular media. GSL uses non-dimensional analysis (NDA) to predict effects between pairs of wheels with identical shape but varying size, mass, and speed. There exists experimental validation for both of these techniques in the literature when applied to narrow cases, but neither has evaluated screw shapes.

1.3 Contributions of this Dissertation

The objective of this research is to identify and model the necessary mechanics of helical motion in granular media by experimental, theoretical, and computational means with the end goal of predicting dynamics of a screw propelled vehicle in Earth and lunar gravity. The scope of the work is intended as a study of the performance of an SPV in baseline media (such as glass beads or silica sand) and relevant media (such as BP-1) environments. It is also intended as a study of the specific BP-1 material as applied to MBD-DEM simulations and current analytical solutions. Finally, it aims to better understand the theoretical granular physics behind dynamics of helical interactions with granular media. The novel contributions of this work can be summarized as follows:

1. A direct comparison of static, screw-generated force in glass beads with DEM simulations showing general agreement and a direct comparison of dynamic,

screw-generated mobility in glass beads with MBD-DEM simulations showing general agreement is made. These comparisons show that differences between experiments and stiffness-reduced MBD-DEM simulations for screws are characterizable and consistent. They also show why resistive force theory plate approximation cannot be applied to double-wound helices in granular media due to non-additive characteristics of the granular flow.

2. An investigation of wheeled granular scaling laws is performed for the first time with free dynamic movement, straight and helically grousered wheels on a two-motor lightweight rover, and in a lunar analogue (BP-1) for direct comparison with silica sand. Previous literature assessed single sandpaper wheels on an overhead gantry with an order of magnitude higher masses. Performance of mechanical power draw and velocity prediction by GSL are assessed and show significant, but predictable, deviation in power with more predictable velocity results in silica sand than BP-1.
3. Mass-dependant power prediction deviation in GSL is further investigated with three pairs of masses on grousered and sandpaper wheels and found to have a mass-dependant functionality driven by granular sinkage and engagement. The results can also be seen as a weak function of rotational wheel speed, likely due to inertial effects.
4. BP-1 properties from both literature and in-lab experiments are applied to an MBD-DEM environment for the first time. Three dimensional MBD-DEM simulation results between Earth gravity and lunar gravity for gravity-variant GSL are performed for the first time and show good agreement with theoretical predictions for both power and velocity.

5. A derivation and validation of helical granular scaling laws by non-dimensional analysis is performed. This is done at light masses for which a wheeled rover showed significant errors but a screw-propelled rover shows close general agreement in both power and velocity.
6. An evaluation of a gravity-variant version of HGSL is performed at lunar gravity with BP-1 granular properties applied in a three-dimensional MBD-DEM cosimulation. Results show even closer agreement than experiments.

1.4 Organization of this Dissertation

This section outlines the contents described in various chapters of this dissertation. The remainder of the document is organized as follows: Chapter 2 provides a background of related work for granular mobility. This includes robotic form factors and the empirical, theoretical, and computational techniques used. Chapter 3 examines static screw-generated forces in granular media and how the flow characteristics of the geometry inform the approach to characterizing it. Chapter 4 examines helically-driven granular mobility and gravity-variant scaling relations, which helps make a determination as to the theoretical framework for the remainder of the dissertation. Chapter 5 assesses the predictive performance of granular scaling laws for lightweight wheeled rovers, giving insight into the applicability of laws for a lunar analogue and MBD-DEM performance of such laws. Chapter 6 revisits the scaling laws for robotic mobility in granular media by way of mass variation, and reveals a new significant dependence of scaling law on mass not previously reported. Chapter 7 introduces

the helical granular scaling theory and experimental validation of the law in lunar simulant. Chapter 8 summarizes the conclusions of the document and future work.

Chapter 2

BACKGROUND AND RELATED WORK

2.1 Surface Exploration in the Solar System

Figure 1. Three Types of Lunar Mobility Approaches Including Screws

This work began with a study of mobility in lunar and small body regolith. Regolith is a general term used for the classification of dusty, fine particles which cover planetary and smaller bodies in the solar system. While investigating possible solutions to excavation or mobility, atypical mobility form factors were considered

for the unusual environment. This led to the central question of the current work: what role, if any, do counter-rotating screw systems have for excavation or mobility in space?

As early as the 1960's, screw-propelled vehicle (SPV) designs were investigated for use on Earth in unstable or uncertain environments. One early example of SPV's was the Marsh Screw Amphibian [1]. This craft propelled itself through water and then quickly transitioned to a solid, muddy environment. Modern takes on the amphibian nature have focused on lake shore environmental monitoring [2]. Another similar vehicle is the Amphirol [3]. This vehicle is capable of navigating through sticky wet clay, a nearly impossible task for other forms of transportation. The Arctic is another example of a demanding environment. An SPV called the ZIL-2906 was used to retrieve Soviet cosmonauts. A modern vehicle called Snowbird-6 utilized screw pontoons for travel in water-ice areas of the arctic, although it also used treads for longer stretches of solid ground.

The above unique environments require extreme design considerations which share traits to the unpredictable surfaces of many bodies in the solar system. Unlike treaded or belted vehicles, SPV's are relatively simple and lend themselves to using more robust, space-faring materials. Space systems necessarily rely on simplicity and well-tested legacy approaches; this was seen as an opportunity to expand the latter. The dominant approach to bodies with a gravity field within one order of magnitude of Earth's (such as Mars and the Moon) has been to use wheeled systems. While the wheel tread designs themselves are typically unconventional, the underlying dynamics of the system have been similar to those on Earth. Although the Soviets' Lunokhod-1 was the first successful space rover, most Americans will be more familiar with the Lunar Roving Vehicle seen in figure 3. Work on this vehicle included the development

Figure 2. Example of the ZIL-2906 SPV for cosmonaut rescue in Siberia

of a new style of mesh wheels and also explored other mobility approaches [4] including screw-powered vehicles as seen in the previous figure 1. At the time, it was uncertain that the terrain could support wheeled mobility.

Current lunar research now includes investigating what kinds of large-scale mining and exploration systems may be useful. Modern development of such systems can be exemplified by RASSOR [5] as seen in figure 4. This robot uses a bucketwheel system to both excavate and transport material. Its design is centered around the advantage of counter-rotation for excavation by using two wheels which rotate in opposite directions The work in this dissertation is meant to compliment these solutions and analyze how a screw shape can contribute to such technology.

Low-gravity designs for small bodies use primarily hopping or tumbling motions. Because of the difficulty in approaching these types of systems, there have only been

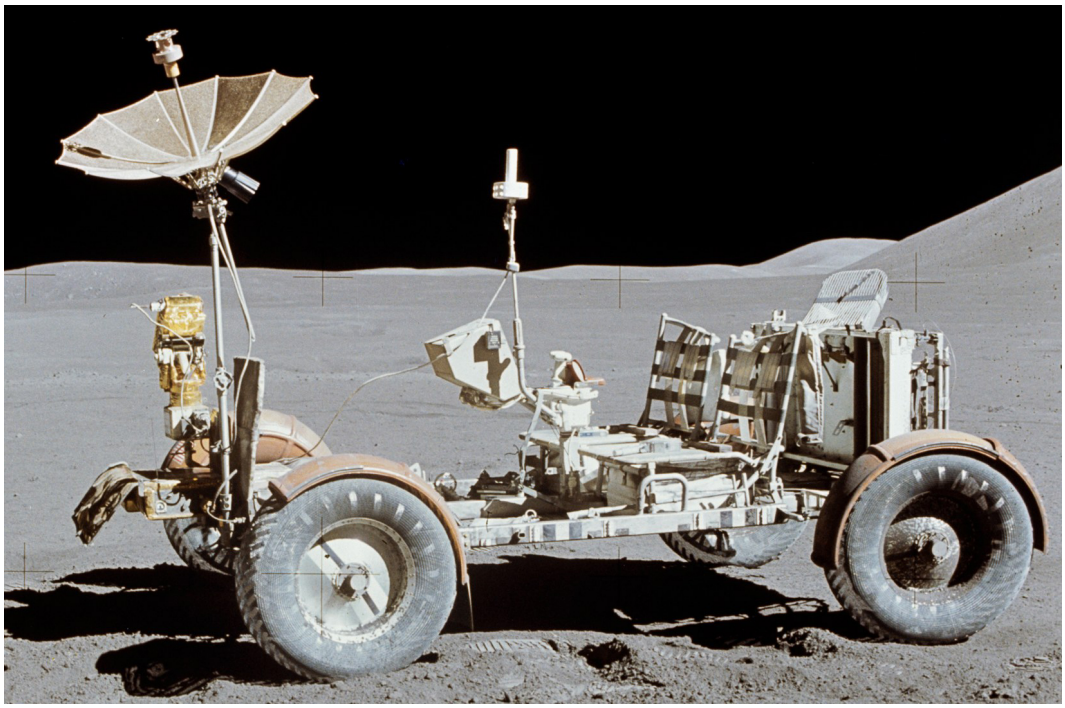

Figure 3. Lunar Rover From the Apollo 15 Mission

five attempted missions at small-body landing. One did not proceed due to loss of contact (Phobos 2). The first successful touchdown was NEAR-Shoemaker [6], an immobile orbiter which continued to collect data. The next was Deep Impact, which impacted a comet in its "landing". Directly following this was the Hayabusa mission[7]. This saw not only an immobile lander, but the first attempt at small-body mobility with the MINERVA robot. This 0.6 kg tumbler was meant to hop across the surface and take pictures, but deployment error sent it into space. The Rosetta mission [8] and its Philae landing probe were designed to shoot harpoons into the surface of the 67P comet, settle into its designated area, and perform several science goals. Instead, the harpoons failed to fire and the probe bounced, entered a shadowed crater, and landed on its side. This series of events resulted in quick loss of power. Recently launched missions include OSIRIS-REx [9] and Hayabusa-2 [10] sample return

missions. Discovery-class missions of Psyche [11] and Lucy [12] also focus on small body exploration. Of those listed, only Hayabusa-2 has landers, which successfully deployed September 21, 2018. This highlights the need for more solutions to surface mobility.

Figure 4. RASSOR Robot at NASA KSC

Alternate designs to granular mobility can include peristaltic or waveform motion as found in snakes and worms [13, 14, 15, 16] but the complexity likely makes them prohibitive for space applications. Other related research includes efforts into asteroid anchoring technology such as ATHLETE [17, 18] and microspine grippers [19, 20] aimed at attaching to rocky surfaces. In current research, the most popular form of small-body mobility is still hoppers or tumblers[21] [7, 22, 23, 24, 25]. These typically use internal flywheels such as the MINERVA attachment previously mentioned in the Hayabusa mission. New generation HEDGEHOG or HOPTER [23, 24] provide similar

designs. They are found to be simple and energy efficient forms of transportation due to the low gravity of the body. The simplicity which increases chances of success also introduces limitations to discrete control or risk of impact. In this context, one goal of the work is to examine whether an added amount of complexity in the form of an SPV may result in a well-characterized, predictable, dynamically controllable craft which acts as a rover form factor in a wide range of gravity fields.

Mobility in granular media poses challenges due to the complexity of the material, even for wheeled mobility. These challenges are compounded when the granular media has not been well characterized as many terramechanics models use material-specific "fit parameters" from empirical data. These issues are further aggravated with the additional challenges of space environments. The impact of mass, size, and shape on mobility performance has been the subject of previous field research for both Earth and space mobility systems in sandy granular media, but especially lunar and Martian traversing [26, 27, 28]. Recent developments, such as the Axel-DuAxel-Moondiver concept rovers [29, 30] developed by the Jet Propulsion Laboratory, investigate extreme terrains found in canyons and fissures. These rovers have demonstrated mobility in fields of scattered rocks covered with granular media. Other wheeled robot examples for this purpose include ATHLETE, a wheeled platform for a variety of different exploratory purposes [31, 17, 32], TRI-STAR, a three-wheeled, multi-modal exploration robot designed for the regolith of the moon [33], RIMRES, an integrated multi-robot package designed for easy adaptability [34], and the aforementioned RASSOR. Application of granular physics theory to the target environments would be helpful to improve the design of such robots. It is valuable to examine wheeled rover mobility in parallel to SPV's to understand in what ways a screw geometry may compliment current rover design.

In this dissertation, all techniques are discussed using lightweight robotics. These are often used in practice for space robotics and in labs for prototype and development. Sojourner [35], the Mars rover, is an example of such a class of robot at approximately 11 kg. Prayan, the rover from the Chandrayaan-2 mission [36], is 27 kg. With 6 wheels each, the per-wheel mass weight would be 1.8 kg and 4.5 kg, respectively. Other rovers around this class are the 10 kg Moonraker design [37]. PUFFER [38, 39] is a sub 1 kg rover design; reconfigurable or multi-robot schemes often include light rovers [34]. Some potential use cases on Earth are laboratory developments of new grouser approaches [40], angled granular mobility [41], or other field robotics applications [42]. Whether for space or field robotics, there is a need to understand how lightweight prototypes or rovers may deviate from established granular scaling laws.

This work aims to evaluate a lightweight SPV in a cohesive granular environment similar to that of target environments, determine if counter-rotating screws achieve successful mobility and if so, under which gravitational strengths. Screw geometry results will be compared to literature results and tests in well-characterized media to answer questions about whether certain granular physics approaches can be applied. The work therefore addresses two items simultaneously. The first is testing a novel mobility solution for target environments. The second is an evaluation of newly developed approaches for granular media relevant to this topic.

2.2 Granular Testing Environments

Many granular media experiments are done with a common materials such as quartz sand or artificial materials such as glass beads. The work's initial tests with

glass beads were designed to give an evaluation of simulation techniques and then perform further research using a material which more closely resembles regolith.

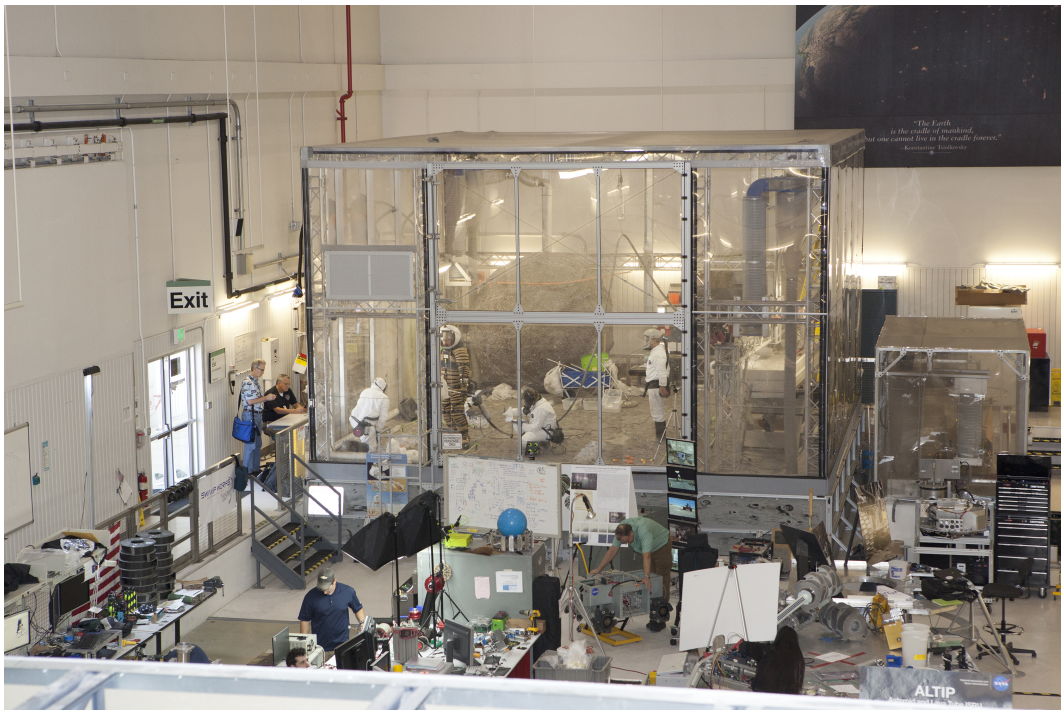

Figure 5. NASA Kennedy Space Center's BP-1 Testbed

Bodies with most successful lander missions (Mars, the Moon) have gravity of the same order of magnitude as Earth. Small bodies in the solar system often have gravitational fields several orders of magnitude smaller than this. Regolith is hard to characterize because of the limited encounters had with space bodies; each body will have a slightly different composition. To experiment with robotic designs and predict interactions with the environment, the astrogeology community creates "simulants" which are aimed at mimicking certain aspects of the regolith. For example, a chemical simulant may react differently to physical disturbance but replicate chemical reactions with high fidelity. Likewise, a physical simulant may not imitate chemical properties but will be a close approximation for predicting physical reactions of regolith, using

measures such as bulk density and particle similarity. In this work, all simulants referenced are physical simulants. Test beds of physical simulants exist at NASA facilities and universities but are relatively uncommon.

A modern example of this which informs the work is the test bed at NASA's Kennedy Space Center (KSC) in the Granular Mechanics and Regolith Operations (GMRO) Lab. This lab and the testing environment are colloquially known as Swampworks and the "Big Bin" respectively. The lunar simulant used in this dissertation, Black Point 1 (BP-1), was obtained from GMRO Lab at KSC. The simulant is made from the Black Point basalt flow in the San Francisco Volcanic Field and shares close characteristics to lunar regolith as detailed in geotechnical assessment [43]. This is the lunar simulant NASA uses at KSC for testing lunar robotics such as RASSOR and in the robotic mining competition [44, 45]. The important characteristics of BP-1 highlighted for the purposes of this work are:

1. Classification as a silty sand with A D60 value of 0.11 mm and D30 value of 0.055 mm, that is 60% of particle sizes are finer (smaller) than 110 microns and 30% smaller than 55 microns.
2. A classification of particle shape in the angular to sub-angular category
3. An internal angle of friction between 39-51°, somewhat dependant on density

The result of the above properties is a granular media that, while not cohesive, may appear to be due to high inter-particle friction forces. The BP-1 simulant has been identified as a closer physical analogue to lunar regolith than many experimentally developed simulants [46, 43] and was in relative abundance due to its existence as a mining byproduct. The difference in composition (and by extension, soil behavior) compared to a common media such as silica sand adds both novelty and value to experiments and better informs testing capabilities for space robotics.

However, even with a relevant simulant, experimental studies of these environments cannot provide all of the possible insights and may introduce unknown side effects. For example, testing reduced gravity dynamics with techniques such as weight-offset on Earth may not take the difference of gravitational compaction of grains into account[47, 48] and produce erroneous and even opposite results to parabolic flight gravity variation. But, parabolic flights are often expensive and inaccessible. A reliable analytical or computational tool can help with the design process. To better understand insights gained from these experiments, the work adds simulations and recently developed analytical approaches.

2.3 Simulation Approaches for Robotic Interaction with Granular Media

Discrete Element Method (DEM) simulations create a simulated environment where each particle is individually modeled. The particle movement and reactions within the environment are driven by a selected physics model and various qualities. Comparative results between DEM simulations and experiments can vary widely. It is necessary to identify what granular media qualities are essential for a particular comparison. Experimental validation studies between DEM simulations and granular media experiments mainly focus on two aspects: either the flow patterns of the granular material [49, 50, 51, 52, 53, 54, 55] or the generated reaction forces of a variety of machines. Much of the literature focuses on the tumbling and mixing patterns of drums or other rotating items [56, 57, 58, 59]. Others study blending and mixing [60, 61, 62, 63] machines. Flow patterns for relatively small particles in hoppers have been shown to be accurately simulated [64]. Utilizing screw conveying of both powder and beaded material is another topic of interest in the literature [65, 66, 67, 68, 69, 70].

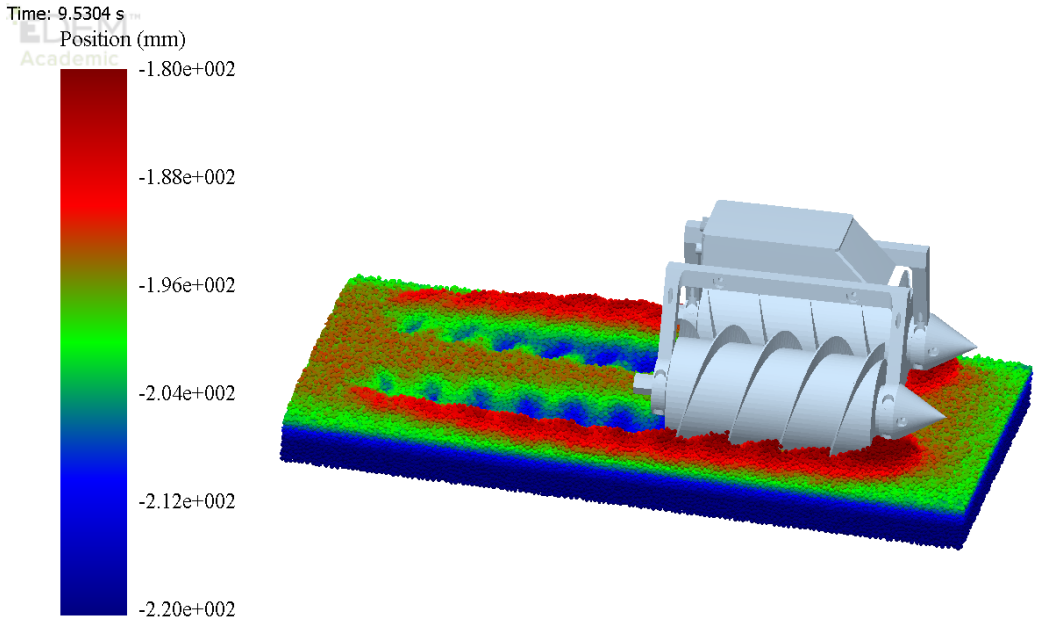

Figure 6. DEM Simulation from an Isometric Point of View

However, errors can occur from various causes. Recent cone crusher comparisons showed only slight variation in the size distribution of produced rocks between simulations and experiments [71] but the power draws of the rock crusher had significant error. Likewise, pellets evaluated in DEM utilizing a variety of parameter combinations showed that several combinations produced good comparisons for a rotating drum [72]. The upper and lower angles of repose during rotation matched well to experiments but DEM significantly overestimated particle velocities near surface level. DEM has also been used for comparisons with non-cylindrical drums [73]. In another drum experiment, fluid approximation resulted in good match for speed but pressure and particle front showed difference [74]. Wall smoothness can change frictional effects and introduce significant differences between experimental and DEM results in terms of flow patterns and forces [75, 76, 77]. Other uses of DEM include testing deformable materials [78, 79, 80], evaluating the dynamics of additive manufacturing [81, 82] and particle beds [83], or assessing the physical properties of a new material [84]. It has

also been used to analyze jamming/packing problems [85, 86] or evaluate granular properties of shapes [87]. In one case, it was used for both, showing that helical textures on the inside of pipes transporting granular media help evenly distribute mass flow and prevent jamming events[88]. Experimental comparison is key.

Different granular intruders have been successfully simulated when compared to experiments [89]. Particles of similar size to the work (1-3 mm) have been simulated in many ways [90, 91, 92, 93] as have glass beads specifically [94, 95]. There has been recent work done in the literature which shows DEM has some success replicating physical simulants [96, 97]. There is also recent evidence that forces from very small particles can be successfully replicated using groupings of larger particles when utilizing the right parameters and staying within certain scaling limits [98, 99]. The current work aims to expand on this using a different intruder and different material, with the DEM simulations and varied gravity adding another dimension of novelty. Another simulation type, multi-body dynamics (MBD), evaluates the solid bodies or links of a dynamic system and the joints that restrict their relative motion, and how they react to internal and external forces. It can provide tools to study systems which are too large to test [100], have conditions that would be difficult to replicate [101], or would be prohibitively expensive to pursue initial prototypes. DEM has also been combined with other methods such as finite element modeling (FEM) to evaluate deformation in shot-peening [102] or powder compaction [103]. In this dissertation, DEM and MBD have been co-simulated to replicate both granular and craft dynamics. Validating such results in Earth gravity can provide better insight to reduced gravity simulations.

2.4 Characterizing BP-1 for Simulations

Since many DEM simulations (including the software used in this dissertation) are based on Hertzian contact and spheres, shapes must be approximated by composing overlapping spheres. Some calibration procedures have focused on evaluating the necessary complexity of these shapes with procedures of manually investigating particle shapes and creating clumps accordingly [104]. While this was done for particle diameters of 10 mm or more, the principles can be applied to microscopic shapes. The results in the literature show that particles comprised of more spheres tend to have less volumetric error. The average error of a single sphere and dual, four, and eight sphere clumps is 20%, 10.9%, 6.5%, and 4.6% respectively. This trend is in agreement with other literature [105] which shows single perfect sphere models significantly deviate in force and torque values from aspect ratio 1.1 or higher. The decision was therefore made to use 2-sphere clumps for elongated particles and 4 sphere clumps for pyramidal or tetrahedral particles and apply the geotechnical testing of the simulant from the literature [43] and to DEM models as best as possible.

While the BP-1 particles are largely around 100 microns or below, there have been studies which show that scaling small cohesive particles up to an acceptable size for simulation can result in accurate predictions of forces on agricultural tools at a macroscopic level [99]. Ideas similar to this have been explored recently by evaluating the flowability of JSC-1 lunar simulant using CFD-DEM coupling[96]. This study utilized a "course graining" technique of increasing particle size, something which becomes necessary when simulating particles of this size in a DEM environment. The limits of DEM aggregate modeling have found that deviations in soil occur only when scaling is exceedingly large[98]. While drawbar pull and slippage data between DEM

and experiments has been compared [97], other proposed mobility characteristics have not.

The ability of particles to scale is highly dependant on the application [106] as well. Very recent work shows that while rotating drum calibration tests can match scaled particles up to x4, a hopper flow only retained accuracy up to 2.5 and revealed that for industrial applications concerned with accuracy of flow, using particle scaling above this was inadvisable. Interestingly, similar scale-up for a screw conveyor showed that x4 scale-up did not influence flow rate. A series of evaluations of tillage forces and torques in the literature using simulated soil media implicates flexibility for this work's application. Initial studies introduced plastic deformation to the soil mechanics via Hysteretic Spring Contact model and found the plastic deformability of the soil was accurate to experiments and estimated how friction values would need to change to keep similar results with larger, upscaled particles [107]. A DEM simulation of sandy loam soil with estimated particle range of 0.032-1 mm simulated using 10 mm radius particles with a range of 0.95-1.05 of the mean radius showed good correlation between simulation and experiment to predict forces on a sweep tillage tool for a range of geometries [99]. This experiment did not find it achievable to match the bulk density due to the unusually large particle size. However, another study by the same group sought to pursue this technique of bulk density matching [108] in adhesive/cohesive wetted soil by increasing particle density. This study found high accuracy in the sweep tillage tool at speeds up to 12 km/h for the 400 mm by 32 mm geometry. It also explored using simple planar compression in another study to compress the particles of real density into the correct bulk density [109] for a similar geometry. Most similarly, this problem has been studied closely by those in the space community for rover mobility [110]. It concluded that poly-ellipsoid particles

would better mimic soil reactions than tri-sphere, but the application was focused on high slippage conditions. It also used a mono-dispersed particle sizing, lessening the interlock effect, and used 4 mm radii spheres which would result in a roughly 1 cm particle. It also dealt simultaneously with greater sinkage due to the softening of particles will small shear modulus (0.05 GPa).

To reiterate, the ability to scale particle size accurate depends a great deal on the application. It appears particularly relevant whether or not the targeted results are based more on geometry reactions (i.e. forces and movement) or the rheological reactions (flow in a circular or linear fashion). For vehicular applications it seems that the dominance of the force/mass balances in the scenario means that the primary concern is correctly recreating the bulk density and friction characteristics.

This was the approach chosen for several reasons. The first was to preserve using as many accurate particle properties as possible. The second was to give greater flexibility in increasing particle size. Any attempt to simulate a powder via coarse grain will necessarily be at unrealistic sizes. By saving computation time in particle size, this allows the use of a higher Young's modulus. That creates particles which are less "squishy" for the simulation, and have better bearing strength for vehicles. The choice of BP-1 particle size was motivated by striking a balance between factors needed to decrease simulation time. These particles are still relatively small to the geometry of the vehicle and while larger particles may disrupt granular flow, the bulk density was determined to be the more important factor for the results sought. Many geotechnical characteristics of BP-1 have been evaluated, including bulk density at various depths. The characteristics are listed with explanations as follows:

Poisson's ratio and Young's modulus are both taken from basalt characteristics [111] with the modulus reduced. Bulk density is taken from BP-1 geotechnical

Table 1. Properties of simulated BP-1, ABS, and interactions

Material Property	**BP-1**	**ABS**
Poisson's Ratio	0.25	0.35
Density (kg/m^3)	3150	1070
Young's Modulus (MPa)	73	1800
Interactive Property	**BP1-BP1**	**BP1-ABS**
Coefficient of Restitution	0.8	0.8
Coefficient of Static Friction	0.56	0.57
Coefficient of Rolling Friction	0.07	0.17
Other Properties	**Value**	
Size of Bisphere clump	3 mm	
Size of Tetrasphere clump	3.75 mm	
Simulation Timestep	9.6E-6 s	

assessment [43]. The friction of basalt on basalt is affected by the glass content of the rock. Because the black point lava flow has relatively high glass content, the friction values for glassy basalts in the literature is used. Coefficient of restitution for basalt is roughly 0.8 which makes sense for a glassy rock and coefficient of restitution tests with plastics were use for the value of BP-1 on ABS [112]. Frictions and CoR were taken from basalt-basalt interactions in literature [113, 114]. BP-1 on ABS properties were evaluated by in-lab testing. Together, the above properties were determined to strike the best balance between accuracy of simulations and computational time.

2.5 Analytical Approaches for Robotic Interaction with Granular Media

Terramechanics as a field tends to favor empirical or semi-empirical approaches. This was the precedent set by Bekker [115, 116] including for lunar mobility [117]. Later Wong [118] made advancements in examining many different soil-geometry models, including those with gravity variation. For example, rover weight-offset testing for space applications can have erroneous and at times even opposite results

to identical experiments in parabolic testing [47] due to the gravity compaction of grains. Recent efforts have been assisted by integrated wheel sensors [119] or predictive algorithms [120], but the broadest solutions will be design-independent. There are various characteristics such as particle size, size distribution, angularity, material composition, and homogeneity of mixture which can limit the utility of empirical laws or require additional complimentary tests for fitting parameters.

In recent years [121], the emergence of more holistic understanding of granular-geometry interaction has occurred. One example is the newly developed granular resistive force theory (RFT), an examination of granular material reactions [122, 123, 124, 125, 126, 127, 128, 129] driven by the fluid dynamic theory of the same name. Granular RFT decomposes bodies into a collection of plates or cylinders to sum the resultant forces for analysis. However, it will not yield accurate results with a rotating screw as expected due to violation of the fundamental assumption about non-disruptive flow. This is explicitly shown in chapter 3 using comparative DEM simulations showing the sum of two single bladed screws is significantly greater than one double-bladed screw with identical dimensions. RFT has been recently reconciled with more theoretical granular physics by assuming the target environment to be a continuum obeying certain characteristics [130, 131, 132, 133, 134] that allow for non-dimensional analysis of the movement of craft in that environment. Evidence suggests that RFT and continuum approaches can be explained by plasticity theories [133] and both have also been experimentally validated [134, 127] for their respective scenarios. The above non-dimensional analysis yielded a new set of granular scaling laws based on this continuum theory which have been successfully tested and applied to arbitrarily shaped wheels as well as DEM simulations of gravity variation [134]. By direct scaling of various parameters such as size and mass, certain outputs such

as velocity and power for larger wheels of the same general shape can be predicted from smaller ones. The advantage of exploiting these non-dimensional parameters is the ability to extrapolate performance of fully-sized field craft from smaller prototype versions without apriori knowledge of soil characteristics. This gives greater flexibility to initial testing of designs. These laws include a gravity variant version, and hold great potential for the development of field robotics and space robotics in particular. There is a valuable opportunity to evaluate various scenarios for such powerful laws and determine their feasibility. These laws, and extensions developed in this work, will be further explored in their respective chapters.

Diverting to a more specific area, there are recent notable developments which explore helical motion within granular media. The first case studies helical propulsion and the effects of geometry, granular confinement pressure, and external load [135]. By deriving an expression for helix speed as a function of the tangent and normal forces, an optimal helix angle identified for this locomotion case. This optimal angle was experimentally verified during original findings and the driving anisotropic forces identified. A second study [136] examined geometry of helix angle, length, diameter, and two different medias. This study showed similar optimal helix angle results with both glass bead and mustard seed experiments. In both studies, two distinct differences from this dissertation are present. First, the helical intruder is modeled as a collection of slender cylinders, based upon a wire geometry with $L >> d$ instead of a screw, with analyzed forces decomposed into normal and tangential. Second, the helical intruder is submerged fully in the granular media and moved through the medium instead of mobilizing over the surface. Hence, while there are theories about helical geometry in granular media, the expansion of non-dimensionalized power and velocity prediction of a dual screw propelled craft, reconciled with wheeled GSL, is

novel. To better understand the relationship between intruder and granular media, the work now details its current contributions and planned future contributions. The first of these is the experimental validation of static screw forces in a DEM simulation.

Chapter 3

SCREW-GENERATED FORCES IN GRANULAR MEDIA: EXPERIMENTAL, COMPUTATIONAL, AND ANALYTICAL COMPARISON

3.1 Abstract

This study presents an experimental, computational, and analytical comparison of a submerged, double-helix Archimedes screw generating propulsive force against a bed of glass beads. Three screws of different pitch lengths were studied. Each screw was tested at six speeds in approximately ten trials for a total of 180 experimental trials. These experiments were then replicated in EDEM, a Discrete Element Method (DEM) software. DEM simulation results for thrust forces in the 30-120 RPM regime had a 5-20% inflation of forces compared to experiments. These simulations were then compared with Resistive Force Theory (RFT) plate approximation of the screw geometries. A superposition-based partition approach to the full length screws as well as force generation in shortened, one and two blade screws is analyzed. The force generation is dependent on the flow patterns and cannot be reduced to partitioned approximations as with simple intruders.

3.2 Methods

3.2.1 Experiments

Experiments were conducted in a 20 cm by 100 cm bed of glass beads with approximately 15 cm of depth. Three screws with dimensions of 10 cm axial length and 5 cm diameter were designed in Solidworks and printed using Acrylonitrile Butadiene Styrene (ABS) on a Stratasys 3D printing system as seen in figure 7. Pitch lengths of 4 cm, 6 cm, and 8 cm were used. These screws will be referred to as P4, P6, and P8, respectively. These pitches were chosen based on preliminary experiments where pitches of 2, 4, 6, 8, and 10 cm were examined. As shown in figure 7, the ABS plastic screw was connected to a metal shaft collar coupling. This was then connected to a 12 V Pololu motor. The motor was housed inside a motor casing created with the same printer as the screw. The back cover of the motor casing was then attached to a 6 DOF load sensor using a laser-cut acrylic attachment with six screws. The other side of the sensor was secured to another laser-cut acrylic piece attached to a vertical aluminum rod and locked into place.

8 mN/minute drift is seen in a typical trial. This is after a minimum 45-minute period of allowing the sensor to "warm up" to avoid larger drift which occurs when the sensor has not been used in the previous 24 hours. The brand and model of the load cell are interface force measurement solutions, 6A27A-F11. Horizontal leveling of the motor box was measured via an electronic angle measurement to ensure true horizontal alignment. The sensor was turned on and allowed to warm up for approximately 45 minutes to attenuate thermal drift in the sensor. It was zeroed when steady, then recording began before the test area was filled with beads. The 2 mm glass beads were

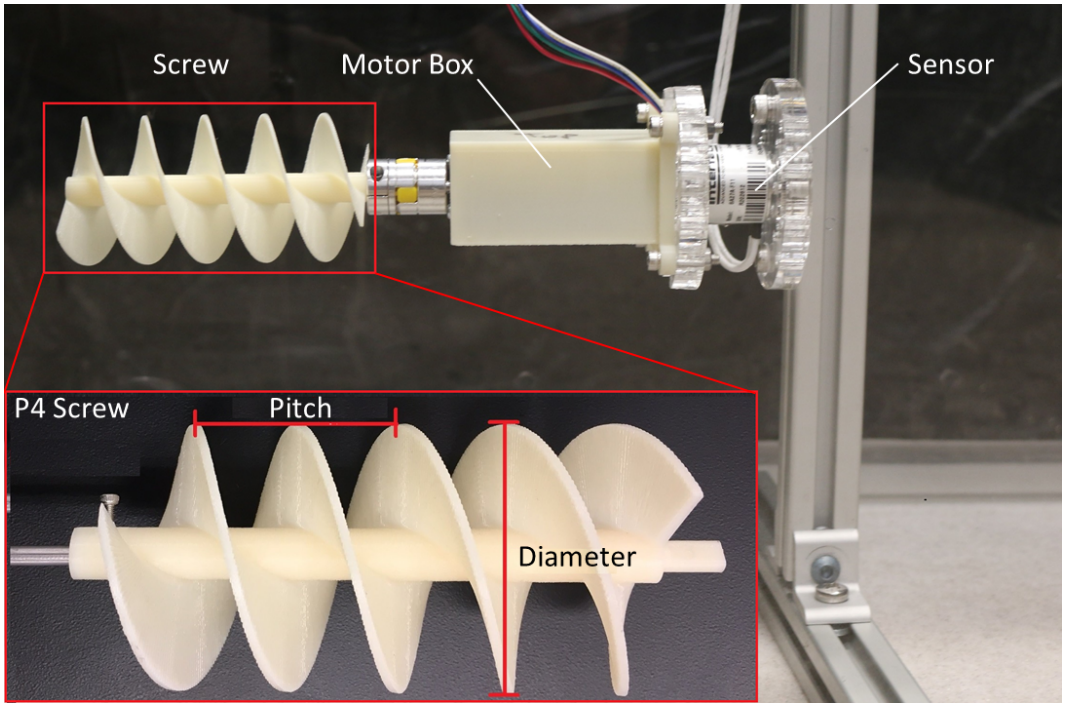

Figure 7. Static screw teststand experimental setup

added such that the screw was completely immersed. The surface level of beads were smoothed for each trial and churned beforehand to avoid compaction or influences of previous trials. Six speeds were used: 30, 45, 60, 75, 90, and 105 RPM. Each trial ran for approximately 15-20 seconds to ensure steady state values. After ten trials, the setup was unloaded by removal of all bead contacts with the motorbox, screw, and other items. Measurements were then taken for ten seconds. Any differences between the unloaded values before and after the experiment were noted and used to address zeroing the average of each set. Typically within each set, some level of thermal drift occurred in the sensor. Therefore the average of the zeroing before and after experiments was subtracted from the average of all trials. The motor control and RPM data collection was driven by an Arduino Uno.

3.2.2 Simulations

Using the model developed in Solidworks, simulations in EDEM, a DEM program (figure 8) were designed. The imported model was then placed inside a simulated cylindrical bed. The simulated environment was filled with particles composed of two overlapping spheres which were slightly offset from each other. This was done to introduce an aspect ratio of 1.1 to eliminate perfect sphericity to correlate with the manufacturer's given 90% roundness. This has been shown [105] to have a significant effect in DEM simulations.

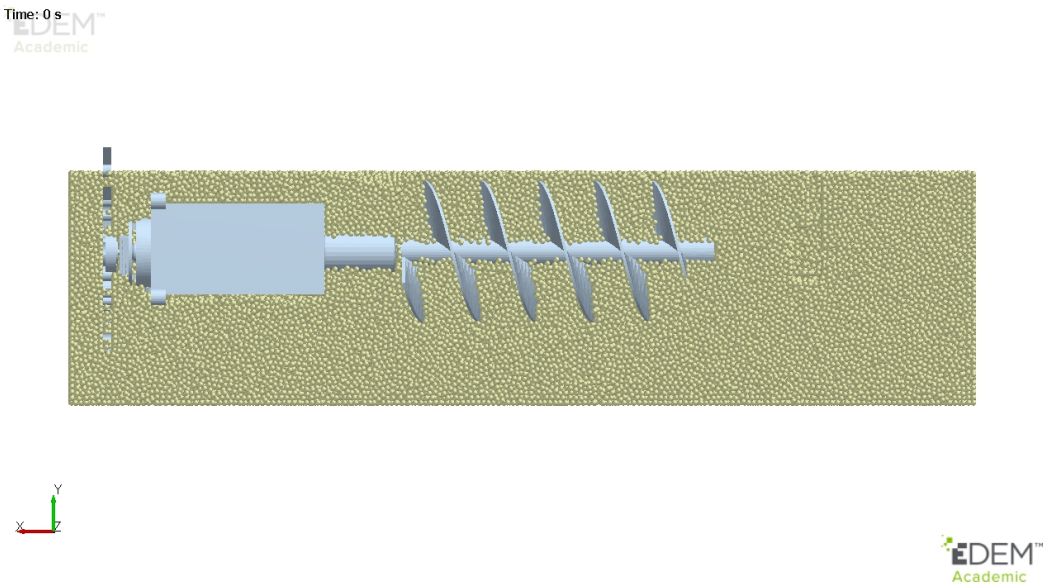

Figure 8. EDEM model with P4 screw (side view)

The degree of eccentricity does not seem to be as influential as its presence. For example, the difference in flow patterns between a perfect sphere and a 1.1 aspect ratio particle is much larger than between a 1.1 and 1.2 aspect ratio particle. The particles were also polydispersed in a normal distribution with standard deviation of

0.1 mm per the manufacturer's specifications. Particles settled until no movement was observed. The beginning of both simulations and experiments occurred with the screw completely covered by granular media. The amount of screw covered is not different across trials in either experiment or simulation, or to each other. The horizontal screw is usually tangential to the surface of beads. Its blades usually are touching the last layer of beads. At this point, the kinematic motion of the screw at the specified rotational velocity began instantaneously. It ran until steady state was observed for two seconds; this required at least seven seconds of simulation. Steady state was defined as a deviation of less than 1% with the previous 1-second average. Details of the DEM contact model are explained in the discussion section. EDEM allows user control over almost all aspects of both the simulated granular material and geometry materials. In addition to shape, there are six mechanical properties to highlight which influence the simulated flow patterns. Three of these are material properties: the density, Young's modulus, and Poisson's ratio. These parameters are well-established for soda-lime glass [137]. The manufacturing method of ABS affects the mechanical properties of the plastic, but recent tests have established baselines for 3D-printed ABS parts [138]. There are three remaining properties which are interaction-dependent: coefficient of restitution, static friction, and rolling friction. These are different between glass-glass interactions and glass-ABS interactions. Several experiments have looked at glass-glass interactions with beads of comparable size. Coefficient of restitution with isolated bead collisions taken from high-speed camera tests in the literature [139, 140], estimate the value at 0.97 for collision speeds under 1 m/s. The same study estimates the dynamic coefficient of friction as 0.092 and static coefficient of friction between 0.16-0.29. Simple glass-glass static friction tests

were performed and found values similar to the lower end at 0.16. The rolling friction coefficient of glass beads against each other is estimated at 2.5E-5 to 5E-5 [141].

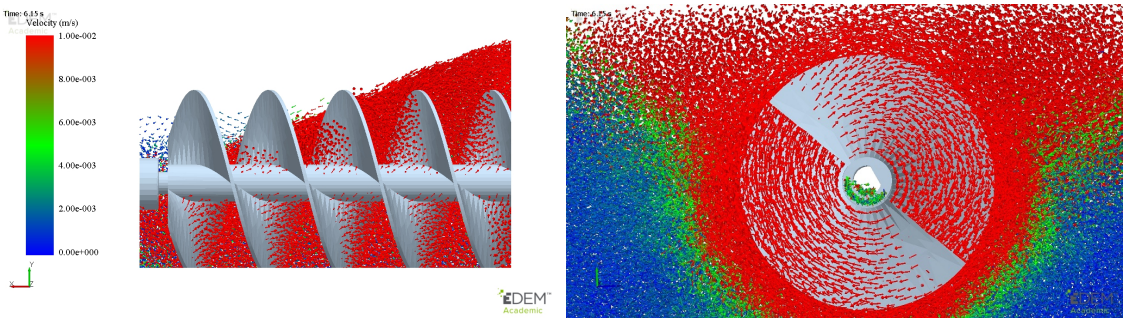

Figure 9. Flow visualization of particles in side and front view

We did not find Glass-ABS interaction properties reported in the literature. The coefficient of restitution of several different 3D-printed materials has been tested. Researchers used an aluminum rod at various speeds on plastic plates composed of these materials [112]. Coefficient of restitution will also change based on the order of magnitude of velocity. The impact speeds for this study are comparably low (below 0.5 m/s) and hence the value of 0.7 was selected as the best approximation. Similarly, the information on glass-ABS friction interaction in the literature is rare. For static friction, a tilt test was conducted between two plates. Static friction for glass-ABS was estimated at 0.16, similar to the glass-glass interaction. A standardized ASTM rolling friction test was adapted [142] for the coefficient of rolling friction. This resulted in a rolling friction of 0.173.

The simulated bed is 32 cm long and 20 cm in diameter. Force/velocity imaging for simulated particles was observed, an example of which is shown in figure 10. No wall effects were observed, and particle forces were below 0.0002 N at walls as shown. The

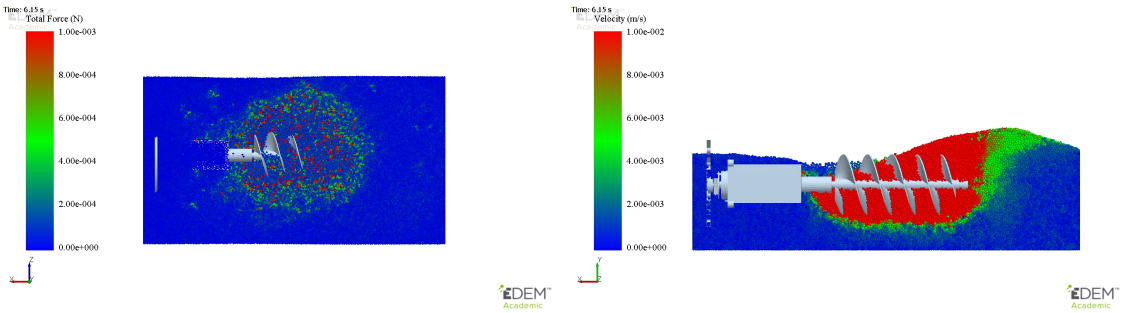

Figure 10. Buildup of particles from top and side view and colored by force and velocity respectively

piles formed at the end of the bed had the same shape/height/extent in experiments and DEM. This was an item of concern before beginning simulations and monitored.

3.3 Results and Discussion

3.3.1 Experiments

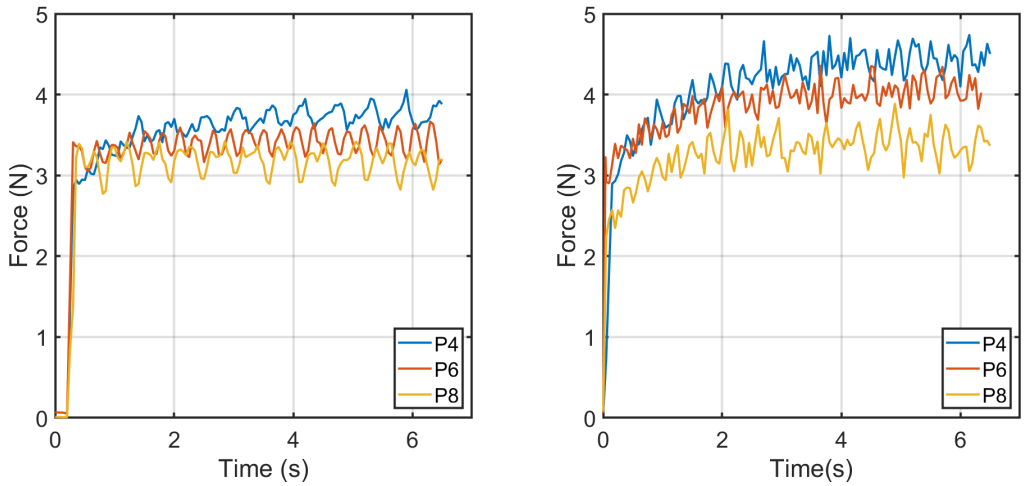

Figure 11. Thrust force versus time at 105 RPM for (a) experiments vs. (b) simulations.

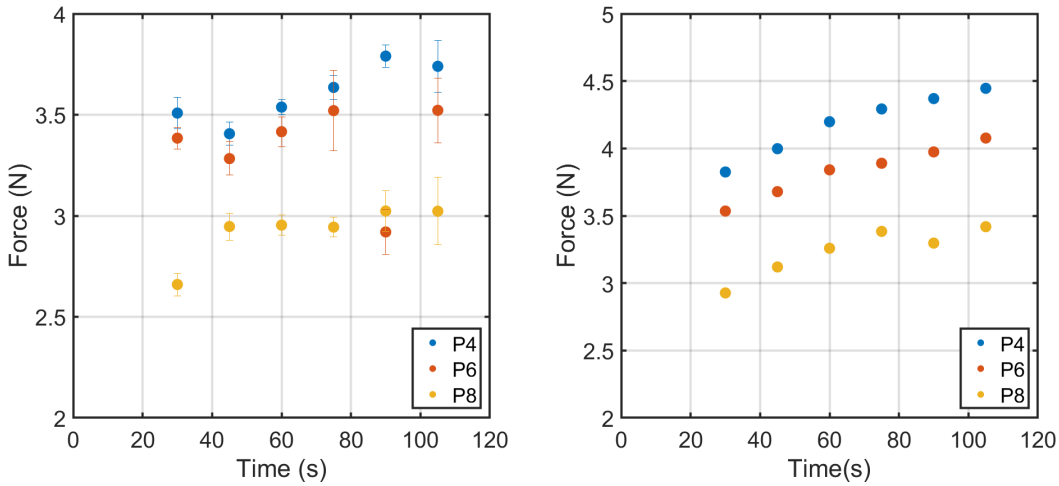

Figure 12. Thrust force. (a) Experiments vs. (b) simulations.

The experimental force data is taken from the steady state plateau of each individual trial for multiple seconds and averaged, per trial. All trials are then averaged with standard error shown in the plots. A force graph of what an experimental trial run looks like can be seen in figure 11a and a simulation is seen in 11b. The simulation takes slightly longer to reach steady state, but the force evolves in a similar manner. Since each combination of design and speed was only simulated once, there is no standard deviation to speak of for DEM simulations. Given values are the mean force over the last 2 seconds of data, and the noise oscillations are typically within a 0.5 N band. All experimental results for thrust force as a function of RPM are shown in figure 12a. As the pitch is shortened and an increased amount of surface area faces the axial direction, thrust force increases. The force also increases with RPM, but inertial forces are not the primary contributor to the magnitude of thrust force in this case. For experiments, the thrust force increase from lowest to highest RPM for P4, P6, and P8 was of 11.9%, 4%, and 13.6%, respectively.These results are within the range of other observations for increased force in granular media due to inertial forces.

For example, less than 20% increase in forces on intruders was observed when velocity was increased from 1 cm/s to 1 m/s [127].

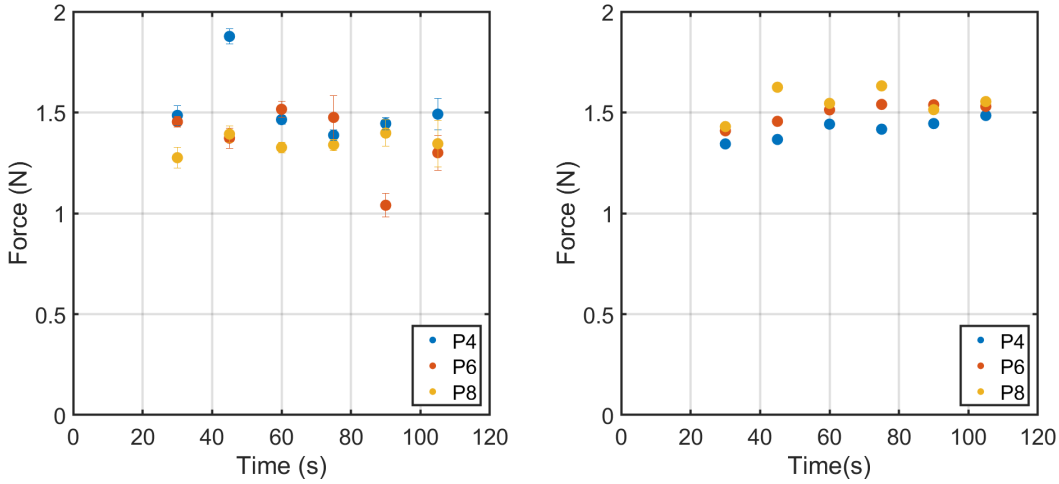

Figure 13. Vertical force. (a) Experiments vs. (b) simulations.

In contrast to the horizontal thrust force data in figure 12a, the vertical force data in figure 13a shows virtually no relationship between vertical force and RPM, nor vertical force and screw pitch. The vertical force changes from 30 RPM to 105 RPM in experiments were -1%, -10%, and 5% for P4, P6, and P8, respectively. Looking at figure 13b shows a different story for simulations as P4, P6, and P8 vertical forces increase by 10.3%, 8.5%, and 8.6% from lowest to highest speed, respectively. During these experiments, as previously mentioned, the trial begins with the leveled surface tangential to the screw blade as shown in figure 8. It ends with a steady state mound at the expelling end, shown in figure 10, continually regenerated from beads falling after the angle of repose is exceeded. Note that these results, indicating small vertical force compared to the axial force, are limited to surface conditions. They cannot be extrapolated to the force relationship a deeply buried screw may experience.

3.3.2 DEM Simulations

Thrust data for simulations are shown in figure 12b. A plateau appears at the end of the curve. Because of the screw's surface level, the majority of force being generated is coming from the accumulated pile of material near the discharging side. While the RPM cannot change the angle of repose, a faster speed can continue to recirculate and deposit material at a higher rate, resulting in more thrust force. Hence, at higher speeds a mild increase in force is observed. It appears that thrust forces begin to plateau at high speeds. The avalanching slope of the mound does not reach the boundary of simulation or experiment according to observations. Figure 10 shows that boundary particles are not significantly affected. During both experiment and simulation, no wall effects were present.

The plateau can be explained if the affected area around the screw is viewed as a control volume. As the screw speeds up, the mass flow rate of particles out of this control volume begins to increase. However, the maximum mass flow rate of particles into the control volume, or "refill rate", is a function of both gravity (the acceleration forces pushing the particles downward to open space) and particles angle of repose and thus, it does not change. At a high enough speed, the mass flow rate of particles out of the control volume begins to equal or exceed the maximum mass flow rate into the control volume. This is analogous to a choked flow in fluid dynamics.

As shown in figure 12b, the band between higher and lower speeds stays consistent. For P4, P6, and P8 the amount of force increase from 30 RPM to 105 RPM is 15.5% 15.3%, and 16.7%, respectively. Similar to experiments, the simulation forces in figure 13b do not show much magnitude difference in the vertical direction. In particular,

P4, P6, and P8 vertical force increases are 10.3%, 8.5%, and 8.6% from highest to lowest speed respectively.

As shown in figure 12, the average thrust force increase from experiment to simulation across all RPM's is 16.0%, 15.2%, and 10.6% for P4, P6, and P8. The average vertical force difference between experiment and simulation across all RPM's is -5.4%, 12.1%, and 15.2% for P4, P6, and P8. Some of the sources contributing to these differences in magnitude will be discussed in the error section.

3.3.3 Resistive Force Theory

One recent approach to assess granular mobility and force generation is RFT. Under the assumptions of negligible inertial forces and using superposition of geometric components, RFT examines the forces on geometries in granular media. It does so by characterizing the shape into discrete plate elements. These plate elements, based on orientation, are compared to previously acquired data in various granular media. As long as these elements are independent and do not influence each other, they can be added together [122]. The forces are derived from empirical equations found through evaluation of a flat plate at different orientations and velocities. By applying a Fourier transform to the data of multiple granular media, empirical equations were obtained which linked the forces generated as a function of orientation angle and velocity vector.

We applied an RFT approach to the horizontal, helical screw under the assumption that it could be well approximated with small plates. Estimations of the total screw force correlated poorly between experiments and RFT (see supplemental material A). The RFT estimated forces were 10.34 N for a 2 cm (half-pitch) P4 screw buried at 4 cm and 19.90 for a 10 cm P4 screw with upper blades located just at surface level

of the granular media, compared to 4.51 N for P4 DEM simulations. This prompted a closer investigation into the mechanics of how a screw generates force in granular media.A DEM simulation where the depth of the screw was increased to 4 cm instead of just below the surface level was run. This ensured that the depth would stay consistent rather than the material piling to one side as with the surface case.

As shown in figure 14 the last 2 cm (a half pitch-length or "turn") of the 10 cm length screw generated 55.8% of the total force. The last 4 cm, a full turn, generated 63.1% of the total force. RFT would predict uniform force generation across the screw if none of the geometry was interfering with other sections. Therefore, the initial conclusion for RFT failing to reproduce the forces was that the current designs were violating superposition by introducing leading edges. A leading edge is a portion of the object's geometry which is in front of another portion of the object in the direction of travel. By doing this, the first portion affects the flow pattern applied to the second portion. This violates a key aspect of superposition, namely that the additive portions do not affect each other. Each chamber was moving material forward along a path which the proceeding chamber had already cleared. The section of the screw pushing granules against a bulk of granules and generating the majority of the force is the expelling end.

The above insights prompted an investigation to see if perhaps a screw which did not violate the leading edge assumption would correlate better to a plate approximation. Similar simulations were run but with screws of half-pitch length instead of the full 10 cm so that the leading geometry assumption would not be violated. 2 cm P4 screw was used as the sample. The screw was placed at a 4 cm depth and run at 15 and 30 RPM with negligible difference. This is within the range of depth tested during the experiments used to create the empirical RFT approximation equations. The results

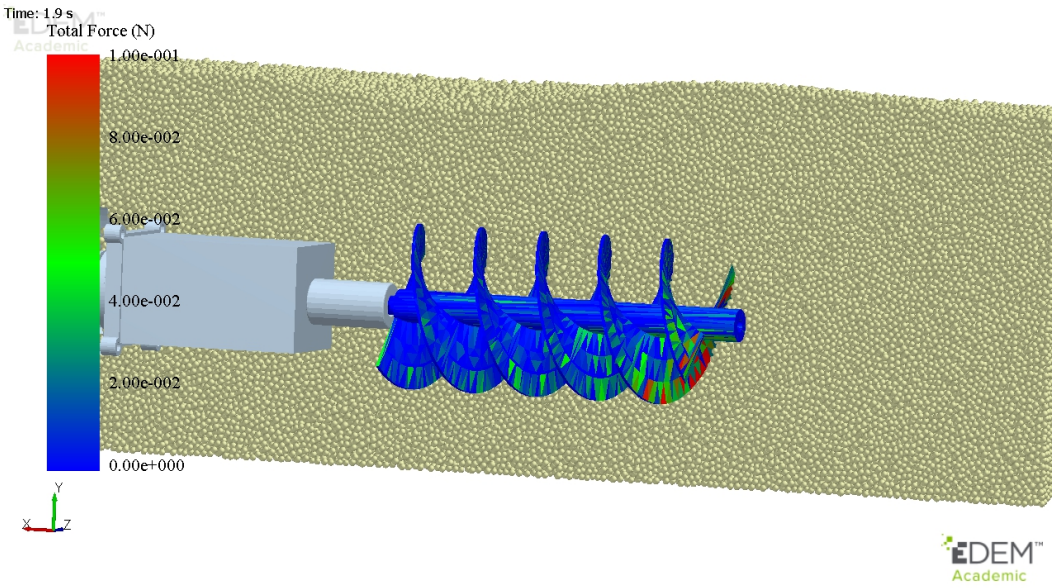

Figure 14. These instantaneous forces occurring at the given time across the discretized screw in the simulation are unevenly distributed, showing much stronger forces generated at the expelling end (right side of the screw)

of this indicated a force generation of approximately half of that predicted by RFT estimations. This prompted another investigation into whether force generation per screw blade would be additive. The number of blades in the screw is designated by "N" followed by a number. An N1 screw, a screw with only one helix winding, was evaluated in the same depth as the N2 screw. For the buried P4 N2, 5.5 N axial force resulted. For the buried P4 N1 in identical conditions, an oscillating force of 2-5 N depending on blade orientation was observed. To construct the hypothetical force of a screw with two of these blades, the results were offset by a half-cycle and summed.

The N1, N2, and theoretically constructed N1+N1 are seen in figure 15. The results indicate that added blades do not scale linearly even under ideal conditions. This perhaps seems intuitive in hindsight, especially compared to bladed geometries interacting with fluids, but it was unclear if slow movement in granular media would

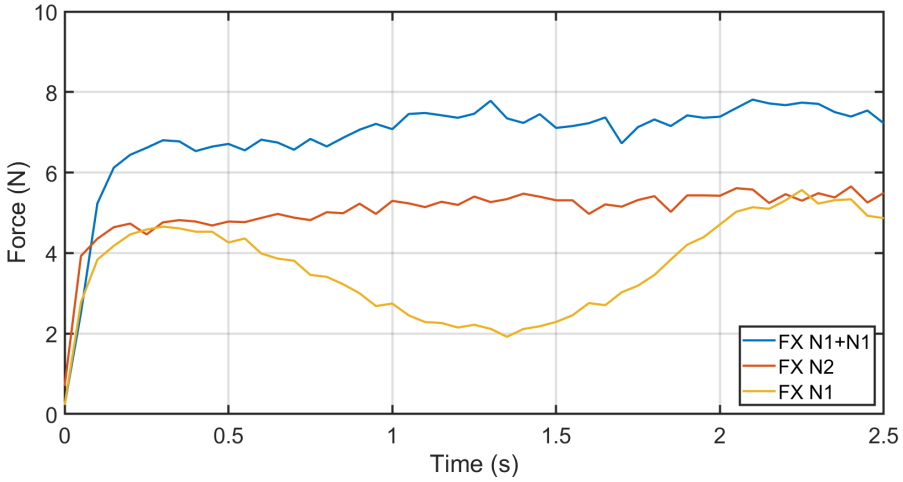

Figure 15. The force of a double-bladed screw is significantly smaller than the sum of two single bladed screws

hold to the same rule. This indicates that RFT which relies on superposition should be approached with caution when applying to screw generated forces in granular media.

Indeed, the flow pattern of the screw is of utmost importance to the force generation if results from a full 10 cm screw and a half-pitch screw are compared. The last 2 cm of the 10 cm P4 screw generated 4.5 N of force. In comparison, the 2 cm screw with an identical section by itself generates 5.5 N of force. This shows the importance of the previous screw sections in affecting the flow pattern and hence the amount of force a screw will generate.

3.3.4 Potential Sources of Error

As discussed before, DEM uses a different approach than analytical methods such as continuum mechanics or empirical methods such as resistive force theory [133, 143]. Each individual particle is modeled as to affect the other particles. There are different physics models which can be selected for DEM simulations based on the attributes of

the granular media. Some models incorporate cohesion, adhesion, machine wear, and other aspects. The Hertz-Mindlin model was selected based on the need for a robust model without requiring wear, thermodynamics, or other analysis. The model is built on Hertzian contact theory while integrating tangential forces, damping forces, and friction forces. In this model, normal contact forces, F_n are functions of the specific Young's modulus, E^*, the specific radius of particles, R^*, and the overlap, δ_n. The i and j subscripts denote two subsets of qualities for the two particles colliding. Since the physics model is driven by spherical contact, it looks at many calculations for the two individual spheres where each one has its young's modulus, radii, etc. The E* and R* are then called the "specific" quality of the calculation. The specific Young's modulus is a function of the Young's modulus and the Poisson's ratio, ν_i, of the two particles colliding. During particle collision, the simulation creates a small overlap representing an estimated real world deformation. The higher the Young's modulus, the smaller the allowable deformation. The smallest allowable deformation determines the timestep of the simulation due to more frequent checks. A higher Young's modulus would allow less deformation, which requires the program to check the simulations with a much higher frequency.

$$F_n = \frac{3}{4} E^* \sqrt{R^*} \delta_n^{\frac{3}{2}} \tag{1}$$

$$\frac{1}{R^*} = \frac{1}{R_i} + \frac{1}{R_j} \tag{2}$$

$$\frac{1}{E^*} = \frac{1 - v_i^2}{E_i} + \frac{1 - v_j^2}{E_j} \tag{3}$$

A DEM time step is therefore a function of particle stiffness. Real modulus values make EDEM simulations computationally costly. This leads to a decision to reduce the Young's modulus by several orders of magnitude [141, 144, 145, 146, 147]. For

clarity, a reduction of magnitude by 100 results in 10 times faster simulation times in this case [148].

Bulk behavior such as angle of repose does not change significantly until Young's modulus has been lowered beyond the 10 MPa range [148]. Materials close to this range of stiffness (or lack thereof) will begin to see their piles collapse under their own weight for most materials. However, flow behavior may change if significant overlap is allowed with geometry. Thus, the Young's modulus is modified to examine the difference in simulation results with the chosen value for stiffness (20 MPa) versus a value closer to the measured stiffness of glass (680 MPa, 1% of the real world value). A modest decrease in overall thrust force of 4.31 N to 3.9 N when adjusting particle stiffness from 20 MPa to 680 MPa was observed. This is due to the increase in overlap between flowing particles and thus, packing more particles into the same volume that the screw is pushing against.

The reduced particle stiffness introduces some uncertainty into the simulations. The key aspect forthe study is that the particles are pressed against themselves as well as against a complex geometry. When Young's modulus reduction was analyzed [148] the possibility of force changes was discussed. The takeaway is that Young's modulus reduction can cause different forces for simulations than their real-world counterparts when particle compression against geometries or particles is a significant feature of the flow. However, this difference was shown to be predictable and consistent in this particular case. In addition, experimental errors may also contribute to the modest discrepancies between experiments and simulations. In particular, load cell drift, minor screw misalignment, variability in mechanical properties, and 3D printing imperfections may play a part in slight differences observed between experimental results and DEM simulations.

Chapter 4

HELICALLY-DRIVEN GRANULAR MOBILITY AND GRAVITY-VARIANT SCALING RELATIONS

4.1 Abstract

This study discusses the role and function of helical design as it relates to slippage during translation of a vehicle in glass bead media. We show discrete element method (DEM) and multi-body dynamics (MBD) simulations and experiments of a double-helix Archimedes screw propelled vehicle traveling in a bed of soda-lime glass beads. Utilizing granular parameters from the literature and a reduced Young's modulus, we validate the set of granular parameters against experiments. The results suggest that MBD-DEM provides reliable dynamic velocity estimates. We provide the glass, ABS, and glass-ABS simulation parameters used to obtain these results. We also examine recently developed granular scaling laws for wheels applied to these shear-driven vehicles under three different simulated gravities. The results indicate that the system obeys gravity granular scaling laws for constant slip conditions but is limited in each gravity regime when slip begins to increase.

4.2 Methods

4.2.1 Laboratory Experiments

Three screws with dimensions of 10 cm axial length by 5 cm diameter were created in Solidworks and printed using Acrylonitrile Butadiene Styrene (ABS) on a Stratasys 3D printing system. Pitch lengths of 4 cm, 6 cm, and 8 cm were used. This translates to helix angles of 75.7°, 69.1°, and 63° respectively. The versions of the craft using these pitch lengths will be referred to as "P4", "P6", and "P8". The body of the craft was similarly printed and contains an Arduino Uno and Sabertooth motor shield to drive two Polulu 12 volt motors contained inside printed pontoon covers. This assembled craft in figure 16 was then tethered to a testing computer and power supply. The craft setup was chosen to ensure consistent power and prevent any inconsistent battery effects during long test sessions.

This craft was then set in a 20 cm by 100 cm bed of 2 mm glass beads using approximately 15 cm of depth. Speed of the motors was directly monitored via encoders during each trial to ensure consistency during testing. Seven speeds were used: 30, 45, 60, 75, 90, 105, and 120 rotations per minute (RPM). P4 spanned 45-120 RPM, P6 spanned 30-120 RPM, and P8 spanned 30-120 RPM. The P4 set of screws had difficulty overcoming initial resistance at 30 rpm and these results were discarded. Each trial ran for approximately 10-15 seconds. The craft was placed on the top of the beads and allowed to rest under its own weight. The glass beads bore the weight of the craft and it did not sink while stationary. It was levelled by observation at the beginning of the run. At the end of the run, the craft would be tilted backwards slightly. This procedure was repeated for the DEM simulations, with the craft initially

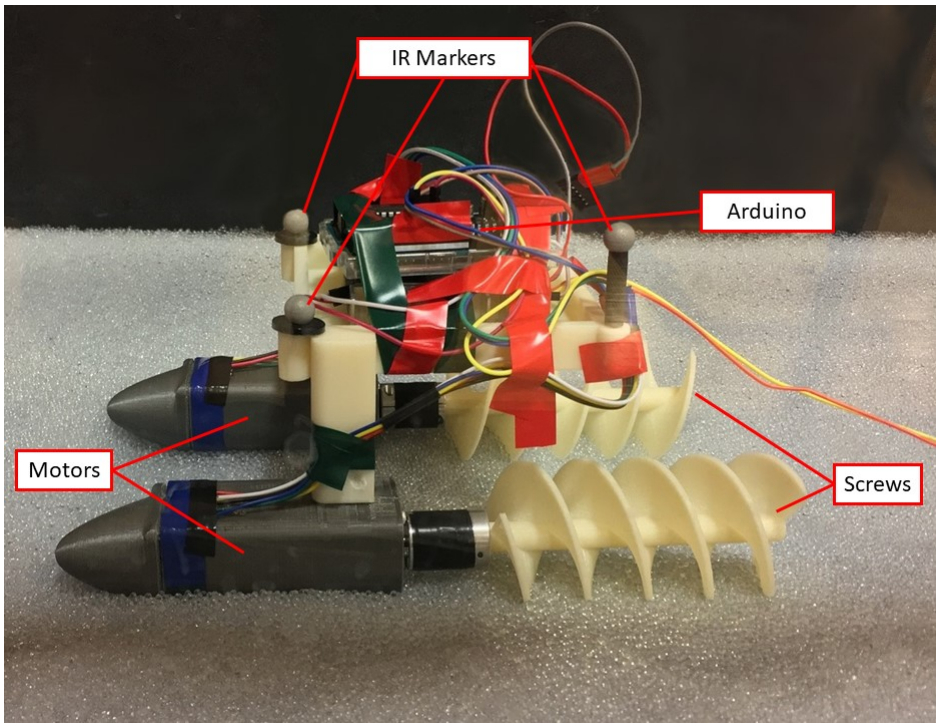

Figure 16. Experimental test craft resting in glass beads with internals exposed

placed a negligible but non-zero distance above the bed of beads. After ten trials, the Arduino was reprogrammed for the next speed and run again. The motor control and RPM data collection were driven by the Arduino. The craft position was monitored via an Optitrack infrared camera system.Three infrared silver markers were attached to the craft as seen in figure 16 and the cameras (not seen here) were mounted to the four corners of the test bed. The Optitrack infrared camera system produced position data of the markers in its calibrated reference frame versus time. Velocity was calculated using distance traveled over time. Initial analysis examined both depth and lateral travel distances and found them negligible. A surface leveling instrument was used after every trial and beads were reset manually to ensure adequate mixing.

4.2.2 MBD-DEM Simulations

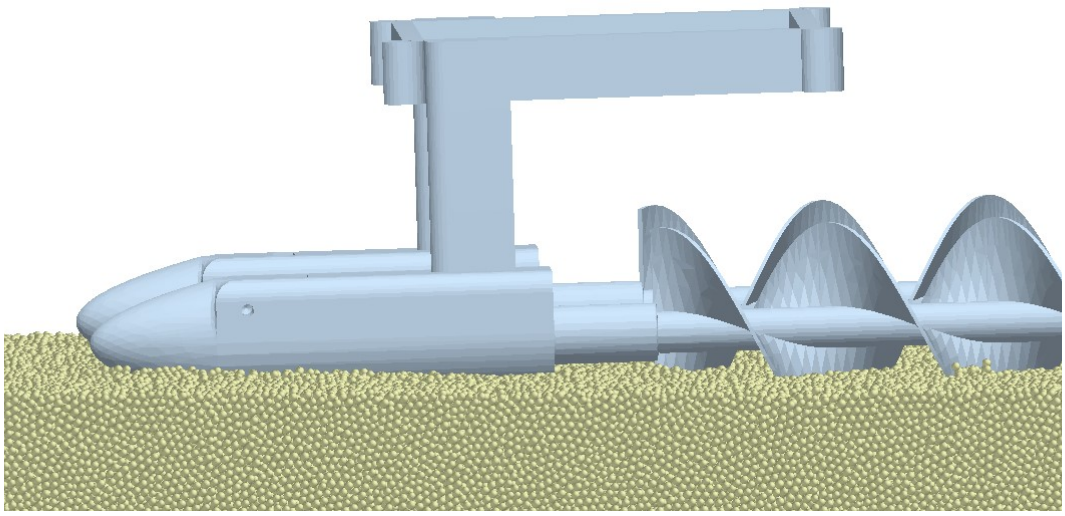

Figure 17. Simulation setup in DEM program showing craft and beads

The same designs used to manufacture the ABS parts were utilized in the simulations. In DEM, simulation completion time scales exponentially with number of particles. This was something we wished to avoid. Thus, simulation time was reduced by decreasing the dimensions of the simulated bed. The experimental environment was a multi-purpose test bed and therefore arbitrarily large compared to our requirements for avoiding wall effects. During preliminary simulations, we evaluated several simulations which were identical except for incremental narrowing of the bed. We examined the results and chose the smallest size which showed no wall effects. We also

used the simulation data to assess the necessary length of the test bed for achieving the steady velocity. The granular environment was set up in a DEM program called EDEM as seen in figure 17.

DEM simulations allow user control over many aspects of the simulated granular materials and intruder geometry materials. These parameters were set to the best matches found from the literature. Key glass and ABS values are listed in Table 1. Key interaction values are listed in Table 2. A thorough explanation of these values is contained in the results of a static force generation experiment [149] but we will discuss these briefly.

Table 2. Properties of simulated glass, ABS, and interactions

Material Property	**Glass**	**ABS**
Poisson's Ratio	0.24	0.35
Density (kg/m^3)	2500	1070
Young's Modulus (Pa)	7E7	1.8E9
Interactive Property	**Glass-Glass**	**Glass-ABS**
Coefficient of Restitution	0.97	0.7
Coefficient of Static Friction	0.16	0.174
Coefficient of Rolling Friction	2.5E-5	0.162
Other Properties	**Value**	
Aspect Ratio of Spheres	1.1	
Average Particle Size	2mm	
Particle Size Standard Deviation	0.1mm	
Simulation Timestep	4.84E-6 s	

As discussed before, DEM uses a different approach than analytical methods such as continuum mechanics or empirical approaches. Each individual particle is simulated. The effect of particles on each other is driven by the selection of physics models based on the needs of the user and the attributes of the granular media. Some models incorporate cohesion, adhesion, machine wear, and other aspects. The Hertz-Mindlin physics model was selected based on the need for a robust model without requiring wear, thermodynamics, or additional analysis. The model is built on Hertzian contact

theory; since the model is driven by spherical contact, it looks at calculations between two spheres and drives the motion based on Young's modulus, radii, etc. During particle collision, a small overlap representing an estimated real-world deformation is allowed. This allowed deformation is based on the stiffness from the Young's modulus. A smaller allowable deformation requires more frequent checks and hence, a smaller time step and higher frequency. This slows the progress of the simulation and a balance must be struck between implementation and material fidelity. Particles in the simulation were modeled as closely to the glass beads as possible. The aspect ratio of 1.1 means that a small degree of eccentricity was introduced by creating particles in the program which were two slightly offset spheres overlapping each other. The software uses spherical contact physics models and as such, all particles generated are some composition of spherical surfaces. The dynamics of the craft and reaction physics were driven by a multi-body dynamics (MBD) software called Adams [150, 151]. In the case of MBD-DEM co-simulations, the MBD software will control the movements of the craft. For example, in our case we set the rotational speed of the screws in Adams. The model and physics behind it were then exported to the simulated granular environment. In our case we set the rotational speed of the screws in Adams. Adams simulates the relationship between the solid bodies of the craft dynamic system and their reaction to the environment; it simulates how the craft linkages react to internal linkage forces and external environmental forces. The DEM program, EDEM, simulates how the granular media reacts to the internal granular forces and external geometry forces [152, 153, 154]. The center of mass in EDEM is co-located at the identical space in the universal coordinate frame as the center of mass in Adams. EDEM calculates how the granular media reacts to the geometric intruder's motion. It then sends reaction forces to the MBD program after a discrete

time step. These reaction forces are implemented by Adams onto the craft geometry and translated into movement during each discrete time step. The craft location is adjusted in EDEM, reacts with the granular environment, and this cycle continues until completion of the simulation. Simulations of Earth-gravity experiments were run to compare directly to their experimental counterparts and identify any salient patterns or differences between the two. All simulations were run using the discrete time step listed in table 1. All simulations ran for a total length of 2.5-3 seconds. This length of time was determined to be the minimal amount of time required to reach steady state velocity.

4.3 Results and Discussion

4.3.1 MBD-DEM Earth Simulations Compared to Experiments

All results for craft steady state velocity as a function of RPM are shown in figure 18. Velocity as a function of RPM had slopes of 0.386, 0.656, and 0.855 for P4, P6, and P8 respectively. This relationship has an observably linear trend. At least four RPM data points for each simulation were also used to establish trends. The craft velocity of each set of simulations was higher than that of the experiments, as observed in the individual pairings. When the slopes of experiment and simulation best fit lines are compared, the increases are 25.3%, 18.5%, and 15.2% for P4, P6, and P8 respectively. In terms of raw inflation between experimental values and simulated for each RPM, the average was 18.3%, 4.5%, and 17.5% respectively. The maximum difference between experiment and simulation data was P4 at 120 RPM. Steady state for experimental was 47.7 mm/s while simulation was 59 mm/s for a difference of

23.1%. While the simulated values showed inflation, and changed slightly between designs, the overall trends for all simulations and their experimental counterpart were very similar. The R^2 values, coefficient of determination, of these fit lines ranges from 0.9967 to 0.9998.

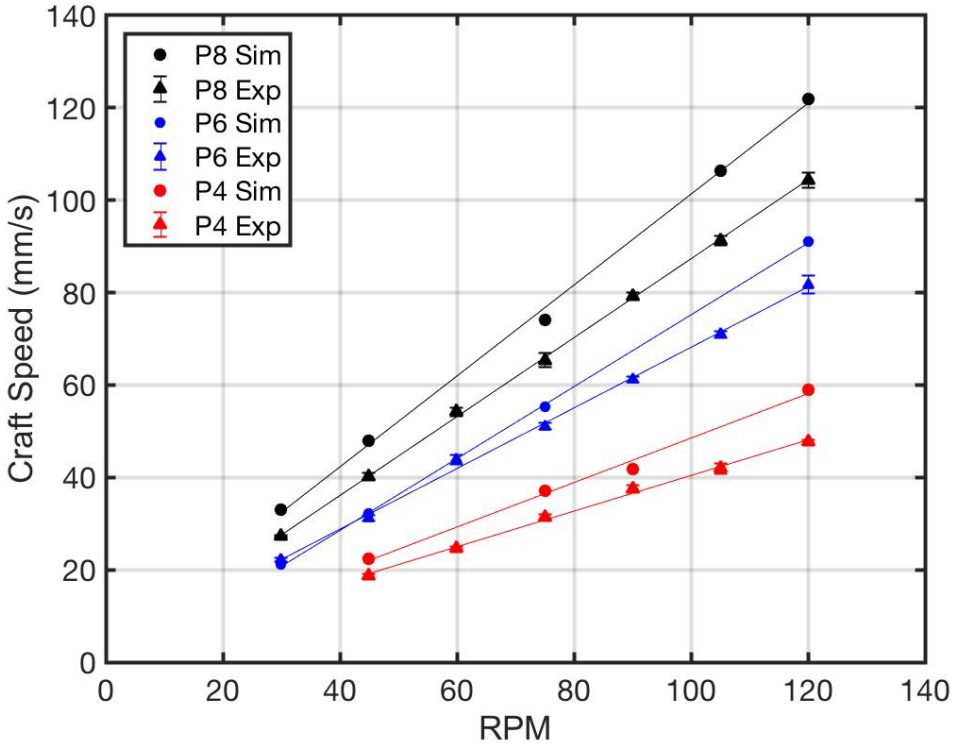

Figure 18. Experiments and simulations compared for three craft designs

4.3.2 MBD-DEM Earth Simulation Slip Trends Compared to Experiments

This same data, when converted to no-slip format, also shows uniform trends compared to the experiment as seen in figures 19. Imagine a cylinder with helical windings. As this screw rotates in place on its center axis, the real path in space of any

arbitrary point on it is a perfect circle around that axis of rotation. Yet when observed rotating, that arbitrary point can appear to move in a forward or backward motion perpendicular to this plane because during rotation, a new portion of the helix has shifted to occupy that control volume. As the pitch of the screw is increased, the rate at which physical blade geometry enters or exits that control volume increases as well. When contact is made with a group of particles, those particles resist the movement of the helical blades within their particular control volume. This reaction force propels the craft forward. We define no-slip velocity as the hypothetical translational velocity achieved if rotational motion is converted to translational without loss.

For example, if a tire rotates without slipping along the ground, it will translate the distance of one circumference per rotation. For a screw, no slipping would mean a translation of one pitch per rotation. A screw with a 4 cm pitch rotating at 60 RPM (1 rotation per second) would have a no-slip velocity of 4 cm/s. The pitch couples the rotational and translational movement. Slip, in the context of this chapter, is the ratio of the actual craft velocity to the maximum velocity possible if all locomotive efforts were perfectly transferred into translational motion. Let us now take the black triangles of figure 4 as an example. The furthest datapoint shows coordinates of approximately (160,120). This indicates 25% slip because the actual velocity is 75% of the theoretical maximum. If we move several datapoints down the black triangles, we can see a datapoint which looks to be approximately (100, 75). This, again, indicates 25% slip. The ratios of actual velocity to theoretical remain very close and are expressed in that slope. However, the real difference between the theoretical maximum and actual velocity of the two datapoints change. In the slower datapoint, the gap is 25 RPM and in the faster datapoint the gap is 40 RPM.

If the no-slip velocities of all three screws are plotted with their experimental results on one plot as seen in figure 19, we can see that the levels of slip experienced between the three designs is quite similar. The overall slope of the experimental data is 0.657 for actual velocity vs no-slip velocity. All experimentally tested points obey this linear fit, indicating that our experiments were below velocities which would significantly increase slip levels. As the velocity gets higher the linear fit will no longer apply due to the refill rate of the granular media in Earth's gravity. At reduced gravities, this peak velocity and slip begin to change as demonstrated in the reduced gravity section of this article. All tested points demonstrated an observable linear relationship between translational velocity and the no-slip velocity with little variation between the trials for each data point; the largest standard error experienced was 1.9 mm/s. This data was therefore deemed an acceptable target to validate DEM simulations against.

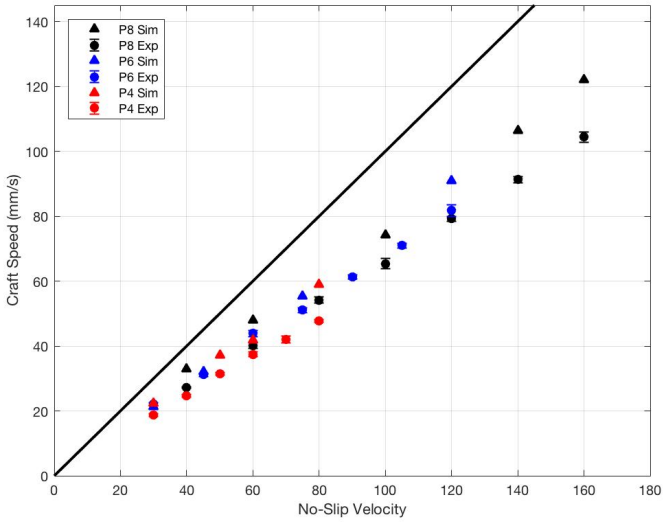

Figure 19. Slip trends shown for individual designs

The thick black line indicates where no-slip velocity would occur. The slope of such velocity would be 1.000 on this graph.

The slope of actual velocity vs no-slip velocity is 0.761 for all simulation data, an overall increase of 15.8% from the 0.657 for all experimental, as seen in figure 20. The simulation data also follows a constant linear trend for slippage. The individual slopes for P4, P6, and P8 in simulation are 0.725, 0.775, and 0.719. This is an increase of 25.6%, 18.1%, and 12.2% for each design respectively over experimental slopes. This means that the simulated craft experienced both a) closer rates of slip between designs than the experimental cases, and b) less overall slip during movement than experiments. Several DEM simulation material parameters could be the cause of this variation. The Young's modulus has been purposefully reduced. The rolling or static friction coefficient between glass and ABS are possible causes of differences between simulation and experiments. The surface friction of printed materials may vary with different geometries, printers, and print conditions. There also were no studies found in the literature which explicitly tested printed ABS and glass. The coefficient of restitution was also not found to be explicitly tested. This is another potential cause, but we hypothesize a less likely one since impact speeds in these simulations were low. Furthermore, the modification of Young's modulus is another potential cause. We know that it can modify forces by slightly changing the packing fraction (less rigid material can pack more tightly into the same space) and this gives the screw a more densely packed media to push against. It may also affect drag forces. Finally, the differences could also be explained by the approximations required to use the Hertz-Mindlin physics model in DEM or the choice of time steps.

This leads to two insights. First, the data shows that with calibration of simulation parameters to test data, MBD-DEM simulations can reproduce craft movement from

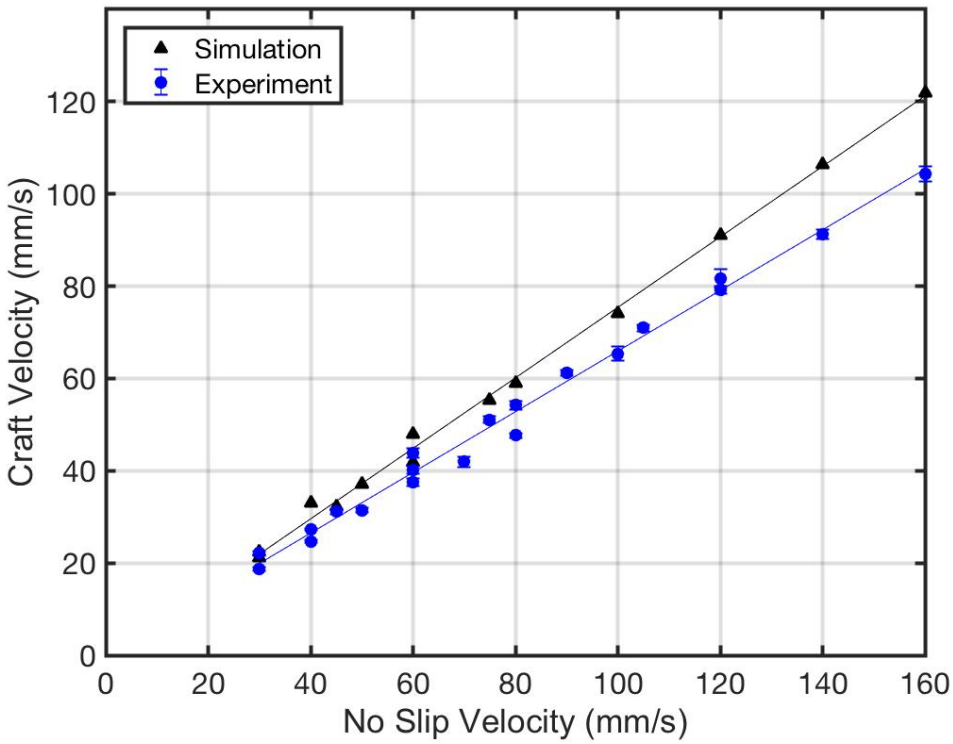

Figure 20. Comparison of simulation slip trends versus experimental for all designs combined. Actual craft velocity achieved is compared to the hypothetical maximum no-slip velocity. Trend lines of simulations and experiments can be compared to the thick black line, which indicates what a constant, no-slip velocity would look like.

shearing, helical geometries in a range of speeds under the assumptions of constant slip. This is while utilizing a Young's modulus reduction technique by several orders of magnitude. The Young's modulus was reduced from a nominal value of 70 GPa to 70 MPa for simulation. Evidence in the literature suggests that bulk behavior may not show significant error until Young's modulus is lowered below the 1E7 threshold [148]. Second, the choices for glass and ABS material properties, as well as interaction parameters, for these DEM simulations have been successfully validated to a reasonable degree. With Earth gravity validated to within a 15% offset of experimental values,

we now move on to a set of computational comparisons which address granular scaling laws with a focus on gravity reduction.

4.3.3 MBD-DEM Lunar and Ceres Gravity Simulations compared to General Scaling Relations for Varied Gravities

Recent granular scaling laws have been developed in the literature which have implications for traversing granular media[134]. These have been tested and confirmed for arbitrarily shaped, rotating intruders of uniform thickness in one dimension. This includes a classic wheel shape, a lugged wheel, and even a rotating rectangular bar. The dimensional analysis performed in the literature relies on mass, wheel shape, dimensions, speed, and gravity. First, assume a wheel of arbitrary shape f and let us define the inputs. This wheel has a tire thickness of D into the page. It has a characteristic length L that scales with the shape, typically defined as a radius for circular wheels. The wheel has mass M concentrated on the axle, acted on by constant g gravity. Assume a consistent granular media and a fixed rotational velocity ω. The outputs of interest derived from this are craft mobility power, P, and the wheel's translational velocity V. These outputs are a function of time, t. The non-dimensionalized relationships between these, derived in the cited literature, are as follows:

$$\frac{P}{Mg\sqrt{Lg}}, \frac{V}{\sqrt{Lg}} = t\sqrt{\frac{g}{L}}, f, \frac{g}{L\omega^2}, \frac{DL^2}{Mg} \tag{4.1}$$

This results in a relationship between the variables:

$$(g', L', M', D', \omega') = (qg, rL, sM, sr^{-2}D, q^{1/2}r^{-1/2}\omega) \tag{4.2}$$

This also results in relationships for output variables as well:

$$P' = q^{3/2} r^{1/2} s P \tag{4.3}$$

$$V' = q^{1/2} r^{1/2} V \tag{4.4}$$

These were experimentally validated in the literature [134]. However, a key feature of the scaling laws is focus on strictly uniform-thickness wheels with the axis of rotation perpendicular to the direction of translational motion. This motion is primarily driven by contact forces with particles near or on the surface of the granular media and to a certain depth based on stress envelopes. In a screw-powered vehicle, the rotating axis is parallel to the direction of translational motion and utilizes an intruder with a different set of reaction forces in the medium. Since screws and augers offer opportunities for mobility, anchoring, and material transfer in both terrestrial and space settings, it is worth examining whether a dynamic scenario can be predicted by these particular laws or not. If shear-dominated motions can be expressed by the same laws, it increases the robustness of these parameters. We removed the differences of size and mass by setting s=1 and r=1 while varying the gravity constant q to 1/6 and 1/36 for lunar and Ceres gravity. This produced a set of test velocities to compare different gravities and predict the power and velocity outcomes in these two reductions of gravity. When gravity and angular velocity are modified but all other quantities are left constant, the relationships reduce to the following:

$$(g', L', M', D', \omega') = (qg, L, M, D, q^{1/2}\omega) \tag{4.5}$$

$$P' = q^{3/2} P \tag{4.6}$$

$$V' = q^{1/2} V \tag{4.7}$$

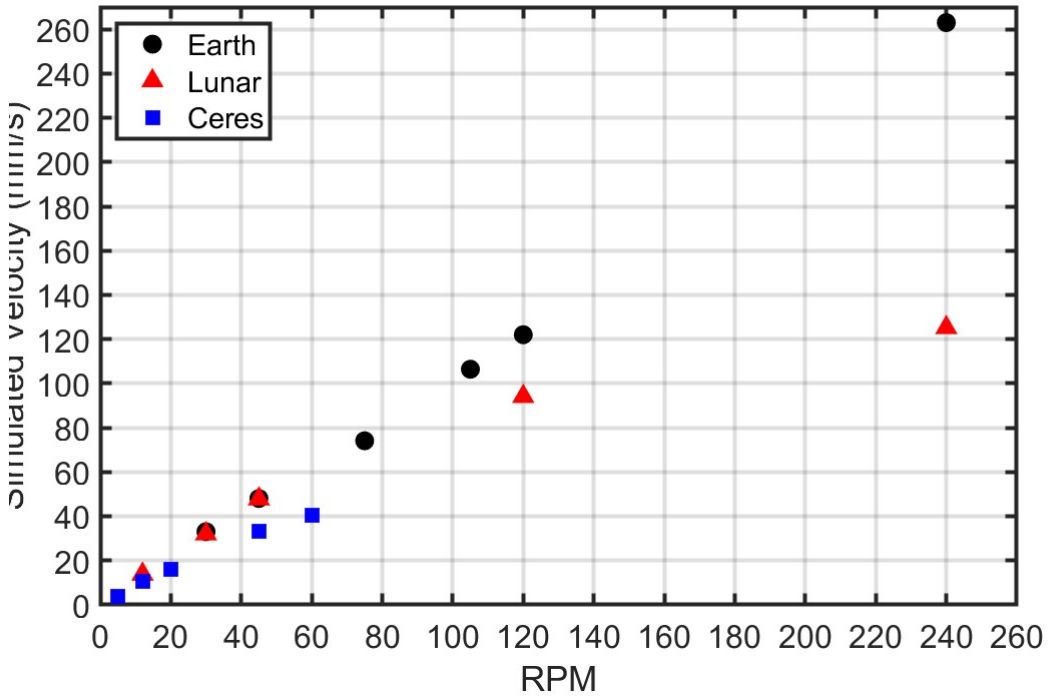

Figure 21. Simulations of identical geometry with three gravity variations

Bearing these scaling laws in mind, speeds were identified for both gravity levels. The simulations were run for three gravity levels. The original simulations at Earth gravity served as the first. The second was lunar gravity (1.62 m/s^2). The third was Ceres gravity (0.27 m/s^2), the largest object in our asteroid belt. This was done because the Earth-moon gravity ratio is very similar to the moon-Ceres ratio (1/6). All EDEM parameters regarding material parameters were kept constant. As can be seen in figure 22, the craft obeyed the predictions set out by the scaling laws for lunar gravity in both velocity and power. Velocity in this case is defined as the translational velocity in the primary direction of travel. Power in this case is mechanical power, the rate of physical work being done by the screws. These are both results which EDEM allows the user to extract on a per-geometry basis. These showed very close

approximations of 102.6%, 105.9% and 102.7% of predicted values for 12, 30, and 45 RPM respectively. The power was also close, with 94.2% 92.1% and 94.4% of predicted values. The perfect prediction lines have been shown in black on these graphs.

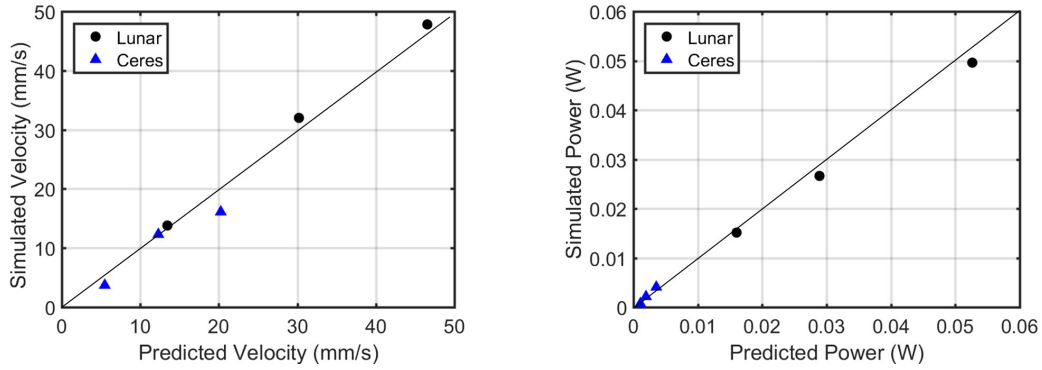

Figure 22. Scaling law predictions versus simulation results

The Ceres gravity resulted in significant variation for predicted values compared to simulated. The 12 rpm case showed a 0.1% deviation from the expected velocity, but the 5 rpm case was 67.5% of predicted value and the 20 rpm case was 79.5% of the predicted value. In the case of power, 62.5%, 109.4%, and 114.9% were the values found as a percent of predicted value. One item to note is that the gravity variation performed in the scaling literature was done so with a gravity increase, not decrease. As such, we believe we encountered a level of gravity low enough that our speeds do not stay in a constant-slip range.

In figure 21, the raw craft velocities versus their rotation speeds are plotted for all gravity levels. While the Earth and lunar gravity simulations show almost identical relationships, the Ceres gravity simulation speeds display a non-linear trend. The trends clearly show further deviation with increased speeds. The lower gravity provides less entrapped granular media to push against.

4.4 Potential Sources of Error

The errors in this chapter fall into two categories. The first set of differences occurs between experimental and simulated craft at Earth gravity. The second occurs between simulated and predicted values at reduced gravity compared to Earth gravity. To address the small but non-trivial differences in experimental validation, it is worth noting the driving physics behind the DEM simulations. Each individual particle was modeled and driven by the listed granular parameters, as well as a Hertz-Mindlin physics model for spherical contact. A typical technique for DEM is to reduce the Young's modulus for faster simulation time. [148]. While the change in Young's modulus from its real-world measured value to a reduced one does show some level of effect on the simulations, the effect appears consistent. This reduced modulus was used for all simulations.

Since the Earth-DEM simulations showed close patterns to experiments, we consider them valid for evaluating scaling law comparisons. They have relatively consistent inflation between their velocity measurements and behaved as expected. The lunar gravity DEM simulations also behaved as expected. However, the Ceres simulations (performed under 3% of Earth's gravity) did not follow predictions. The most likely cause, as is observable from the trends, is that an assumption of constant slip rate is necessary for these laws to work. As gravity is decreased and granular media is subject to weak compaction, the range of speeds in which slip stays constant shrinks considerably and in this case, tested speeds exceeded it.

Chapter 5

PREDICTIVE PERFORMANCE OF GRANULAR SCALING LAWS FOR LIGHTWEIGHT ROVERS

5.1 Abstract

Inspired by recently developed granular scaling laws (GSL) and motivated by the desire to explore improved wheel design for Earth and space applications, we have investigated the performance of both straight grousered wheels and a helical grousered wheel in both silica sand and lunar simulant. Mechanical power draw and velocity of the wheel designs are compared in both materials for performance assessment. The scaling laws were evaluated for Earth gravity experimentally and reduced gravity through multi-body dynamic coupled with discrete element method (MBD-DEM) simulations. Experimental results show a general power prediction error between 20-35% for lunar simulant and 15-25% error for silica sand which was further investigated and explained by several factors that point to scaling law dependency on mass or sinkage. Velocity prediction error showed high dependence on material, with silica sand error generally between 4-10% and lunar analogue varied between 0-27%. The MBD-DEM simulation results match theoretical predictions more closely with power error under 8% and velocity error under 4% for all speeds except slowest. This study presents a set of experiments and simulations which significantly contribute to the ability to design and test rover wheels on Earth and beyond.

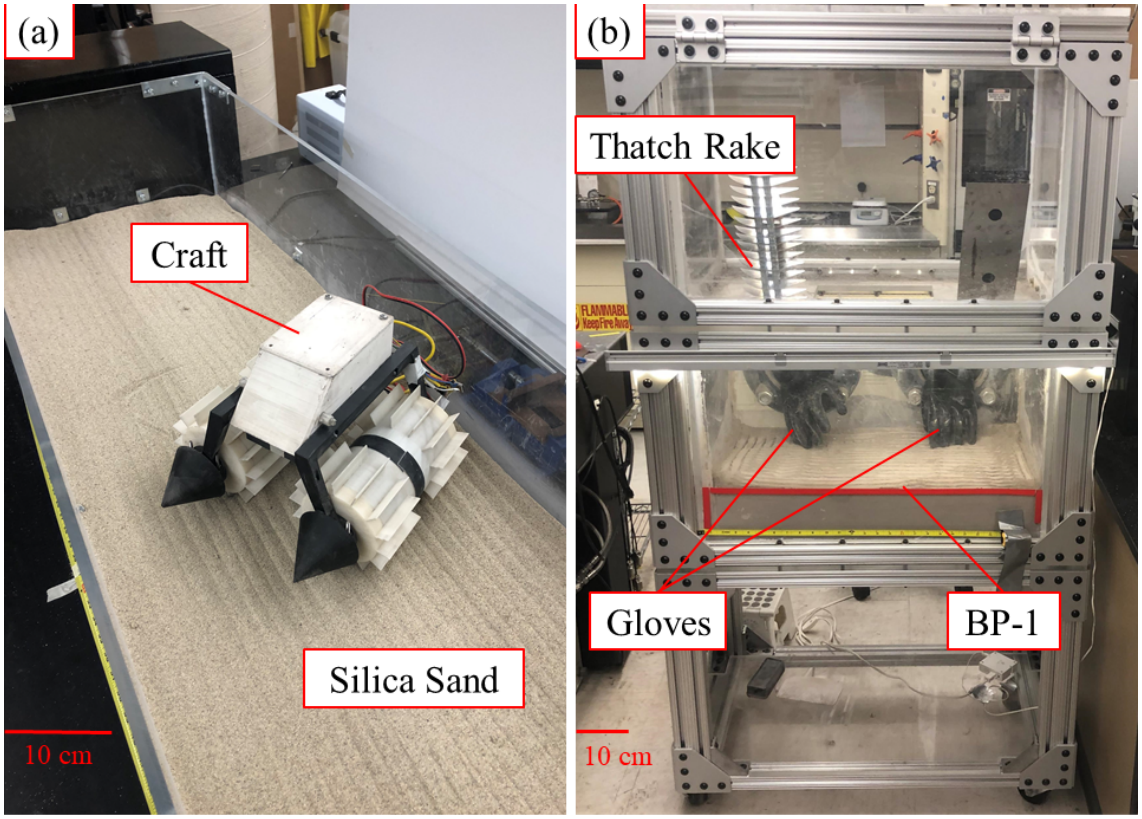

Figure 23. (a) Craft with straight grousered wheels attached in silica sand bed and (b) simulant containment unit with tools displayed.

5.2 Wheel Design Theory

The wheel shapes in this experiment are cylinders with two types of grousers as seen in figure 24. The designations are “GSL” for the theory being evaluated, “1“, “2”, or “3“ sizing as described in Table 3, and “B” or “G“ for bihelix and grouser shape, respectively. The sizing of the three sets is driven by GSL and we will explore why straight grousered wheels are worth validating for these laws and helical grousers are worth exploring as an expansion by discussing a brief derivation of and the assumptions behind these laws.

Figure 24. The wheel sets used in experiments with helical grousers on the left and straight grousers on the right.

The functional expression for GSL is presented in equation 5.1 with parameters labelled on their physical counterparts in figure 25:

$$(P, V) = \psi(d, l, m, \omega, t, f, g, \rho, \mu, \mu_w) \tag{5.1}$$

The geometry is described by the wheel's characteristic length (radius or diameter) l, its depth into the page d, its mass m, a driving rotational velocity ω, and a consistent shape outline of points f. These physical characteristics are changed for the sizes of "1", "2", and "3". The environment is described by gravity g and the granular characteristics ρ, μ, and μ_w; these are density, internal friction, and wheel-grain

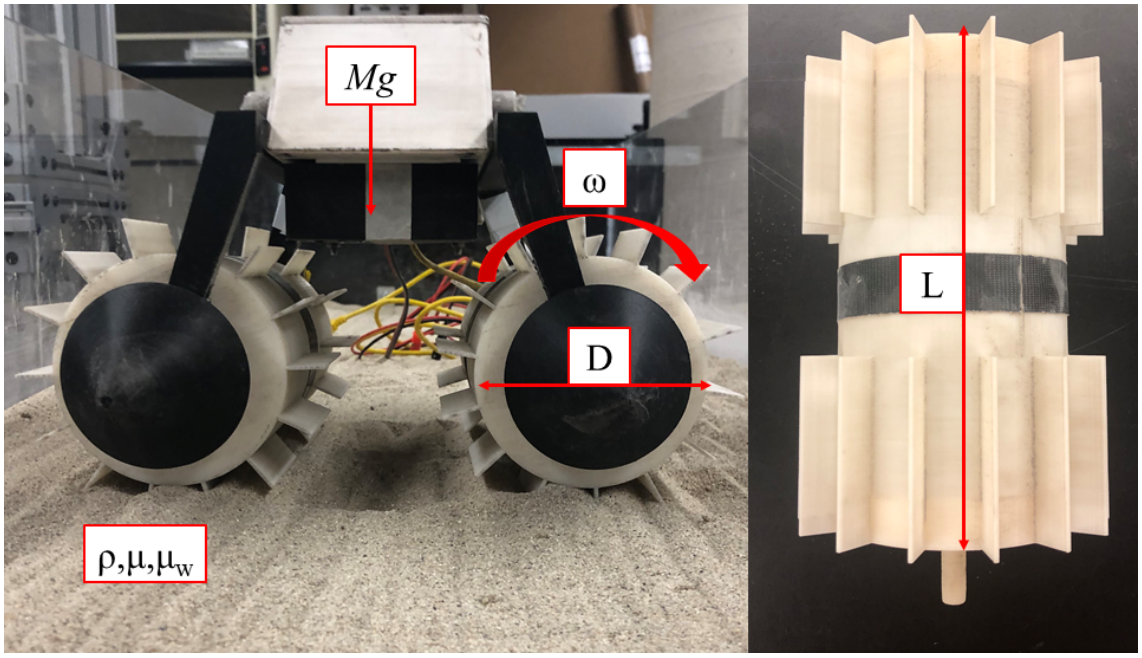

Figure 25. Granular scaling parameters labelled for craft and straight grousered wheel.

friction, respectively. They are constant and occur as a function of the granular environment and its interaction with the geometry. In our case, Quikrete and BP-1 will have different characteristics and this is why we can only predict the performance of a larger wheel from a smaller one in the same material.

The results we are interested in are power P and translational velocity V. The system is dependant on time, t, and under experimental trials the time-averaged outputs are discussed. By using non-dimensional analysis and a careful set of assumptions, the result is as follows [134]:

$$[\frac{P}{Mg\sqrt{Lg}}, \frac{V}{\sqrt{Lg}}] = \Psi(\sqrt{\frac{g}{L}}t, f, \frac{g}{L\omega^2}, \frac{DL^2}{M}) \tag{5.2}$$

Equation 5.2 includes gravity as a potential variable. We change gravity in our simulations; however, during experiments we utilize the gravity-invariant laws that are simplified as follows:

$$[\frac{P}{M\sqrt{L}}, \frac{V}{\sqrt{L}}] = \tilde{\Psi}(\sqrt{\frac{1}{L}}t, f, \frac{1}{L\omega^2}, \frac{DL^2}{M}) \tag{5.3}$$

If a wheel with the inputs of (L, M, D, ω) is compared to a wheel affected by positive scalars r and s, the predicted relationship $(L', M', D', \omega') = (rL, sM, \frac{s}{r^2}D, \frac{1}{\sqrt{r}}\omega)$ follows. The conclusion is that one should be able to predict the time-averaged power and translational velocity of a rotating wheel with the following relationships:

$$P' = s\sqrt{r}P \tag{5.4}$$

$$V' = \sqrt{r}V \tag{5.5}$$

Equation 5.4 and equation 5.5 rely on various assumptions. One of the original assumptions which is tested in our trials is that of depth-variance. Recall that f is the symbolic representation of the wheel's consistent outline. GSL simplicity arises partially because of the assumption that the wheel shape outline does not vary with D, allowing the stress functions on the wheels surface from reaction forces with the grains to integrate as a continuous simple function. This allows force in the direction of travel and vertical force to be predictably scaled in both size or number. For example, under these constraints, if the mass M and thickness D of a single wheel were both scaled by some integer n, the resulting wheel would draw nP power. This would hypothetically allow vehicle performance under simple dynamics to be predicted by evaluation of a single smaller wheel.

5.2.1 Design of Straight Grousered Wheels

Grousers are a standard feature for field robotics on Earth and beyond. The shape of a straight grousered wheel adheres to the assumption of depth-invariant shape for

the scaling laws. Yet research indicates that the motion gains or slip reduction of grousered wheels in soils are possibly due to a "soil sweeping" effect rather than a thrust force increase from the grouser [155, 156]. This effect causes a pre-clearing of granular material in front of the leading wheel edge before it makes contact. This lowers contact angle between wheel and soil wall and reduces the motion resistance effect of the media. We propose it is valuable to investigate GSL applied to a grousered wheel because while the outline adheres to the assumptions, this geometry-specific effect may prevent parameters from scaling properly. The minimum number of grousers necessary was determined by the following equation [157]:

$$\Phi < \frac{1}{1-i}(\sqrt{(1+h)^2-(1-z)^2} - \sqrt{1-(1-z)^2}), \tag{5.6}$$

where Φ is the spacing required between the grousers in radians, i is estimated slip, h is grouser height, and z is estimated sinkage. To ensure the next grouser encounters soil before the wheel rim does, the placement of grousers around the wheel must be Φ radians or less. In our case, fourteen was the minimum required to clear material from the contact edge under 20% slip and approximately 2 cm of sinkage, our beginning estimates for the smaller sizes.

5.2.2 Design of Bihelix Grousered Wheels

Studies [158] indicate that a very wide angle with at least one grouser engaged at all times is most effective at generating drawbar pull force in a deformable tissue environment. The granular physics behind why these wheels work deviates from that of traditional grousers. Straight grousers pre-clear material to avoid more resistive piles ahead of the round wheel shape. In contrast, helical grousers rely on the kinematic

coupling in a helicoid shape between rotational and translational motion. As the wheel turns in granular media, the local surface geometry will appear to translate along the axis of rotation. This results in an outward pushing force against the interlocked grains perpendicular to the direction of travel. This translational resistive force contributes to the shear force which generates forward motion in the wheel, impacting the resultant slip. The outcome in the media is a continuous 2D projection of the 3D wheel, seen in figure 26.

Figure 26. Impression patterns left by helical grousers on both granular media (BP-1 on the left and Quikrete on the right).

Several design considerations went into the creation of the bihelix wheel. One was winding direction; all impacts being equal, we favored a helix shape which would tend to push material outwards, away from the wheel. We chose four helix windings, equally spaced around the wheel, to increase media engagement. The non-grousered space in the center was to avoid any interaction between helices or force concentrators where the blades would meet. All wheels, GSLG and GSLB, were printed on a Stratasys Mojo printer, with ABS, and assembled in halves and can be seen in figure 24.

As previously stated, a fundamental GSL assumption is uniformity of wheel shape along the axis of rotation. Explicitly, the arbitrary wheel shape outline is acceptable

as long as it is uniform in this direction. A helical geometry will violate this and it is worth evaluating what level of deviation may be present. For a direct comparison of the grouser performance, the scaling of the wheel base was kept consistent between both wheel types; size is identical and mass differences are trivial between sets. The blade thickness and length of the helix are equal to the straight grouser thickness and length for each respective set. All target dimensions are listed in Table 3; mass is in kilograms and length in centimeters.

Table 3. Properties of Straight Grousered and Bihelix Grousered Wheels

Design	**Diameter**	**Mass**	**Length**	**Grouser**	ω **(RPM)**
GSL1-G	7.5	1.459	14	1.25	15,30,45,60,75
GSL2-G	11.25	2.594	14	1.875	13,26,39,52,65
GSL3-G	9.375	2.918	18	1.5625	14,27,40,54,67
GSL1-B	7.5	1.477	14	1.25	15,30,45,60,75
GSL2-B	11.25	2.626	14	1.875	13,26,39,52,65
GSL3-B	9.375	2.954	18	1.5625	14,27,40,54,67

Using test parameters for both wheel shapes found in Table 3, the predicted power of the GSL2 sets should be approximately 205% (that is, double) of the GSL1 sets. The velocity should also be 115% of GSL1 velocity. For the GSL3 sets, the power should increase to 224% and velocity increase to 112%. If BP-1's properties lend themselves to scaling, we should see similar results in both granular media.

5.3 Methods to Evaluate GSL Performance

5.3.1 Development of BP-1 Simulant Containment Unit

Since BP-1 has high particle interlock, it is sensitive to plastic deformation memory. For comparison, Quikrete medium used in experiments is a silica sand which is kilned,

sieved, and washed. It is the original material used in the GSL literature and has particles primarily 0.3-0.8 mm in size. It is important to compare the performance of GSL in a lunar simulant against a more conventional silica sand to evaluate the feasibility of using these laws for lunar design. Preliminary Earth testing of Mars Curiosity Rover traversability shows the variability in wheel performance and interaction which can occur in different types of granular media [27].

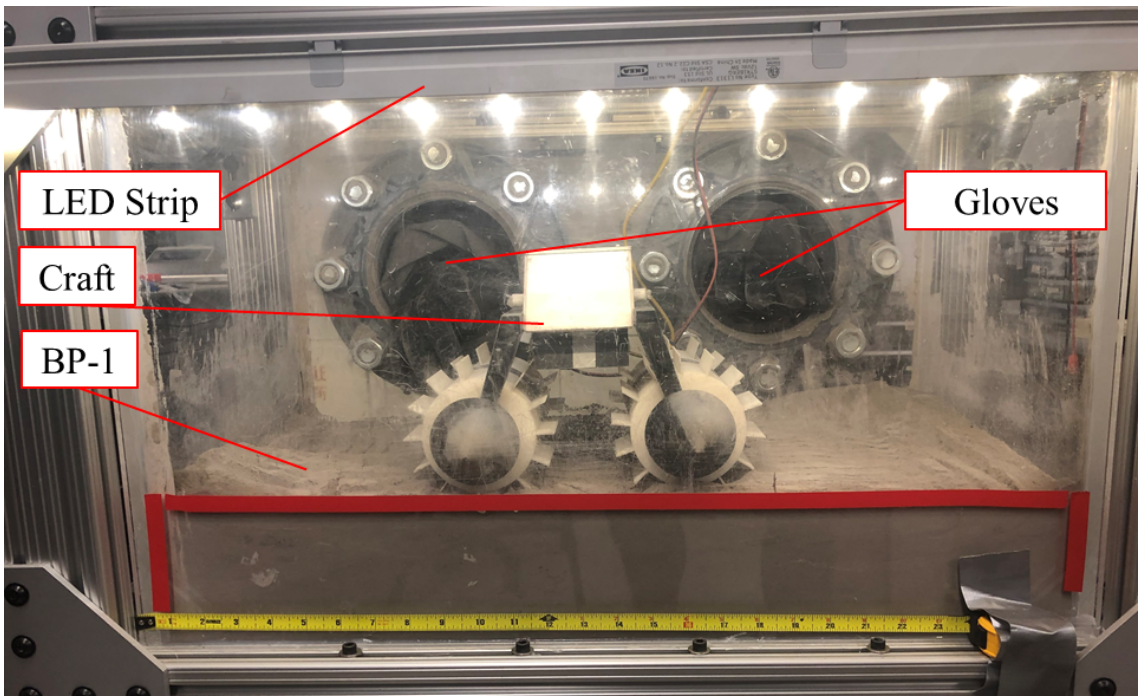

Figure 27. BP-1 testing chamber with craft inside and components labelled.

While BP-1 is generally harmless when undisturbed, it does present an occupational hazard when dusted in a confined space. Therefore, testing of lunar simulants are typically performed with some level of containment. A custom-made simulant containment unit is shown in figure 23 and figure 27. It is complete with sealed chemical glove holes for tool and craft manipulation, and deformable rubber sealing on the box lid to allow for power and control cables. A bar of LED lights helps with visual

tracking conditions. The simulant bed has 37.5 cm × 67.5 cm interior dimensions. The box was created using commercially available acrylic and aluminum. Simulant containment units such as this setup provide a solution to obtain "field" results in such materials.

5.3.2 Design of Concentrically Embedded Motor Transmission

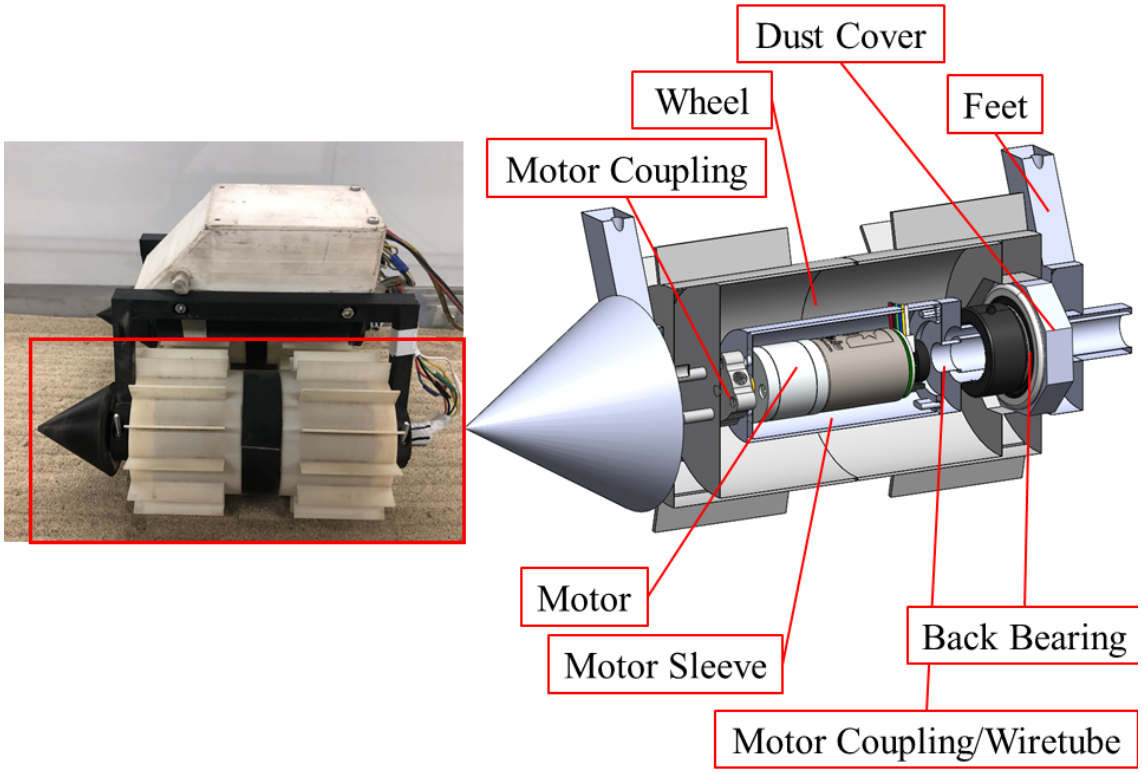

Figure 28. Experimental craft with internal cutaway in Solidworks illustrating the power transfer mechanisms.

The craft was designed to be multi-purpose, allowing the wheels to be easily interchanged. A modular undercarriage weight holder was added to the bottom of the craft to adjust total mass for scaling. Craft height was adjusted to keep center of

gravity as low as possible without interfering with the wheels. Furthermore, the wheel mount width was designed to prevent the granular flows from each wheel actively interfering with the other during craft operation. The craft is pictured in figure 28 along with a Solidworks model of the internal concentric mechanisms. Trade studies indicate that an internal motor drivetrain is optimal due to the dusty nature of the operational environment. Any external belt or chain drive system would be susceptible to dust accumulation and not typically used on rover vehicles for space applications. A 12 V DC motor is fastened to its housing, the motor sleeve, via two small screws. A wiretube with four radially symmetric pegs pressure fits into a cutout pattern at the back end of the motor sleeve. The tube shape transitions to a hexagonal one, and this hexagonal tube is then locked to the feet of the craft to create a single rigid body. Shaft power is transmitted from the motor output shaft to the wheel hull through an aluminum set screw D-hub coupling. Thus, the power is transferred to the wheel body and the motor is held static by the rigid body of the wiretube mounts.

The unit relies on two bearings for rotation. The front bearing (not shown in figure 28) is pressure fit onto the front wheel shaft. These shafts can be seen on the wheels' tops in figure 24. The back bearing, a collar bearing, is affixed to the circular portion of the wiretube with a set screw. This collar bearing is pressure fit into an octagonal dust cover which seals the wheel cavity from BP-1 ingress. The dust cover also mates the bearing and wheel together and allows the wheel to spin around the static wiretube.

The main electronic components are comprised of an Arduino Uno R3, Pololu MC33926 dual motor driver, and one current sensor and wheel encoder per motor. The dual motor driver enabled the craft to adjust the voltage with response from an Arduino PID controller. In addition, Hall effect linear current sensors were implemented per

motor immediately before input power. All electronics were enclosed and sealed in the craft body to minimize exposure to BP-1 dust.

5.3.3 Experimental Setup and Procedure

Experiments were performed either in the simulant containment unit (BP-1) or a 80 cm $\times$ 250 cm sandbox (Quikrete). Experiments for either material began by tilling the soil with a handheld thatch rake to ensure no large soil stresses were present. Tilling was performed by the same team member for all 720 trials to ensure consistency. Craft was placed on top of either the BP-1 or Quikrete at one end of the respective test bed. The power supply was engaged and the craft completed a trial. The trial was recorded by both Arduino serial monitor for power and video camera for velocity. The simulant containment unit is equipped with a LED light strip so that the moving craft is clearly visible in the video as dusty conditions occur. Camera location and settings were kept consistent between all trials for each material. Blocks of color attached to all sides of the craft were used to enable its tracking. Lighting was kept consistent in order to keep tracking as accurate as possible. Utilizing the videos and a MATLAB based color tracking program, position versus time was determined and analyzed for each trial. The instantaneous velocity was calculated and used to evaluate steady state velocity per trial. Mechanical power was evaluated using in-line hall-effect current sensors to obtain individual current readings from each motor. Using the motor constant, current was converted to torque. The time-averaged torque and rotational speed were multiplied during steady state bands to produce time-averaged power.

A total of 12 trials were performed for each set of speeds, five speeds were chosen for each wheel, and a total of six different wheel shapes were run in the two materials.

The craft was equipped with a removable mass box which held the proper amount of weights needed for each wheel shape. Each set of pontoons were weighed so that the total amount of mass for an unweighted craft was known. GSL1 trials were run without the box. When running GSL2 and GSL3 trials of either shape, mass was added in the box to meet the scaling requirements.

5.4 Results and Discussion

5.4.1 Empirical Performance of Wheels in Quikrete and BP-1

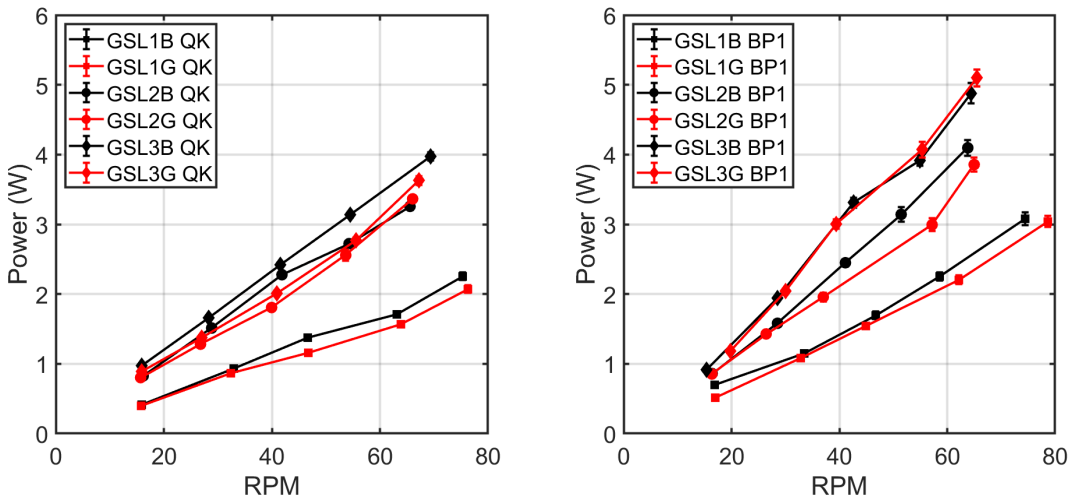

Figure 29. Comparison of craft power draw in the two materials, Quikrete on left and BP-1 on right.

Power draw data plotted in figure 29 indicate that the traditional grouser shape drew slightly less power than the bihelix grouser for all three sizes. This was true for both materials with the only notable exceptions being the two fastest speeds in

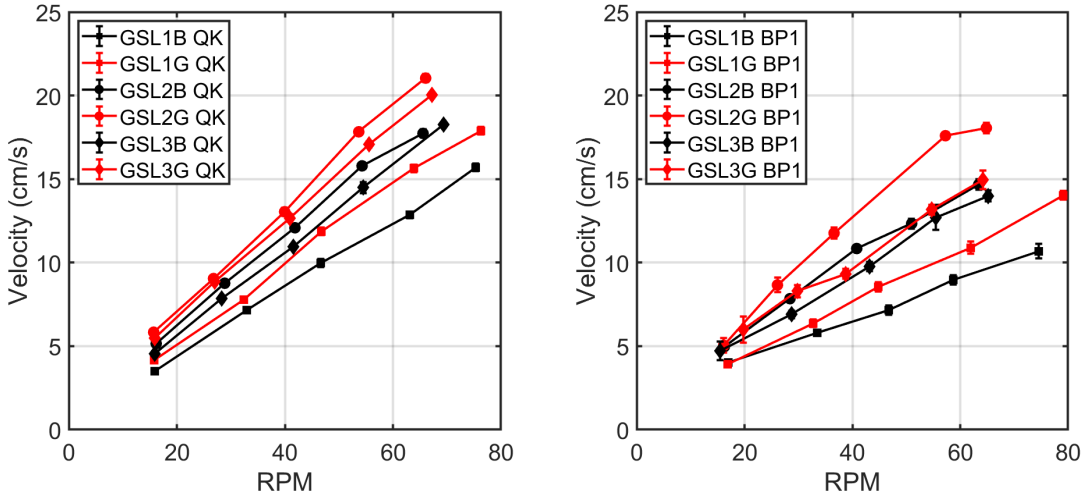

Figure 30. Comparison of craft velocity in the two materials, Quikrete on the left and BP-1 on the right.

BP-1 at the heaviest wheel size. It is worth bearing in mind that the bihelix design has not been optimized but still showed relatively similar trends to straight grousers in most BP-1 cases. Shape optimization, number of helices, grouser length, among other design factors are worth exploring, especially at a higher mass, slip, or sinkage. Chevron grousers have found success in low slip conditions [159] and are used on the Curiosity rover, and it would be a worthwhile future exercise to further investigate shape advantage in Martian or lunar regolith.

Straight grousers also resulted in higher velocity than bihelix wheels. Trends are seen in figure 30 with the GSLG sets generally shifted higher than GSLB regardless of size. This is displayed very plainly in the Quikrete experiments in addition to the "1" and "2" sizing in BP-1. However, the "3" sizing, the heaviest, shows a much narrower difference. This was also the set with nearly identical power draw for GSLG and GSLB.

5.4.2 Mechanical Power Ratio Relationship to Granular Material, Grouser Shape, Rotational Speed, and Motor Placement

The central benefit behind GSL is the ability to predict large vehicle results from smaller ones. This can be expressed as a power or velocity ratio. For our study, the "2" and "3" size designations should result in power ratios of 2.05 and 2.24, respectively. Neither of these were fully reached; errors indicated that the larger crafts did not draw as much power as predicted. This is possibly explained by hidden mass, pressure, slip, or sinkage dependencies which are discussed in the last section of this chapter and supplementary material. However, the ratios did show differentiation between experimental factors as seen in figure 31. For a set to be correctly predicted by GSL, all data ought to fall on the black line.

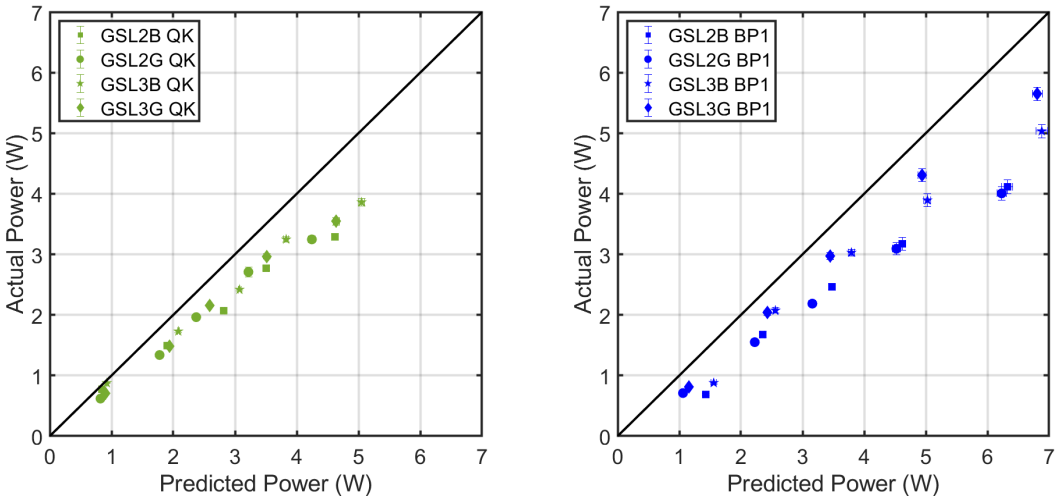

Figure 31. Predicted power versus actual power consumption with black line indicating perfect prediction. Quikrete on the left and BP-1 on the right.

Higher error is present in all four shapes for the lunar simulant than Quikrete. Errors for all but the lowest speeds were 29-35%, 19-27%, 30-36%, and 13-17% for 2B,

3B, 2G, and 3G. Error for the slowest speeds of each set were 52%, 44%, 33%, and 30%, respectively. Conversely, the silica sand remained relatively consistent in level of error across sets. It also saw a much lower error in general. Errors for all speeds were 9-29%, 5-24%, 16-25%, and 16-24% for 2B, 3B, 2G, and 3G, respectively. Both the "2" and "3" sizes appear to have similar trend in moving further away from the line with higher power draw, and indeed the furthest points are the fastest speeds in BP-1 for both sizes. However, it is apparent that the heavier of the two sets, "3", resulted in lower error for both shapes in BP-1. We will also note that the data for GSL2G and GSL3G in Quikrete, the material used in original GSL testing, were remarkably consistent in power ratio error. While we saw prediction errors of 15-25% across speeds, their values at each speed held a difference of less than 1% except for the slowest speed.

After examining the comparisons, one concludes that the shape of the grouser made little difference in this set of experiments, that the larger mass difference in the "3" case made them marginally more accurate, and in general, BP-1 showed more error than Quikrete. In all cases, the data deviated from the prediction line with increased speed. Notably, this means that despite the error, the bihelix shape generally conformed to the scaling laws as well as straight grousers and BP-1 was only marginally worse than Quikrete in predictive results.

Preliminary investigations into how the mass or velocity envelop may affect the scaling laws [160] provide an explanation and feasibility criteria. An interesting point of note is that linear regression of the power error compared to craft mass was very similar for this chapter's straight grousered wheels in Quikrete compared to the above study. Thoesen *et al.* study predicted a total elimination of error for grousered wheels in silica sand at 8 kg and this one predicts it at 9 kg [160]. The mass scalar in those

experiments was 1.778 for all sets. In our study, 1.778 and 2.0 are used. In the Slonaker *et al.* study, mass scalars were 2.18-2.40 [134]. The scalars may have a limit of applicability per soil. Other potential sources of error which were examined and ruled out include the current-torque constant, wheel size, and effects of grouser power reduction difference at sizes. One remaining comparison to make would be to run identical mass and wheel size tests with a single wheeled gantry versus dual wheeled craft. It is possible that the unconstrained wheeled craft dynamics create non-trivial effects in predictive abilities for power.

5.4.3 Velocity Ratio Relationship to Granular Material, Grouser Shape, and Rotational Speed

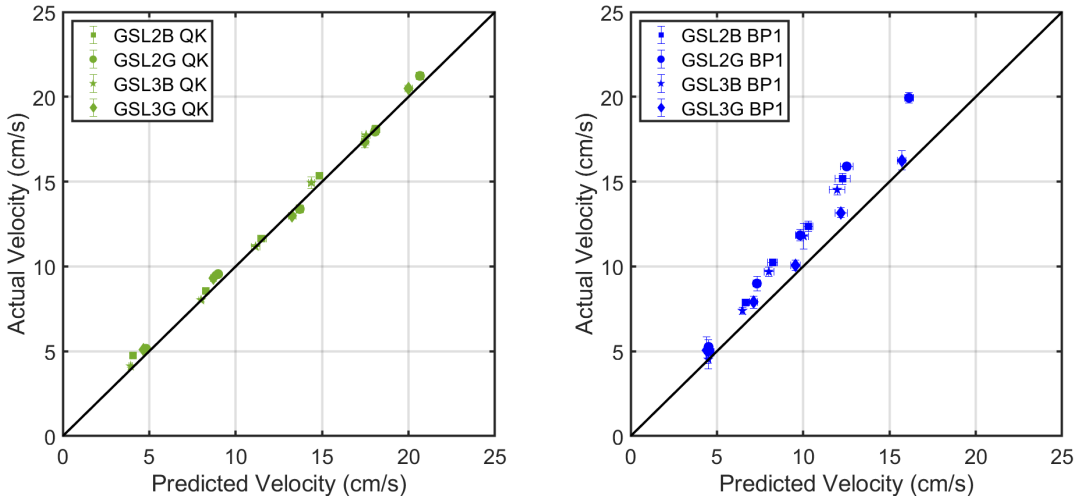

Figure 32. Predicted velocity versus actual velocity achieved with black line indicating perfect prediction. Quikrete on the left and BP-1 on the right.

Differentiating the velocity ratio prediction found by material yields a much starker contrast than the power predictions (figure 32). In BP-1, the error for 2G, 3G, 2B,

and 3B was 17-27%, 3-15%., 7-24%, and 0-21%, respectively. In all cases, the larger and heavier craft moved faster than predicted and this trend generally increased with wheel speed. For the Quikrete, results were much closer in both accuracy and precision. The GSL2G set contained error in the 0.6% to 6.8% range, the GSL3G in 0.8-9.1%, GSL2B in 0.1-3.8% for all but the lowest speed (17%), and GSL3B in 0.1-4.9% across the entire set. If we restrict the range to the three fastest speeds, all comparisons have error below 4%.

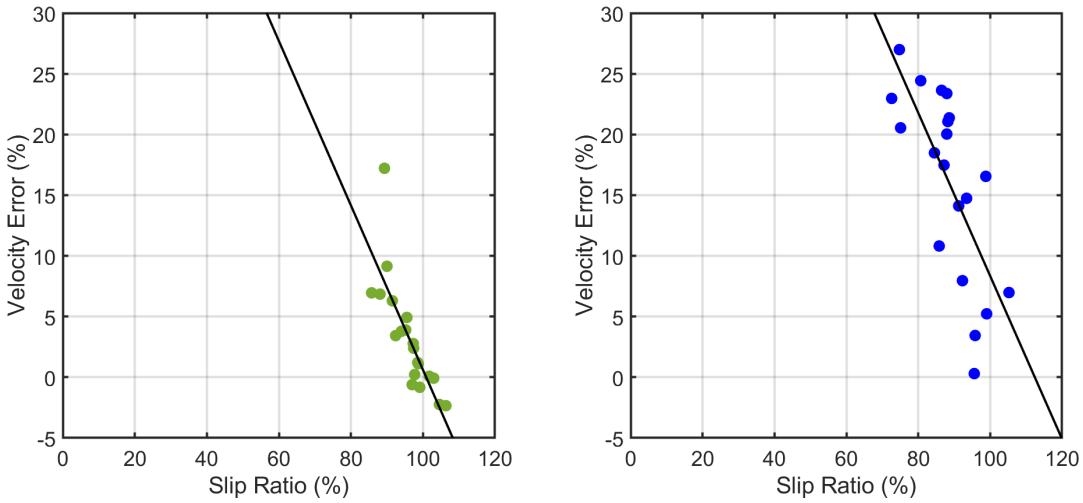

Figure 33. Velocity prediction error as a function of slip ratio with regression line. Quikrete on the left and BP-1 on the right.

Interestingly, we show the percentage difference in slip matches the velocity errors as it ought to in Quikrete. Slip is the amount of rotation which is not transformed into translational motion. A wheel rotating on a surface under no slip conditions, for example, would translate a distance of its circumference for each rotation. If it translated 80% of its circumference, it is experiencing 20% slip. Performing the same slip comparison in BP-1, we see an insight to explain our high BP-1 error in figure 33. An unstated assumption of the granular scaling laws is constant slip between

comparative datapoints. This is implied but not explicitly stated in the original laws that a relatable slip-sinkage relationship exists between the two sets. That is, the mass difference induces a sinkage which necessarily generates the same level of slip between the two sizes. We see that for Quikrete, error between slip and velocity clearly trends towards 0% velocity error for 100% slip ratio. The BP-1 trends are much less apparent, and the general scatter of the data indicates that there may be some environmental effects occurring due to the unique material properties of BP-1. This needs to be further explored in future studies. What appears to be true for Quikrete is that a slip-sinkage criteria could possibly predict where the envelope for GSL feasibility occurs. We also emphasize that translational velocity error was significantly lower than power error because velocity was the driving variable; we set the target rotation and drew the necessary power to achieve it. Assuming relatively consistent slip conditions, the velocity would be very close. Regardless, we see consistent velocity prediction with the largest differentiator being material, and a slightly more accurate prediction with straight grousers in BP-1 than the helices.

5.4.4 MBD-DEM Simulations for Gravity-Variant GSL

Environments where scaling predictions hold significant application include bodies of different gravity. The closest and most visited target is that of Earth's moon; this provides an environment that has been studied extensively. The gravity is roughly 1/6 of Earth's, a suitable order of magnitude for evaluating the laws. Simulations as a design tool become useful because the results of studies comparing reduced weight rovers in earth granular media experiments versus identical experiments performed on parabolic flights with direct gravity variation have shown significant differences

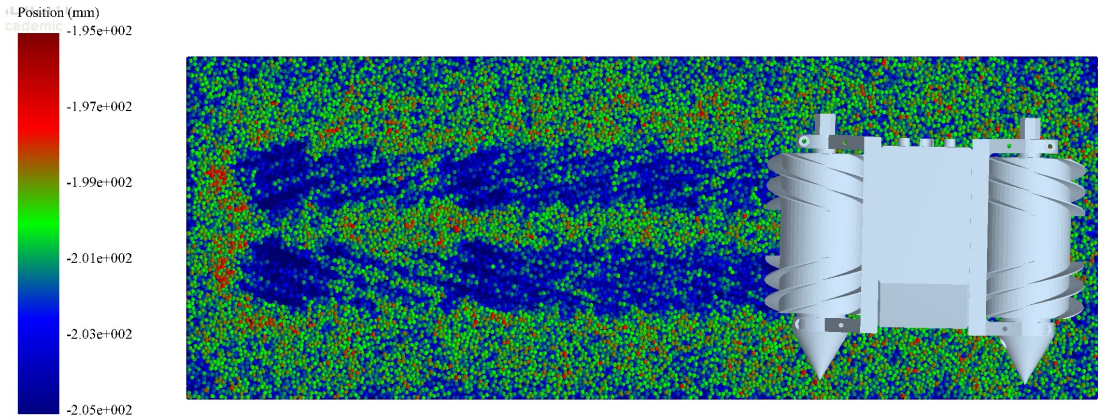

Figure 34. Top view of a MBD-DEM simulation with grouser marks color coded by depth.

[47, 48]. In some cases, the trends are actually inverted; granular compaction due to gravity plays a significant role in granular physics for rover motion. It is therefore of great interest whether tests at Earth gravity could be theoretically extrapolated to predict performance in lower gravity environments. Recall the earlier scaling equations for power and velocity. We now address the conclusion of the gravity-variant version. If a wheel with the inputs of (g, L, M, D, ω) is compared to a wheel affected by positive scalars r, s, and q the predicted relationship $(g', L', M', D', \omega') = (qg, rL, sM, sr^{-2}D, q^{1/2}r^{-1/2}\omega)$ follows. The conclusion is that one should be able to predict the time-averaged power and translational velocity of a rotating wheel even in a different gravity with the following relationship:

$$P' = q^{3/2}r^{1/2}sP \tag{5.7}$$

$$V' = (qr)^{1/2}V \tag{5.8}$$

Due to the computationally demanding nature of these simulations, we selected the bihelix wheel, the GSLB set, to perform in as close a match to the lunar soil as

possible. We reference the properties given in Chapter 2, table 1, and we note here that the results seen are not directly comparable to BP-1. The properties of this artificial granular material match that of BP-1 or basalt as best found in the literature with the exception of particle size and Young's modulus; these were altered since they play a direct role in computation time. GSL2B/3B power and velocity are compared to their predictions in figure 35. To our knowledge, this is the first evaluation of GSL for a fully three-dimensional MBD-DEM rover simulated in a target gravity and environment.

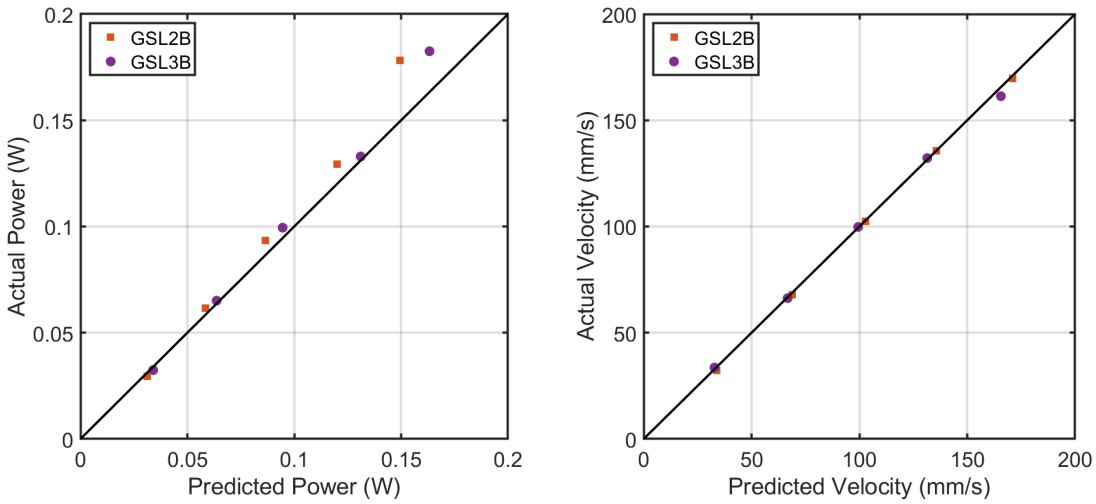

Figure 35. Simulation results paired with their respective predictions with solid black line indicating perfect prediction.

The results indicate a close match with the gravity-variant scaling laws for both power and velocity ratios. In the GSL2B scaling, every datapoint but that of fastest speed showed scaling prediction of power with 5-8% error. In the GSL3B scaling, every speed but the fastest showed scaling with 1-5% error. The fastest speeds had 19% and 12% error in GSL2B and 3B, respectively. In all but the slowest cases, the error was positive; that is, the craft drew more power than predicted during the lunar

gravity cases. The majority of velocity scaling predictions were at less than 2% error; GSL2B error was below 2% for all but slowest speed (5%) and GSL3B ranged from 0.2%-3.3%. We conclude that GSL with gravity variance can be seen as a reliable design tool for evaluating small craft in lunar gravity.

Chapter 6

REVISITING SCALING LAWS FOR ROBOTIC MOBILITY IN GRANULAR MEDIA

6.1 Abstract

The development, building, and testing of robotic vehicles for applications in deformable media can be costly. Typical approaches rely on full-sized builds empirically evaluating performance metrics such as drawbar pull and slip. Recently developed granular scaling laws offer a new opportunity for terramechanics as a field. Using non-dimensional analysis on the wheel characteristics and treating the terrain as a deformable continuum, the performance of a larger, more massive wheel may be predicted from a smaller one. This allows for new wheel design approaches. However, robot-soil interaction and specific characteristics of the soil or robot dynamics may create discrepancies in prediction. In particular, we find that for a lightweight rover (2-5 kg), the scaling laws significantly overpredicted mechanical power requirements. To further explore the limitations of the current granular scaling laws, a pair of differently sized grousered wheels were tested at three masses and a pair of differently sized sandpaper wheels were tested at two masses across five speeds. Analysis indicates similar error for both designs, a mass dependency for all five pairs that explains the laws' overprediction, and a speed dependency for both of the heaviest sets. The findings create insights for using the laws with lightweight robots in granular media and generalizing granular scaling laws.

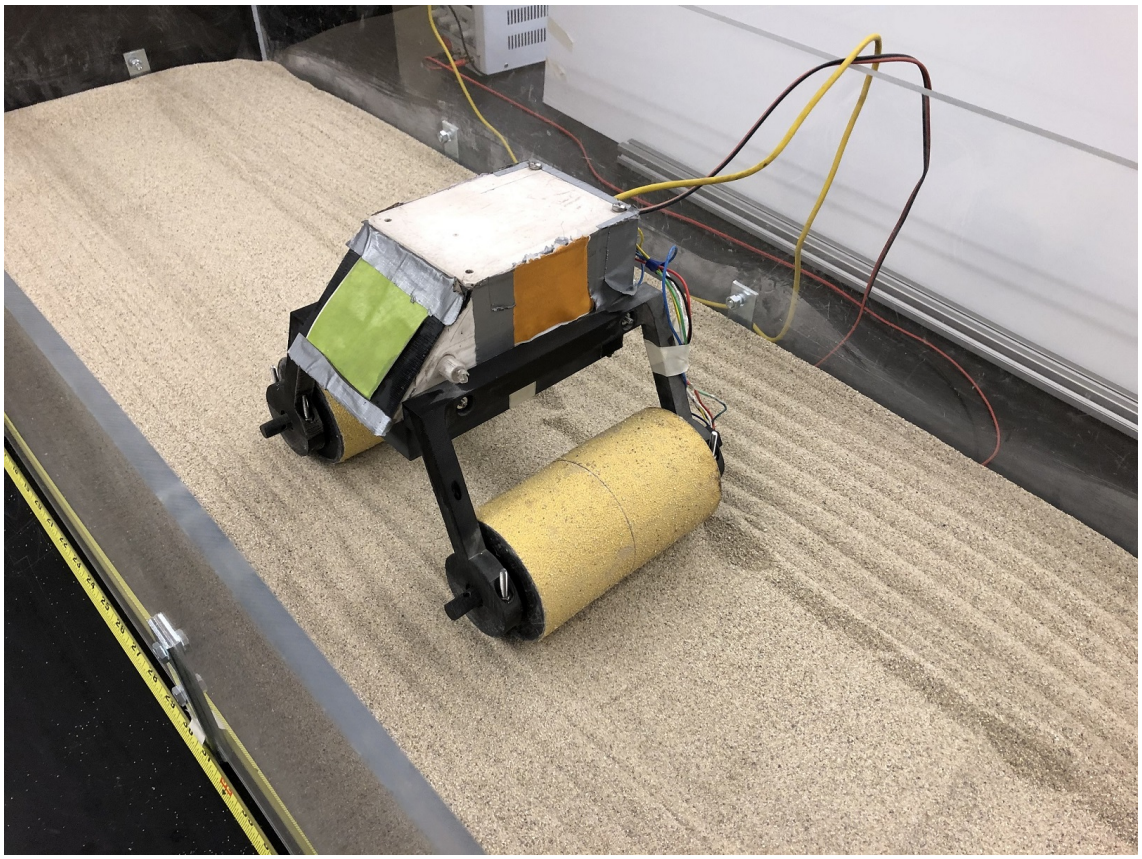

Figure 36. Craft with small sandpaper wheels.

6.2 Granular Scaling Laws

This study examines the performance of a lightweight rover equipped with sandpaper wheels for direct comparison to established scaling experiments and grousered wheels to include evaluation of a commonly utilized shape. Wheel grousers are a typical feature for field rovers and to our knowledge, have not been tested for these scaling laws. The grouser design in this study was driven by equations discussed further in this section. We turn first to the dimensions of length, mass, and time which define the wheel and the experiment. The basis of the wheel shape was an ABS

cylinder covered in either 80-grit sandpaper or printed grousers. As a reminder of GSL, we touch upon the definition of parameters again.

We are interested in power P and translational velocity V. These occur as a function of the wheel and its interaction with the environment. The wheel is described by its characteristic length (typically radius) l, its thickness (depth into the page) d, its mass m, a driving rotational velocity ω, and a consistent shape outline f. The environment is described by gravity g and the granular characteristics ρ, μ, and μ_w which are the density, internal granular friction, and wheel-grain friction. The system is dependent on time, t. By using non-dimensional analysis and a careful set of assumptions discussed in the referenced paper, the result is the set of previously mentioned equations 5.1-5.5.

6.3 Experimental Design

The experiments in this study were designed to replicate verified experimental conditions for GSL except for the control variables of interest. One such variable is changing the wheel shape to that of a grousered wheel. One recalls that f is the symbolic representation that the depth-invariant shape of the wheel is consistent through any dimensional changes. The shape of a straight grousered wheel adheres to this assumption for the scaling laws. Previous research indicates that the mobility gains of grousered wheels compared to smooth in soils are most likely due to a change in soil motion, not an increase in thrust [155, 156]. The root cause of this is the "pre-clearing" of granular material in front of the leading wheel edge before it makes contact, thus lowering the contact angle and compaction/motion resistance of the media, rather than addition of thrust from the paddle-like shape as one might infer.

Thus, while the outline of a grousered wheel obeys GSL, and the flow characteristics may scale, the complexities of granular motion to the grousers mean an examination of GSL for this application is necessary.

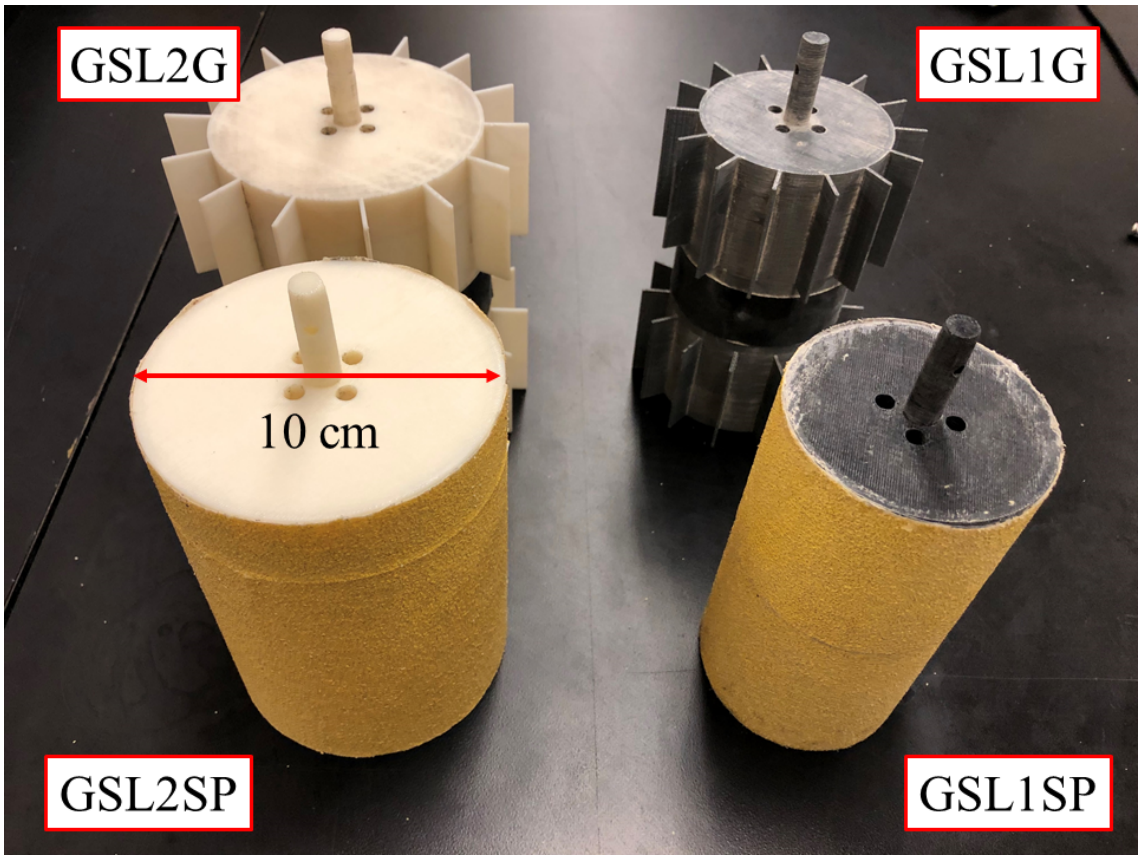

Figure 37. The wheels used in this study labelled with their designations. Grousered wheels of both sizes are seen in the back and sandpaper wheels of both sizes are seen in the front.

The minimum number of grousers necessary to achieve such "pre-clearing" was determined by an equation from the literature [157] with the conservative assumption of 20% slip and approximately 2 cm of sinkage; neither of which appeared reached during experiments. The set of grouser parameters, along with the wheel characteristics, are

shown in 4. The minimum number of grousers required to clear material from the contact edge can be calculated according to the following inequality [157]:

$$\Phi < \frac{1}{1-i}(\sqrt{(1+h)^2-(1-z)^2} - \sqrt{1-(1-z)^2}), \tag{6.1}$$

where Φ is the spacing required between the grousers in radians, i is estimated slip, h is grouser height, and z is estimated sinkage. To ensure the next grouser encounters soil before the wheel rim does, the placement of grousers around the wheel must be Φ radians or less. In keeping with GSL, we maintained the number of grousers between designs when enlarging the shape. The minimum for the smaller wheels was 14 grousers, which also exceeded the necessary number of 13 for larger wheels. The craft was designed to be multi-purpose, allowing wheels to be easily interchanged with other wheel designs. A modular undercarriage weight holder was added to the bottom of the craft. Feet height were designed to keep center of gravity as low as possible without interfering with the granular flow. Craft and sand bed for experiments are featured in 36.

The general dimensions and experimental parameters for these wheels are found in 4 with mass in kilograms and length dimension in centimeters. These classically grousered wheels (GSL1G and GSL2G) use the same wheel sizing as the sandpaper wheels. The sandpaper wheels (GSL1SP and GSL2SP) have an identical body print to the grousered wheels but have 80-grit sandpaper adhered around the entire surface. The two types of wheels are shown in 37. For purposes of simplification, the thickness of the wheel is kept constant between the two sets. The mass and diameter of the wheels were varied according to scaling laws, as were the target RPM's.

For the experiments themselves, we make several assumptions:

1. We assume granular motion in the direction perpendicular to travel, i.e. out of plane is minimal.
2. We assume consistent media; the results of a smaller robot in one granular media should not be used to predict large robot performance in a different media. The relevant granular properties were decomposed into the dimensionless friction coefficient of wheel-sand interaction, the internal friction, and the expression for density. Assuming all three are consistent in the media, we eliminate the frictions and remove ρ from our equations.
3. We assume constant gravity, and use the gravity-invariant laws.

Table 4. Properties of grousered and sandpaper wheels.

Name	**Diameter**	**Masses**	**Depth**	**Grouser**	ω **(RPM)**
GSL1G	7.5	1.46, 2.19, 2.92	14	1.25	15,30,45,60,75
GSL2G	10	2.59, 3.84, 5.19	14	1.667	13,26,39,52,65
GSL1SP	7.5	1.46, 2.92	14	N/A	15,30,45,60,75
GSL2SP	10	2.59, 5.19	14	N/A	13,26,39,52,65

The experiments were performed in the sand bed shown in 36. The bed itself is an acrylic box of 2 meters long and 40 cm wide with 10 cm depth of sand. The sand is Quikrete medium, a well-characterized construction sand. The craft is driven by a wired power supply. This feeds into a motor driver, which distributes the load through a current sensor to each 12 V motor. This process is controlled by an Arduino Uno microcontroller board and the data of the motor encoders and the current sensors are fed back to this microcontroller.

The mass was adjusted to the required amount for each wheel set. The craft was placed at one end of the box, set to run at a specified target speed, and allowed to

travel from one end to another. After each trial, the sand was tilled with a thatch rake in the direction of travel to prepare the sand consistently for each experiment. Ten trials were performed for each set of wheels at each of the five different rotational speeds. All hardware was consistent between trials aside from the wheels and the added mass.

The no-load current of each individual motor was measured with benchtop testing. This current was subtracted from the measured motor load to estimate the torque value from the current-torque relationship of the motor during runs. This relationship is a function of the physical design of the motor and was provided by the manufacturer. By using this torque estimation and the measured rotational speed, the mechanical power of each set was estimated.

Examining the test parameters in 4 for both wheel shapes, we see that the large set diameter is scaled by 1.333 compared to the smaller set. The large set mass is scaled by the square of this, 1.778, compared to the mass of the smaller sets. This leads to identical thickness in the smaller and larger wheels and means the predicted power of the GSL2 sets should always be at a ratio of 2.05 to that of GSL1. If this holds true, the scaling laws are accurate for lightweight wheeled rovers in granular media. These evaluations also require that the larger sets occur at specific speeds. Using a PID controller, we ensured speeds were very close to those targeted (within 3% error). Upon observing a linear relationship between the mechanical power and speed, we used a linear regression and the target speed to estimate the power at the exact speed the scaling laws required for comparison.

6.4 Results and Discussion

6.4.1 Mass/Pressure Dependence of Wheeled Granular Scaling Laws

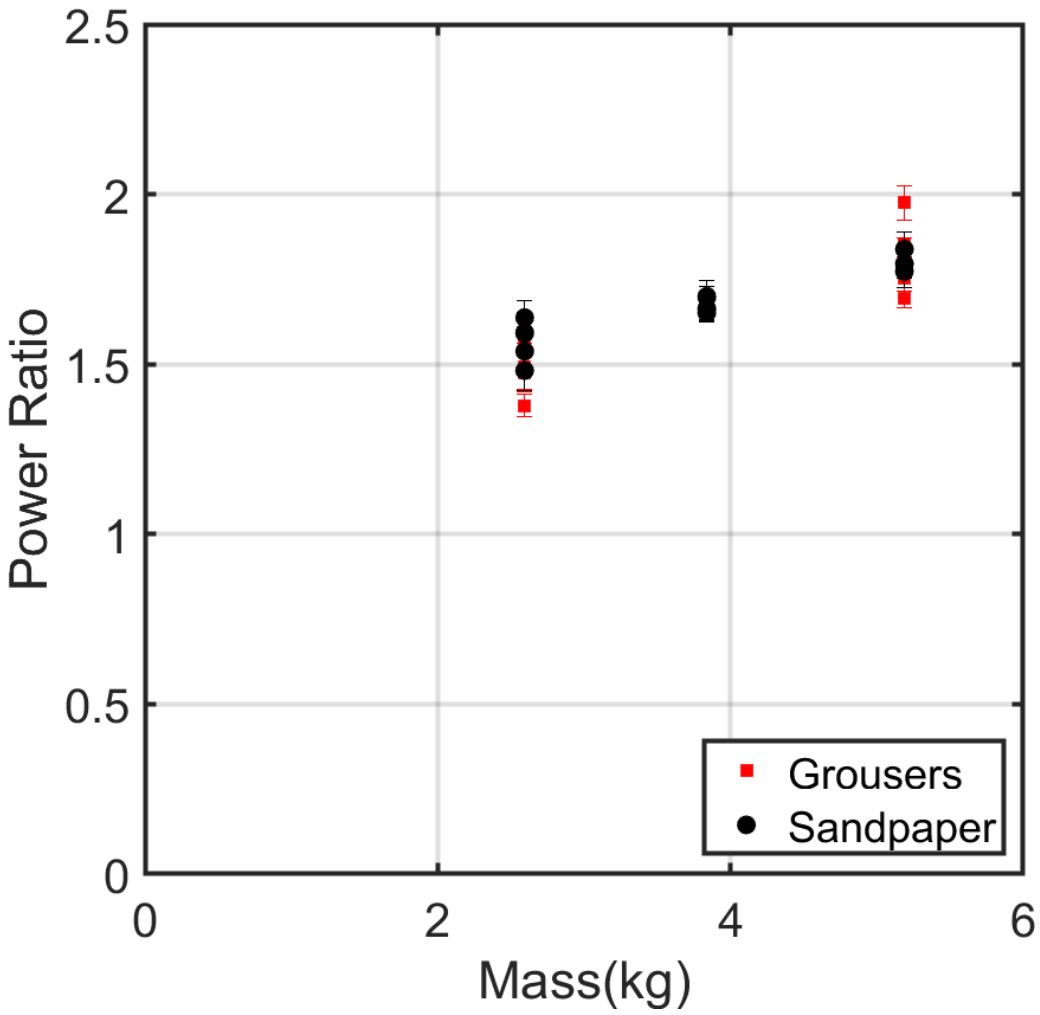

Figure 38. The relationship between mass and power ratio (large set mechanical power over smaller set mechanical power) for both types of wheels.

The study was designed to evaluate whether the scaling laws could apply to a lightweight robot and what deviations might be found. A light, medium, and heavy

set of masses for grousered wheels and a light and heavy set of masses for sandpaper wheels were run (see 4 for details). With these masses and the two wheel sizes, the target power ratio for all sets was 2.05 by design, i.e. all larger craft results should require double the mechanical power of their smaller counterparts. Each one of these was evaluated at five speeds. The full details are listed in 4, and the larger craft mass was used for comparison in both 38 and 39.

In the study by Slonaker *et al*, the original tests were run with masses between 13.4 kg and 45.7 kg for all sets [134]. In those tests, all sets reportedly followed their scaling predictions within an error of 3%. Those experiments were run with a single wheel on a gantry with the direction of travel constrained in a planar fashion. They were also run with all sets below 30 RPM. Here, the lowest mass is 1.46 kg and the largest is 5.19 kg. The total mechanical power comes from two wheels, and the craft is not constrained to move in a planar fashion although it generally did so as seen in the supplemental video. This mobility was allowed to evaluate more field-like conditions. The target speeds range from 15-75 RPM for smaller wheels and 13-65 RPM for larger ones. This different set of lighter, faster parameters was targeted to explore a design space closer to that of laboratory robots and small prototypes rather than fully sized vehicles.

The target power ratio of 2.05 was not reached for any of the experiments (38). Instead, a mass-dependency was noted in the power ratio and error percentage rather than a consistent ratio of 2.05 as predicted. The raw values for all 25 combinations of masses-speeds are shown in table 5 with both power ratio and error listed with “L”, “M“, “H” representing the light, medium, and heavy masses respectively. Interestingly, the closest case to target value was the heaviest sandpaper wheel set at the lowest speed; this particular condition was the closest to the experiments performed [134].

Table 5. Power Ratios and Errors For Mass-Dependant Predictions.

RPM	**GSL12SPL**	**Error**	**GSL12SPM**	**Error**	**GSL12SPH**	**Error**
13	1.59	22.6%	-	-	1.98	3.6%
26	1.47	28.1%	-	-	1.85	9.6%
39	1.38	32.8%	-	-	1.83	10.9%
52	1.55	24.2%	-	-	1.75	14.5%
65	1.49	27.3%	-	-	1.69	17.3%
RPM	**GSL12GL**	**Error**	**GSL12GM**	**Error**	**GSL12GH**	**Error**
13	1.48	27.7%	1.70	17.2%	N/A*	N/A*
26	1.64	20.1%	1.66	19.0%	1.84	10.3%
39	1.59	22.4%	1.70	17.1%	1.80	12.4%
52	1.54	25.0%	1.65	19.5%	1.77	13.5%
65	1.59	22.3%	1.66	18.8%	N/A*	N/A*

An alternative expression of the power ratio data is shown in 39 as an error percentage versus mass. The error percentage is defined as the difference between the experimental power ratio and the target of 2.05, over 2.05. A linear regression approximated the heaviest mass would need to be at 8 kg to attenuate the error to zero.

On this note, we now give our hypothesis for why the error is high when the observed physics appear similar to the case reported in [134]. The first possibility is best explained in an analogy to aerodynamics. Many design principles for commercial aircraft are centered around Reynolds Number, a dimensionless number. These design principles work rather well for large, powerful commercial craft because the flow inconsistencies are trivial compared to the overall system. However, model aircraft can show deviation because interruptions to ideal conditions are non-trivial [161] compared to the overall forces and powers. In our study, any small robot will necessarily be perturbed by slight planar angling of the sand surface, stress concentrations within the grains, and the like. Indeed, higher power levels in both sizes of the heavy sets would explain why their ratios are closer to the hypothetical values. A second insight

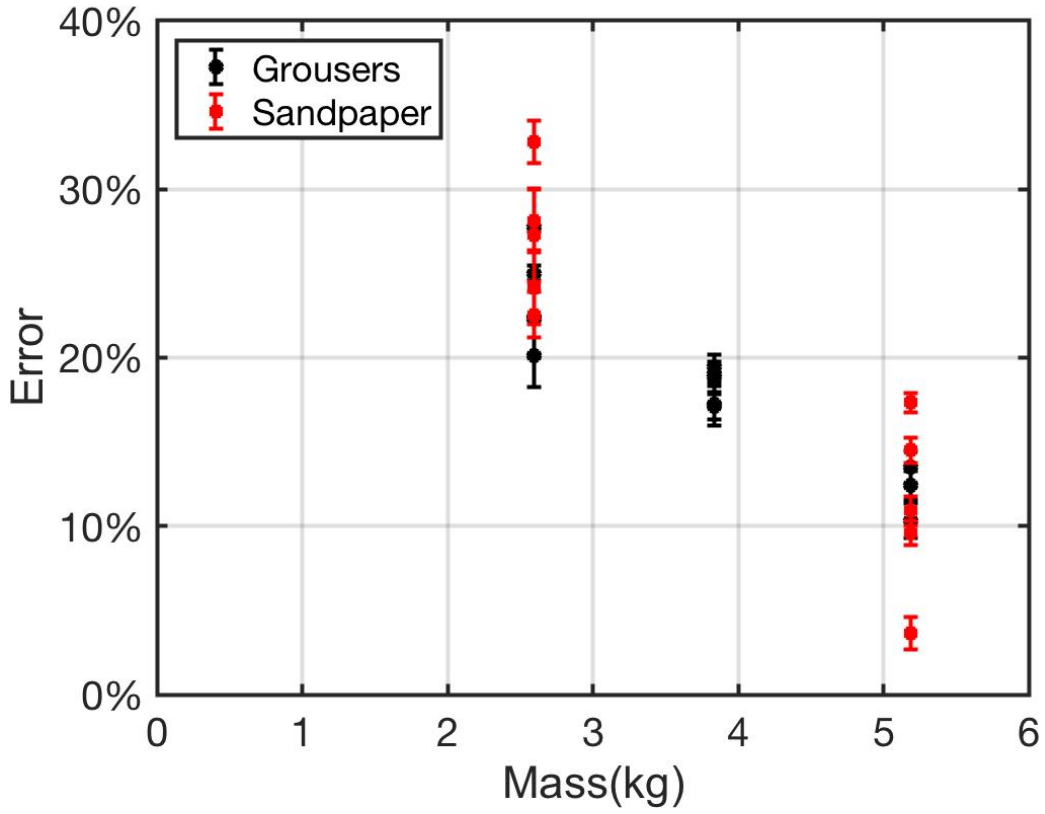

Figure 39. The error percentage as a function of mass. The error percentage is defined as the difference between the experimental power ratio and the target of 2.05, over 2.05.

was gained from preliminary Discrete Element Method (DEM) simulations into this experiment.

Wheels of identical sizes with different grousers were simulated, and the scaling laws were found to fall within 4% prediction at the same light masses which showed 30% error in experiments (40). The difference is that the Young's modulus of the grains was lowered and the grain size was increased in the simulation to decrease the computational cost without significantly sacrificing the macro scale interactions [149, 162, 163]. This may have allowed for an adequate amount of sinkage due

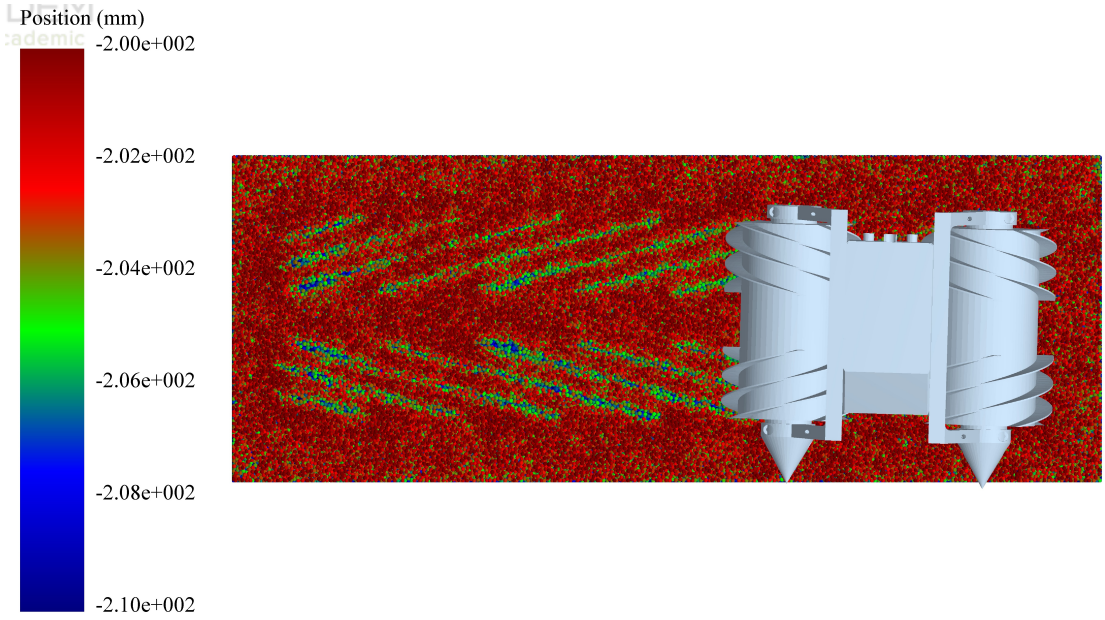

Figure 40. Simulation of a grousered rover traversing simulated granular media at 45 RPM. Cooler colors indicate deeper impressions with 1 cm difference between red and blue.

to compressibility of particles. Sinkage of this depth was not observed during our experiments; the craft was operating in a much shallower region.

It is also possible that the function is one of pressure; that is, there is a critical pressure in any particular soil that is required before the scaling laws are in a low error band or valid. The exploration of this pressure criticality is left as a future exercise since multiple sinkage-pressure models would likely need to be tested and evaluated [164].

The final observation on mass-error dependency is the difference observed between leading and lagging motors in the grousered wheels as seen in 41. If the two wheels are treated independently and the power ratios of the leading/lagging wheels are evaluated, some additional salient trends emerge. Notably, although the sandpaper wheels did not show high differentiation in error between leading and lagging wheels,

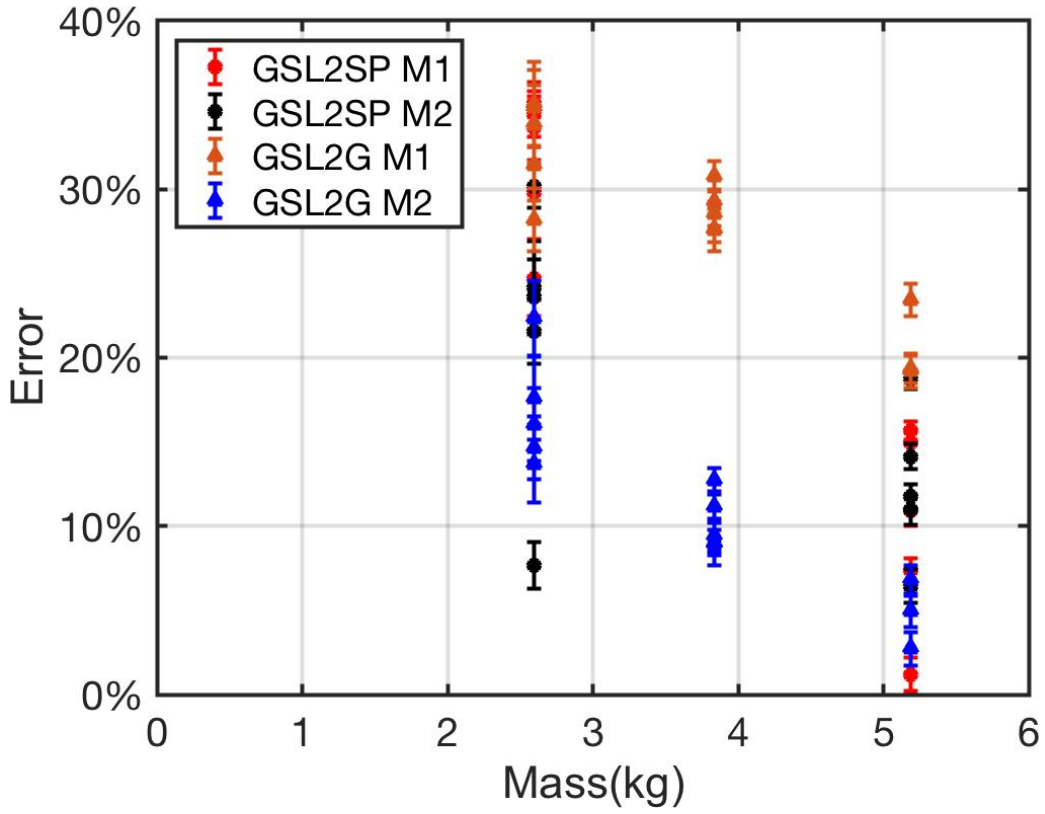

Figure 41. Error of each motor for grousered wheels; the front motors have significantly more error than rear motors.

the grousered wheels showed significant difference with the rear wheels drawing higher power ratio and lower errors in all Fcases. Our hypothesis is that since robot dynamics shifts weight towards the back, the grouser clearing effect was more pronounced on the front wheel. This would lower the power draw more significantly than the back wheel, which would likely see more sinkage and less advantage from the grousered shape.

6.4.2 Velocity/Inertia Dependence of Wheeled Granular Scaling Laws

We turn now to the velocity dependence of the power ratios. In figure 42, power ratios are graphed versus wheel rotational speed. For all sets, there is a weak function of power ratio versus speed with slope of -0.0014 power ratio/RPM. The power ratio decreases minimally with increased velocity for the experiments in general.

In addition, the heaviest sets show the highest dependence on velocity; linear regression shows almost double and quadruple the slopes compared to the group as a whole for grousered wheels with slope of -0.026 and sandpaper wheels with slope of -0.0052, respectively. For context, the original scaling law experiments presented in [134] had speeds between 14-28.6 RPM and no relationship between power ratio and velocity at different masses was observed. This is a limitation that one must bear in mind for using these laws to approximate robot power draw at higher speeds for light-weight rovers. It is possible that this scaling error as a function of wheel rotation velocity is reduced or disappears at higher masses.

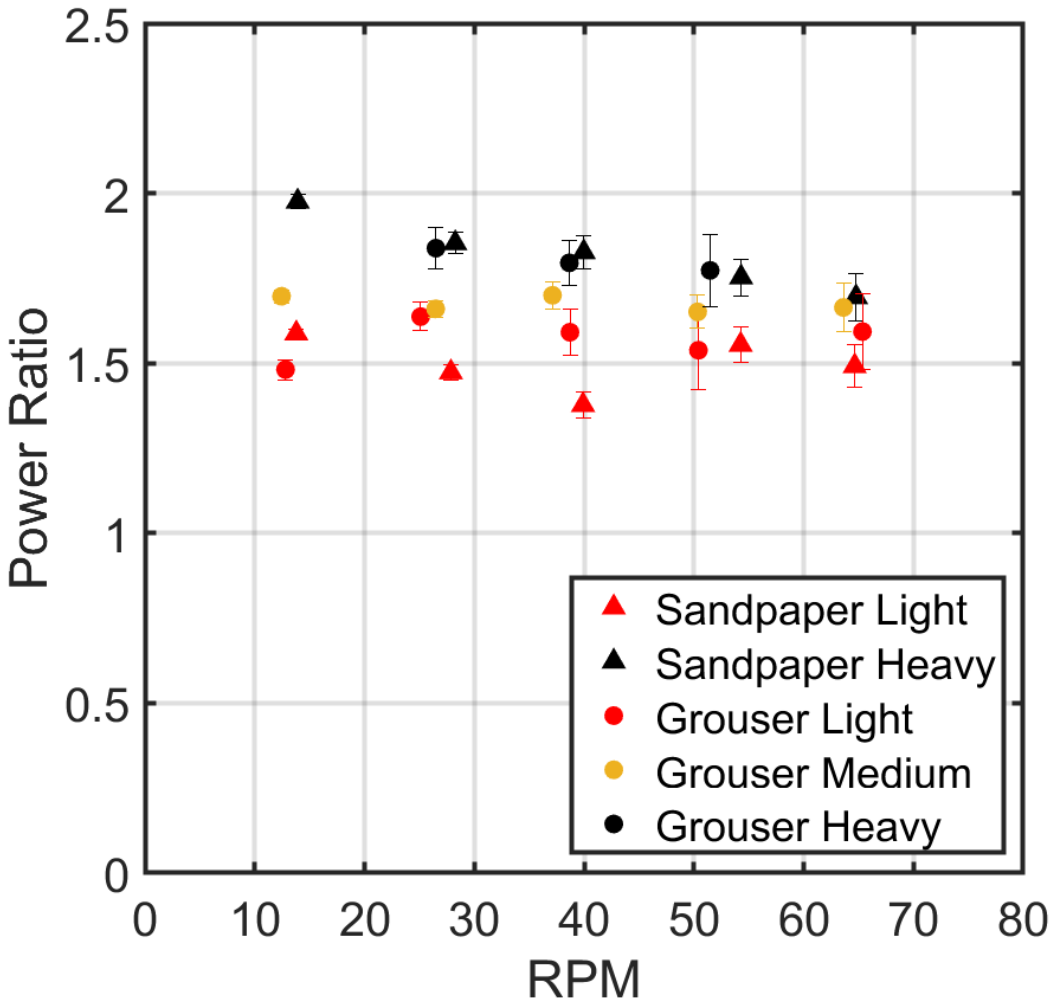

Figure 42. Power ratio versus wheel RPM. Power ratio trend of all data points shows a decrease with wheel rotational speed. Furthermore, power ratios of heaviest data points show significantly more decline with speed than lighter sets.

Chapter 7

HELICAL GRANULAR SCALING THEORY

7.1 Abstract

Motivated by the desire to explore screw propulsion for space applications, we have derived a new set of scaling laws for granular locomotion driven by screw shapes using non-dimensional analysis (NDA). These helical granular scaling laws (HGSL) compliment the already existing wheeled granular scaling laws. We evaluate a set of three screws with increasing size and mass based upon HGSL. The power and velocity characteristics of these sets are analyzed and the predictability of HGSL is evaluated. Surprisingly, we show through theory, experiment, and simulation that the complex granular reaction to three-dimensional screw-driven mobility results in similar power and velocity scaling predictions to those produced by wheeled scaling laws, provided the helix is radially continuous. These laws are verified for earth gravity experimentally in a lunar soil analogue as well as in reduced gravity through multi-body dynamic and discrete element method (MBD-DEM) co-simulations. Experimental results show a power prediction error of less than 10%. The respective velocity for these sets show less than 12% error. MBD-DEM simulation results match theoretical predictions closely with power error of 2-5% when depth is steady and velocity error of 2-3%. The result is a set of experiments and simulations which advance the ability to design and test helical-soil interactions and contribute to the understanding of granular physics scaling.

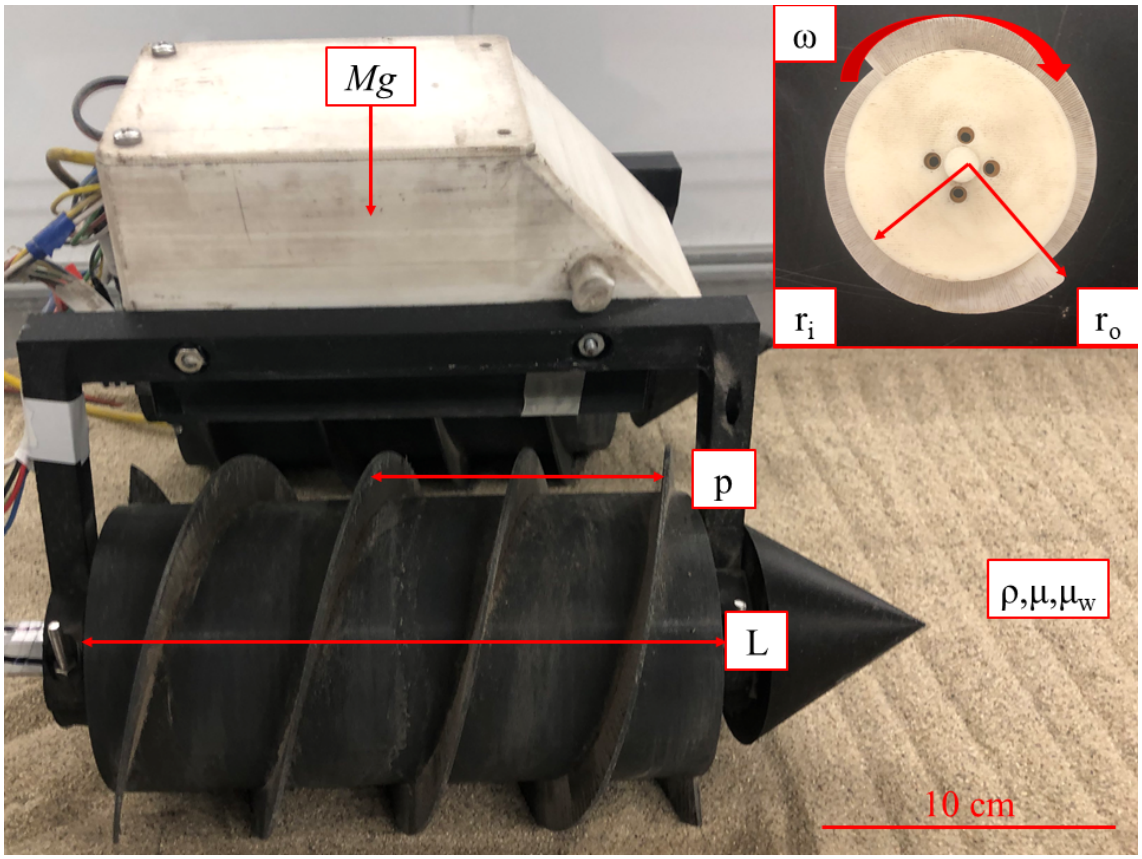

Figure 43. Side view of the craft and top and side views of the screw.

HGSL starts with an examination of the derivations of GSL to search for applicability to varied geometry. One of the fundamental assumptions about the wheeled scaling laws is the depth-invariance of the wheel shape; that is, the geometry is consistent through the entire thickness of the wheel. In this sense, the problem is almost reduced to two-dimensional. However, to expand the applicability for further mobility scenarios and explore the potential avenues of NDA for other geometries in space, we examined scaling laws for 3-dimensional helical geometries. We explicitly limit the helicoid shape of the screw pontoon and craft to certain assumptions. We

assume that the screw is radially continuous in general; that is, a slice of the geometry should be identical to any other portion but for a rotational offset. The screw pontoon radii are therefore consistent throughout the geometry; i.e. the pontoon itself does not taper and the blade radii do not vary. We also assume a straight translational heading of the craft with screw pontoons symmetrical about the midline of the craft and center of mass.

A geometry held to the relationships which classically describe a helical screw, along with the above assumptions, moving through a non or weakly cohesive granular media expressed as a frictional continuum, with trivial vehicle drag or inertial motion of the grains, can define its power and translational velocity based on a function of these variables:

$$[P, V] = f(p, r_i, r_o, l, m, \omega, \rho, \mu, \mu_s, g, t) \tag{7.1}$$

The screw geometry is described by the characteristic pitch p, its inner radius r_i, its outer radius r_o, and its length l. The system is described by its total mass m and a driving rotational velocity ω with the axis of rotation parallel to the direction of travel. The environment is described by gravity g and the granular characteristics ρ, μ, and μ_s; these are density, internal friction, and screw-grain friction, respectively. They are constant and occur as a function of the granular environment and its interaction with the geometry. Time t is the last driving parameter. Our target outputs are power P and translational velocity V. To non-dimensionalize this function, we select three of the variables to express the dimensions of all other variables.

$$L = p \qquad M = m \qquad T = \frac{1}{\omega} = \sqrt{\frac{p}{g}} \tag{7.2}$$

Explicitly, this means that the dimension of length is expressed by the pitch, dimension of mass by the mass, and dimension of time by the inverse of rotational velocity, as well as a relationship of pitch and gravity (this functionality will become apparent later). We produce non-dimensionalized versions of all of the other variables using these parameters as in this example for velocity:

$$\bar{V} = V * \frac{T}{L} = \frac{V}{\sqrt{pg}} \tag{7.3}$$

The variables which define the dimensions, i.e. p, l, and w, are not included since their non-dimensionalized form is 1. The friction coefficients are also already dimensionless, and hence need no transformation. We perform the above transformation on other variables and end up with the following set of non-dimensionalized variables:

$$[\frac{P}{mg\sqrt{pg}}, \frac{V}{\sqrt{pg}}] = (\frac{r_i}{p}, \frac{r_o}{p}, \frac{l}{p}, \frac{\rho p^3}{m}, \mu, \mu_s, \frac{g}{p\omega^2}, t\sqrt{\frac{g}{p}}) \tag{7.4}$$

To narrow the scope of these laws and simplify them, we make several assumptions:

1. We assume granular motion in the radial direction is trivial. In wheeled GSL, we see a similar idea. As a wheel travels over and through granular media, we assume the inertial energy transfer is low and grains are not mobilized quickly. The same assumption occurs here.
2. We assume that the pontoon geometry is radially consistent in shape along its length. In a sufficiently large environment with no wall effects, this implies that if all other dimensions are held but mass m and length l of the pontoon are both scaled by some constant n, then the output power would be similarly scaled by n to nP. This is because vehicle power requirements are largely driven by the granular interaction caused by sinkage, which is dependant on the screw surface pressure in granular media. For example, doubling the mass of a craft would

double the weight, but doubling the length of the pontoons also distributes that weight across twice the surface area, resulting in similar granular pressure and sinkage. This implies a similar sinkage envelope, performance envelope, and the increase in power is then predictably double. Here we make an important insight: pontoon length l and mass m are not independent. The ratio of l and m ought to remain consistent between two scaled designs. Thus, we reduce two non-dimensionalized variables into one by their product and constrain the pontoon length by the mass scalar as well as the pitch scalar.

3. We assume that granular environment is consistent between experiments with different pontoons. The dimensionless friction coefficient of grain-screw interaction, the internal friction of the granular media, and the expression for density are assumed consistent; therefore we eliminate friction and density from our equations.
4. We assume constant gravity and remove it from our expression. This will become important later as we explore MBD-DEM simulations of a gravity-variant nature.

Thus, the final NDA function is as follows:

$$[\frac{P}{m\sqrt{p}}, \frac{V}{\sqrt{p}}] = (\frac{r_i}{p}, \frac{r_o}{p}, \frac{lp^2}{m}, \frac{1}{p\omega^2}, t\sqrt{\frac{1}{p}}) \tag{7.5}$$

The result of this exercise is a set of laws which look remarkably similar to the original wheeled granular scaling theory but for a screw in which the axis of rotation is parallel to the direction of travel. In fact, if one folds the pitch, inner radius, and outer radius into a single variable, the equations take on the same form. Given the above assumptions and two experiments, one with the inputs of $(p, m, r_i, r_o, l, \omega)$ and the other scaled by positive scalars a, b with inputs $(p', m', r_i', r_o', l', \omega') = (ap, bM, ar_i, ar_o, ba^{-2}l, a^{-1/2}\omega)$, the time averaged powers and

translational velocities should follow $P' = ba^{1/2}P$ and $V' = a^{1/2}V$. Simply put, if we scale all screw dimensions (except for l) in size by scalar a and mass by scalar b with the above parametric changes, we ought to be able to predict the mechanical power and velocity of one screw propelled vehicle from another.

7.3 Methods to Evaluate HGSL Performance

7.3.1 Development of Screw Propelled Craft and Screw Designs

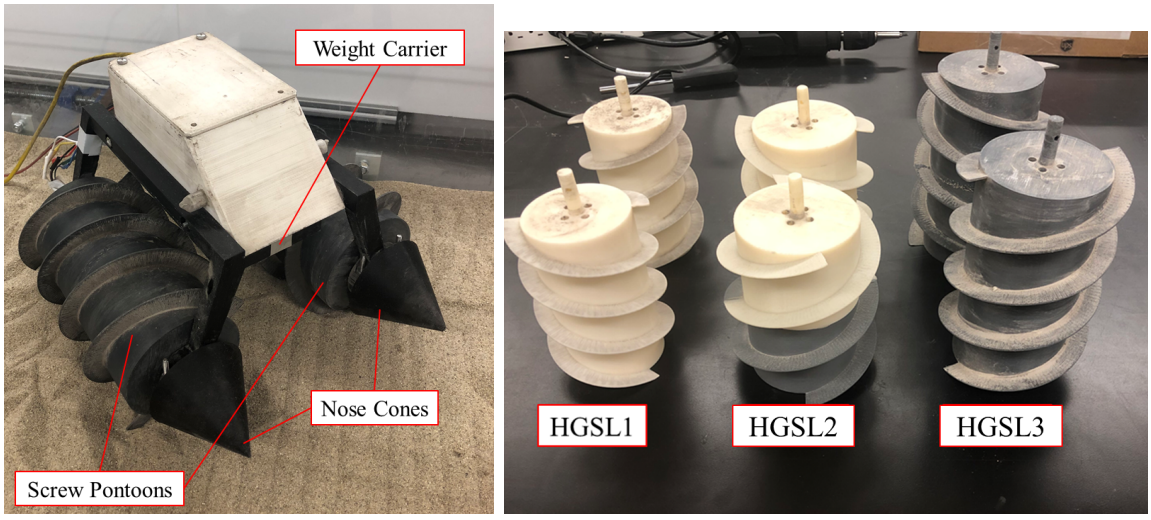

Figure 44. (a) Craft with items labeled and (b) screw sets.

The platform in these tests consists of a central body with electronics located internally, a weight carrier to modify total craft mass, screw pontoons designed in accordance with HGSL parameters, and nose cones to reduce significance of any occurring front drag. Care was taken to avoid body drag as much as possible and to avoid wall boundary effects. The inertia of the pontoons for scaling experiments is a non-trivial concern and care was taken to scale the inertia of the pontoons

appropriately. Design of the helix angle included insights from helical optimization studies [135, 136] that listed 55°, although each paper's helix angles have complimentary definitions. Pitch was equated to the inner diameter value for each set, leading to a close approximation of the above target at 53°. The screw sizes and craft masses were based upon preliminary experiments which indicated the range of output power for our motors could be roughly doubled from the HGSL1 sizing. Therefore, HGSL2 was designed for approximately 50% increase in power and HGSL3 designed for approximately double required power. The chosen parameters for the experiments are listed in table 6 with mass in kilograms and length dimensions in centimeters.

Table 6. Parameters Chosen for Helical Pontoons

Design	**Pitch**	**Mass**	**Length**	r_i	r_o	**Target ω (RPM)**
HGSL-1	7.5	1.441	14	3.75	5	15.0,30.0,45.0,60.0,75.0
HGSL-2	9.0	2.075	14	4.5	6	13.7,27.4,41.0,54.8,68.5
HGSL-3	9.0	2.666	18	4.5	6	13.7,27.4,41.0,54.8,68.5

7.3.2 Experimental Environment and Procedure

Earth testing of Mars Curiosity Rover traversability shows the variability in performance and interactions with different types of granular environments [27]. This variability indicates that evaluation of generalized laws in a material close to target environment is valuable. BP-1 is used as the granular environment for this set of experiments.

Experiments were performed in the simulant containment unit seen in figure 45. The BP-1 was tilled by a thatch rake to prevent large soil stresses. The craft was placed on top of the BP-1 at one end of the chamber. Each trial ran from one end of

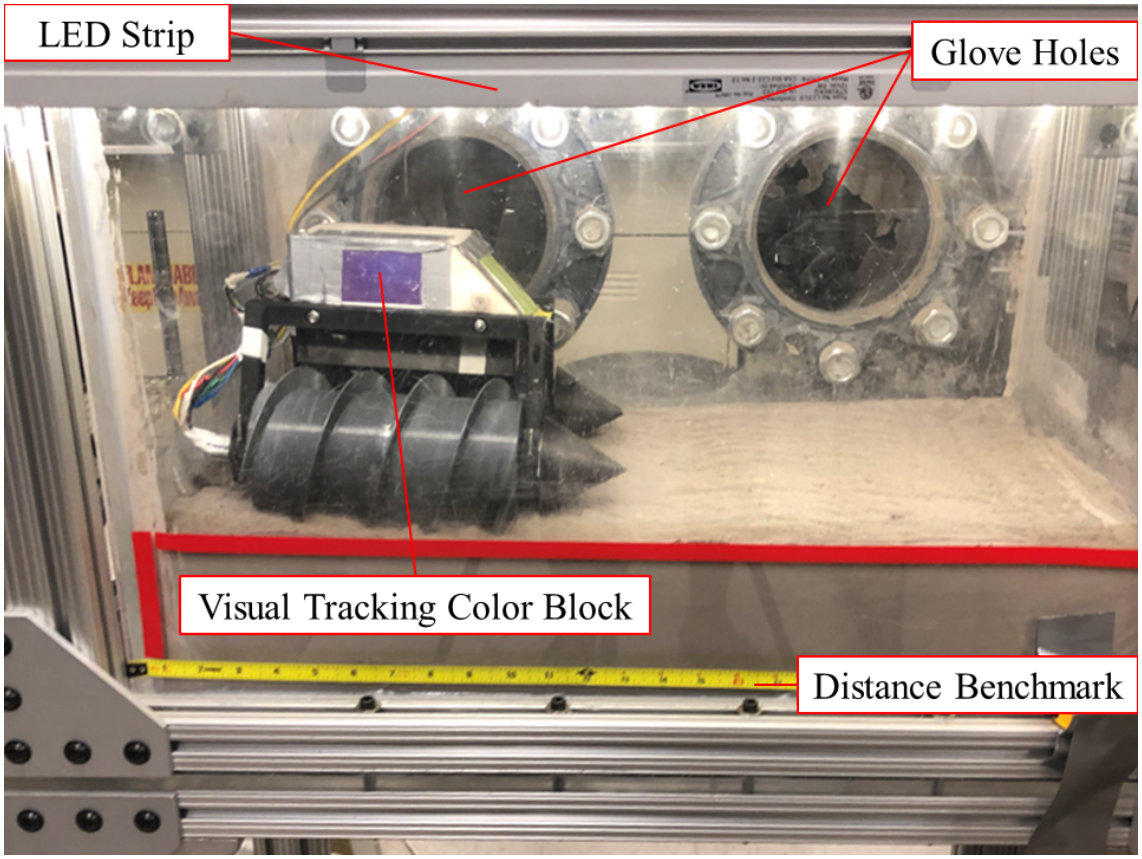

Figure 45. BP-1 testing chamber with craft inside and components labelled

the chamber to the other. The simulant containment unit is equipped with a LED light strip so that the moving craft was clearly visible in the video as dusty conditions occur. Camera location and settings were kept consistent between all trials. A blocks of color attached to the side of the craft was used to track velocity. Lighting was kept consistent in order to keep tracking as accurate as possible. The trial was recorded by both Arduino for power and video camera for velocity. Utilizing a MATLAB based color tracking program, position versus time was determined and analyzed for each video. Mechanical power was evaluated using in-line hall-effect current sensors, located immediately before the motor, to obtain individual current readings. The current was converted to torque by the given motor constant, and the time-averaged torque and

rotational speed were multiplied during steady state bands to produce time-averaged power. A total of ten trials were performed for each set of speeds, five speeds were chosen for each screw, and a total of three different screws were run in the BP-1.

We briefly add experimental craft assumptions to the earlier assumptions about the helical geometry. We assumed no interaction between the helical screws and maintained a physical separation distance appropriate to achieve this. A related assumption was using a straight path; any turning was not sufficient to create interactions between one screw's impression on the environment and the other screw.

7.4 Results and Discussion

7.4.1 Power and Velocity Prediction, Error, and Functional Relationships to Rotational Speed

Trials were run as close to target RPM as possible for HGSL1, HHGSL2, and HGSL3. The five rotational velocities of HGSL1 dictated the exact targets for HGSL2 and HGSL3, and the power at those velocities was then estimated based on a linear regression through the HGSL2 and HGSL3 points. The results of the comparison between predicted mechanical power and actual mechanical power indicate that the laws provide a reasonable estimate in BP-1. The error of HGSL2 ranged from 4% to -3%; the slower speeds were slightly underpredicted and higher speeds overpredicted. HGSL3 showed the opposite trend; it had power prediction error ranging from -4% to 9% weakly driven by velocity. It is noted here that a small portion of power is due to the body drag generated by the nose cones, and HGSL3 as the heavier set may have added power draw due to slightly greater depth and hence, body drag. It is worth

noting that the error of both sets is significantly less than that of recent experiments involving wheels of similar mass [165]. One potential explanation for the lower error is that while the factors which drive granular compaction resistance are complex, there may be some level of sinkage-driven functionality which creates an effect on the laws' accuracy.

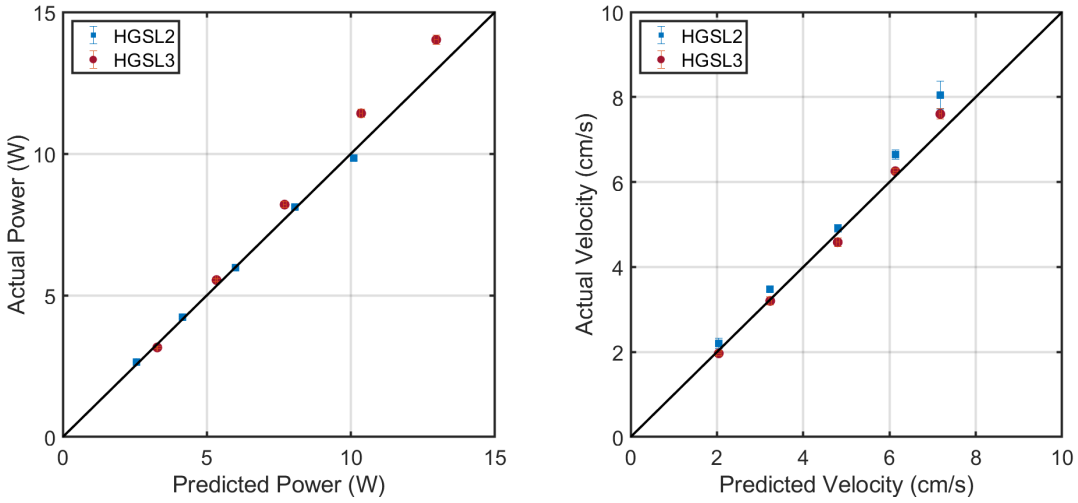

Figure 46. Experimental results paired with their respective predictions.

The results of the comparison between predicted velocity and actual velocity indicate the laws provide a reasonable velocity estimate in BP-1 as well (figure 46). HGSL2 error ranged from 2-12% without noticeable velocity dependence and with all values above predicted. HGSL3 error ranged from 1-6% error with slower values lower than predicted and faster values higher than predicted. One observation made during experiments was the existence of small (but non-trivial) granular accumulation in front of all three sets. It is possible that the HGSL3 set, with higher mass, required additional power to move this material. This would explain its general trends of power overprediction and velocity underprediction.

7.4.2 MBD-DEM Simulations for Gravity-Variant HGSL

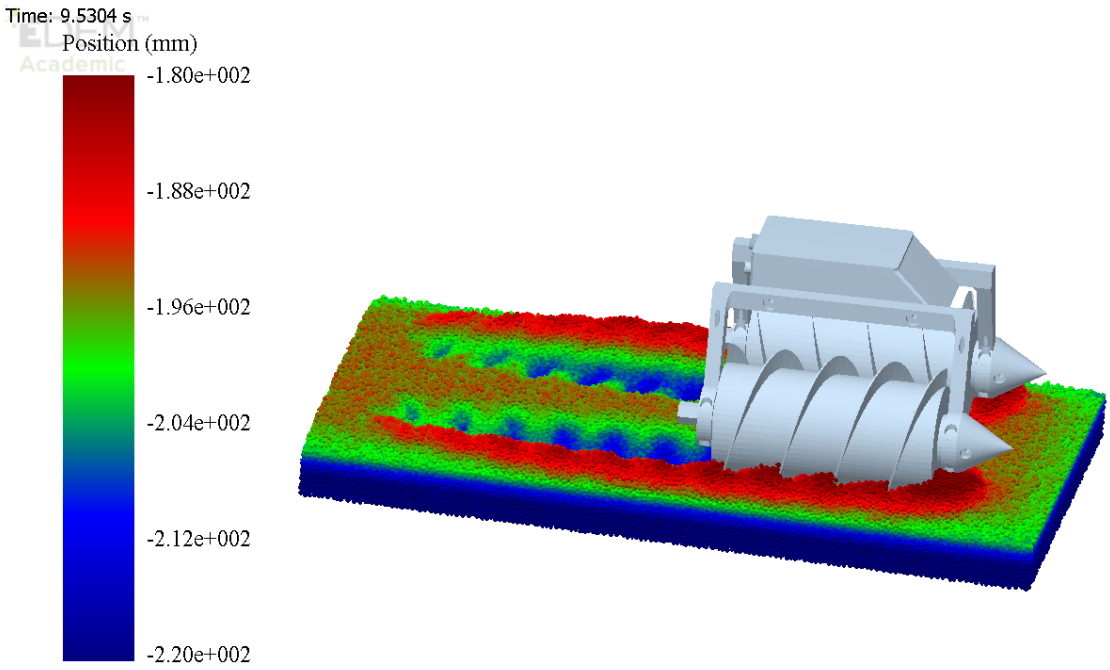

Figure 47. Isometric view of screw pontoon mobility in lunar gravity.

Recall the gravity-variant scaling laws in equation 7.4. Given the same assumptions as before, we now examine two simulation sets: one with the inputs of $(p, m, r_i, r_o, l, \omega, g)$ and the other changed by positive scalars a, b, c with inputs $(p', m', r_i', r_o', l', \omega', g') = (ap, bM, ar_i, ar_o, ba^{-2}l, a^{-1/2}c^{1/2}\omega, cg)$. The time-averaged powers and translational velocities should then follow $P' = a^{1/2}bc^{3/2}P$ and $V' = a^{1/2}c^{1/2}V$. If we scale all screw dimensions (except for l) in size by scalar a, mass by scalar b, and gravity by scalar c with the above parametric changes, we ought to be able to predict the mechanical power and velocity of one screw propelled vehicle from another in a different gravity.

All simulation parameters were driven by the literature or experimental testing. Rolling friction of BP-1 on ABS and static friction of BP-1 on ABS was determined experimentally by spraying spheres and a plate with adhesive, dusting with BP-1, and running trial experiments. Bulk density measurements of BP-1 were taken; unconsolidated (experimental conditions) were found to be 1.561 $\frac{g}{cm^3}$ while consolidated were 1.633 $\frac{g}{cm^3}$. Both of these are well within the range previously noted [43]. Notably, Young's modulus was reduced and particle size increased to make simulations computationally feasible. Table 1 in Chapter 2 lists the simulation parameters used.

Briefly, we touch upon an experimental and simulation HGSL1 set comparison, since these are both at Earth gravity and can be directly compared. We find a non-trivial difference for power between the two sets; the simulation power is $\approx 70\%$ that of experimental for each speed. This is largely due to the reduced stiffness of the particles and increase in particle size; while care was taken to create a realistic bulk density, there are still granular phenomenon which cannot be replicated by spherical agglomerate models. The difference in velocity was $\approx 20\%$. While this signifies deviation of bulk properties from experiments, it also is an opportunity to evaluate HGSL laws in what could be considered a second material.

Time, power, and velocity were non-dimensionalized and the average power and velocity were taken from the same dimensionless time range for both the Earth and lunar simulations. Figure 48 illustrates an error of 1-5% for most power scaled predictions in steady depth and 2-3% for velocity scaled predictions in lunar gravity from Earth gravity results. Notably, the 11 RPM trial for HGSL2 simulations shows 13% power error. In examining the results, the 11 RPM trial is found not to reach a steady depth by the end of the simulation. These results, similar in error range to experimental, are better than previous MBD-DEM simulations run with wheeled craft

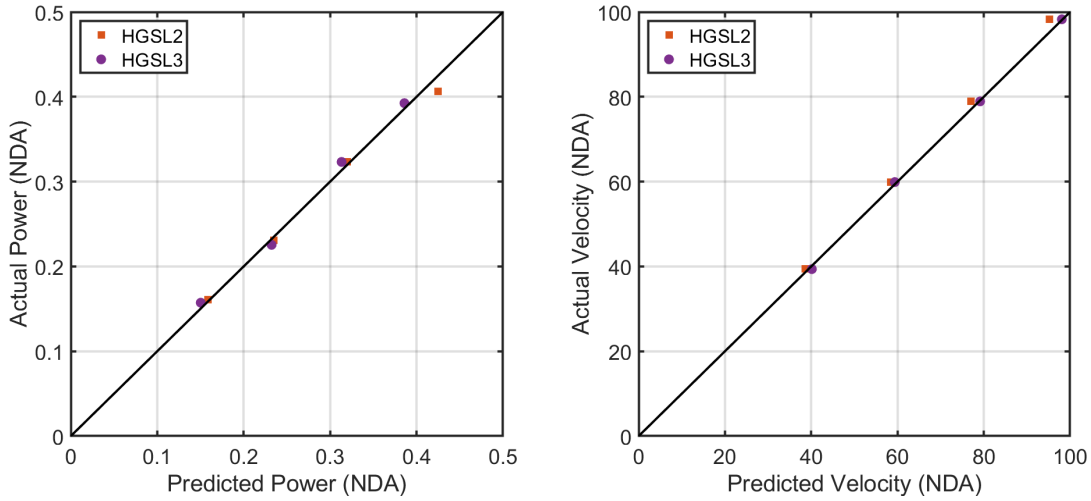

Figure 48. Simulation results for HGSL2 and HGSL3 compared to their NDA counterparts from HGSL1

at the same mass [165]. This is attributed to the same explanation as experiments: deeper geometry engagement with grains and lower translational speed compared to our previous wheeled studies. Overall, HGSL prediction of both velocity and power find good agreement with simulation results, and better agreement than wheeled scaling laws for rovers of similar mass. HGSL closely predicts the time-averaged power and velocity of screw propelled vehicles in Earth gravity experimentally and lunar gravity by simulation.

Chapter 8

CONCLUSION AND FUTURE WORK

8.1 Conclusions

This thesis has presented several approaches for predicting responses of helical geometry in granular media. The primary driving goal of chapter 3 is the evaluation of DEM capabilities for accurately predicting forces generated by double-wound helices using a glass beads. DEM proved valuable for helices, given that they violate leading edge geometry conditions assumed in RFT. The work shows that it is possible to make reasonably accurate predictions about helix force generation with DEM at lower Young's modulus values but a rotating helix in granular media may not be well analyzed using RFT. Chapter 4 examined dynamic screw designs with MBD-DEM co-simulation using adjustments to the Young's modulus. Addressing the differences in simulations and experiments led to the conclusion that MBD-DEM is suited for evaluating dynamic motion generated by double-wound helices in well-characterized granular media and showed that non-dimensional gravity-variance predictions in Earth, Moon, and Ceres simulated gravity obey the developed scaling laws under conditions of consistent slip. Chapter 5 indicated a potentially important envelope of feasibility for using GSL. MBD-DEM simulations of wheeled GSL in lunar gravity show a promising avenue of evaluating gravity-variant rover predictions, given that the simulated environment had lunar analogue characteristics. However, experiments with a lightweight, two-wheeled, unrestrained craft show significant deviation from power predictions. It highlights important edge cases for GSL and the need to find a

minimum wheel engagement criteria for individual soil/pressure combinations or wheel designs. BP-1 predictions are only marginally worse than Quikrete, bihelix wheel performance is similar to straight grousers, and overall error is explained by craft dynamics and a mass, pressure, slip or sinkage dependency in Chapter 6. The accuracy of predicting mechanical power draw using granular scaling laws for lightweight rovers is evaluated, with results indicating inconsistency with the laws at the masses (1.5-5.2 kg) and speeds (13-75 RPM) tested. Importantly, the heaviest and slowest sandpaper case showed error within reported literature accuracy and the results of this inaccuracy can be seen as a strong function of the mass, likely due to lightweight rovers creating subcritical amounts of sinkage to fully engage the soil at a level which is necessary for scaling to be accurate. The results can also be seen as a weak function of rotational wheel speed, likely due to inertial effects. Furthermore, when analyzing individual motors, there is lower error for lagging wheels than leading wheels in the grousered sets, likely because of vehicle dynamics and more effective lead wheel grouser clearing. Finally, in Chapter 7 three SPV's of different size and mass were designed and tested according to this dissertation's newly derived helical granular scaling laws in experiments and simulations. Good general agreement is seen in both power and velocity prediction for experiments in BP-1. Explicitly, and importantly, this points to BP-1 as a granular material which will obey a GSL under critical engagement conditions. In MBD-DEM simulations, good agreement is seen with both power and velocity to predictions, validating HGSL for a range of gravity between Earth and lunar.

8.2 Future Work

Future research could include developments in MBD-DEM, granular scaling theory, or expansion of rover designs. For MBD-DEM simulations, it would be valuable to characterize what influence Young's modulus reduction has on both static and dynamic movement characteristics such as drag force, power, and peak velocity. It would also be valuable to refine the DEM characteristics of regolith simulants such as BP-1. Greater agreement between direct experiment and simulation comparisons for these materials would aid development of craft and tools meant to operate in these environments. Granular environment choice is another path. Using a ubiquitous material such as Mars Mojave Simulant, a Martian regolith simulant, would be valuable as a future testing media. Investigations of wheel shape, particularly grouser shape, using MBD-DEM analysis would be useful to find optimal grousers for a particular soil.

For expansion on general granular scaling theory, parameters of interest, such as non-dimensionalized drawbar pull, are a potential avenue; it would be beneficial to understand towing force using this approach. All of these ought to be done with simple benchmark tests regarding the mass and size of the craft first to determine GSL applicability at those target levels. Interactions also occurred with grousered wheels to create unequal loading in motors; although the separation distance between wheels was not characterized this is a potential design space to explore as well. Determining the envelope or criteria of accuracy for GSL due to geometry engagement is an important question to answer. As the vehicle becomes closer to a magnitude of weight and size seen by full-sized rovers, there may be other mass-dependant effects which have not been uncovered yet. A study ranging across 2.6 kg (the smallest

mass used in chapter 6) to 29.3 kg (the smallest mass used by Slonaker *et al* in their larger wheel sizes) in a well characterized sand could fully evaluate the relationship between mass (or pressure/sinkage) and scaling error. Direct measurement of sinkage or pressure in this case would provide the most straightforward answer. Exploring the max loading envelope of screws before the craft is immobilized, and studying a minimum envelop of engagement (such that the pontoons do not merely fluidize granules rather than mobilize the craft) are also possible paths. Varying mass in an MBD-DEM simulation to evaluate the scaling laws could provide valuable insights, as could extending the range of gravity variance. Exploring these scaling principles in a wider variety of environments could similarly provide valuable insights. Body drag force in granular media has been shown to scale cubically with characteristic length of the object and a similar theoretical conclusion for colloidal matter such as gels has been shown[133], providing an opportunity to explore continuum based predictions in muds on Earth. One could also reconcile the body drag laws with GSL to create numerical simulations or analytical predictions of complex vehicle engagement which includes both locomotor and body of vehicle. Non-homogenized environments including obstacles such as boulders are another option.

A possible direction of rover development from the work in this dissertation is a fusion of traditional wheeled mobility with screw propulsion for multi-modal craft mobility. In chapter 5, the empirical performance of the heaviest sets, GSL3G and GSL3B, were shown in figure 29 and figure 32 to be very similar for both power and velocity. If a craft were operating with four independent helically grousered wheels, it would be capable of achieving screw propulsion with the right configuration of rotations. This mode of travel would confer an advantage in escaping high sinkage media for higher gravity bodies such as the Moon and potentially be a primary

mode of exploration for lower gravity bodies such as Enceladus or large asteroids. Both mobility modes could then be evaluated using GSL, HGSL, and MBD-DEM approaches to achieve an optimal craft design for such an application.

REFERENCES

[1] MJ Neumeyer and BD Jones. "The marsh screw amphibian". In: *Journal of Terramechanics* 2.4 (1965), pp. 83–88.

[2] Liang Ju et al. "Experimental results of a novel amphibian solution for aquatic robot". In: *Robotics and Automation (ICRA), 2010 IEEE International Conference on*. IEEE. 2010, pp. 2261–2266.

[3] Ken Evans. "The history, challenges, and new developments in the management and use of bauxite residue". In: *Journal of Sustainable Metallurgy* 2.4 (2016), pp. 316–331.

[4] Vivake Asnani, Damon Delap, and Colin Creager. "The development of wheels for the Lunar Roving Vehicle". In: *Journal of Terramechanics* 46.3 (2009), pp. 89–103.

[5] Robert P Mueller et al. "Regolith advanced surface systems operations robot (rassor)". In: *Aerospace Conference, 2013 IEEE*. IEEE. 2013, pp. 1–12.

[6] J Veverka et al. "The landing of the NEAR-Shoemaker spacecraft on asteroid 433 Eros". In: *Nature* 413.6854 (2001), p. 390.

[7] Akira Fujiwara et al. "The rubble-pile asteroid Itokawa as observed by Hayabusa". In: *Science* 312.5778 (2006), pp. 1330–1334.

[8] Holger Sierks et al. "On the nucleus structure and activity of comet 67P/Churyumov-Gerasimenko". In: *Science* 347.6220 (2015), aaa1044.

[9] DS Lauretta et al. "The OSIRIS-REx target asteroid (101955) Bennu: Constraints on its physical, geological, and dynamical nature from astronomical observations". In: *Meteoritics & Planetary Science* 50.4 (2015), pp. 834–849.

[10] Yuichi Tsuda et al. "System design of the Hayabusa 2—Asteroid sample return mission to 1999 JU3". In: *Acta Astronautica* 91 (2013), pp. 356–362.

[11] LT Elkins-Tanton et al. "Journey to a metal world: concept for a discovery mission to Psyche". In: *Lunar and Planetary Science Conference*. Vol. 45. 2014, p. 1253.

[12] HF Levison et al. "Lucy: surveying the diversity of the Trojan asteroids, the fossils of planet formation". In: *Lunar and Planetary Science Conference*. Vol. 47. 2016, p. 2061.

[13] Hayato Omori et al. “Validation of the measuring condition for a planetary subsurface explorer robot that uses peristaltic crawling”. In: *Aerospace Conference, 2013 IEEE*. IEEE. 2013, pp. 1–9.

[14] Hayato Omori et al. “Development of a novel bio-inspired planetary subsurface explorer: Initial experimental study by prototype excavator with propulsion and excavation units”. In: *IEEE/ASME Transactions on Mechatronics* 18.2 (2013), pp. 459–470.

[15] Cornell Wright et al. “Design and architecture of the unified modular snake robot”. In: *Robotics and Automation (ICRA), 2012 IEEE International Conference on*. IEEE. 2012, pp. 4347–4354.

[16] Weikun Zhen, Chaohui Gong, and Howie Choset. “Modeling rolling gaits of a snake robot”. In: *Robotics and Automation (ICRA), 2015 IEEE International Conference on*. IEEE. 2015, pp. 3741–3746.

[17] Brian H Wilcox. “ATHLETE: A limbed vehicle for solar system exploration”. In: *Aerospace Conference, 2012 IEEE*. IEEE. 2012, pp. 1–9.

[18] A Scott Howe and Brian Wilcox. “Outpost assembly using the ATHLETE mobility system”. In: *Aerospace Conference, 2016 IEEE*. IEEE. 2016, pp. 1–9.

[19] Aaron Parness. “Anchoring foot mechanisms for sampling and mobility in microgravity”. In: *Robotics and Automation (ICRA), 2011 IEEE International Conference on*. IEEE. 2011, pp. 6596–6599.

[20] Donald Ruffatto, Aaron Parness, and Matthew Spenko. “Improving controllable adhesion on both rough and smooth surfaces with a hybrid electrostatic/gecko-like adhesive”. In: *Journal of The Royal Society Interface* 11.93 (2014), p. 20131089.

[21] Benjamin J Hockman et al. “Design, Control, and Experimentation of Internally-Actuated Rovers for the Exploration of Low-gravity Planetary Bodies”. In: *Journal of Field Robotics* 34.1 (2017), pp. 5–24.

[22] Robert G Reid et al. “Contact dynamics of internally-actuated platforms for the exploration of small solar system bodies”. In: *Proceedings of i-SAIRAS*. 2014.

[23] Daniel Mège et al. “The Highland Terrain Hopper (HOPTER): Concept and use cases of a new locomotion system for the exploration of low gravity Solar System bodies”. In: *Acta Astronautica* 121 (2016), pp. 200–220.

[24] Marco Pavone et al. “Spacecraft/rover hybrids for the exploration of small solar system bodies”. In: *IEEE Aerospace Conference*. 2013.

[25] Christian Krause et al. “MASCOT–a Mobile Lander on-board Hayabusa2 Spacecraft–Status and Operational Concept for the Asteroid Ryugu”. In: *2018 SpaceOps Conference*. 2018, p. 2418.

[26] Masataku Sutoh et al. “Traveling performance evaluation of planetary rovers on loose soil”. In: *Journal of Field Robotics* 29.4 (2012), pp. 648–662.

[27] Matt Heverly et al. “Traverse performance characterization for the Mars Science Laboratory rover”. In: *Journal of Field Robotics* 30.6 (2013), pp. 835–846.

[28] Feng Zhou et al. “Simulations of mars rover traverses”. In: *Journal of Field Robotics* 31.1 (2014), pp. 141–160.

[29] Issa AD Nesnas et al. “Axel and DuAxel rovers for the sustainable exploration of extreme terrains”. In: *Journal of Field Robotics* 29.4 (2012), pp. 663–685.

[30] Issa A Nesnas et al. “Moon Diver: A Discovery Mission Concept for Understanding the History of Secondary Crusts through the Exploration of a Lunar Mare Pit”. In: *2019 IEEE Aerospace Conference*. IEEE. 2019, pp. 1–23.

[31] Brian H Wilcox et al. “ATHLETE: A cargo handling and manipulation robot for the moon”. In: *Journal of Field Robotics* 24.5 (2007), pp. 421–434.

[32] Vytas SunSpiral et al. “Development and field testing of the footfall planning system for the ATHLETE robots”. In: *Journal of Field Robotics* 29.3 (2012), pp. 483–505.

[33] Takeshi Aoki, Yuki Murayama, and Shigeo Hirose. “Development of a transformable three-wheeled lunar rover: Tri-Star IV”. In: *Journal of Field Robotics* 31.1 (2014), pp. 206–223.

[34] Thomas M Roehr, Florian Cordes, and Frank Kirchner. “Reconfigurable integrated multirobot exploration system (rimres): heterogeneous modular reconfigurable robots for space exploration”. In: *Journal of Field Robotics* 31.1 (2014), pp. 3–34.

[35] Rover Team. “Characterization of the Martian surface deposits by the Mars Pathfinder rover, Sojourner”. In: *Science* 278.5344 (1997), pp. 1765–1768.

[36] Jitendra Nath Goswami and Mylswamy Annadurai. “Chandrayaan-2 mission”. In: *Lunar and Planetary Science Conference*. Vol. 42. 2011, p. 2042.

[37] Kazuya Yoshida, Nathan Britton, and John Walker. "Development and field testing of moonraker: a four-wheel rover in minimal design". In: *ICRA13 Planetary Rovers Workshop*. 2013.

[38] Jaakko T Karras et al. *Puffer: pop-up flat folding explorer robot*. US Patent App. 15/272,239. 2017.

[39] Jaakko T Karras et al. "Pop-up mars rover with textile-enhanced rigid-flex PCB body". In: *2017 IEEE International Conference on Robotics and Automation (ICRA)*. IEEE. 2017, pp. 5459–5466.

[40] Ahmad Najmuddin Ibrahim, Shinichi Aoshima, and Yasuhiro Fukuoka. "Development of wheeled rover for traversing steep slope of cohesionless sand with stuck recovery using assistive grousers". In: *2016 IEEE International Conference on Robotics and Biomimetics (ROBIO)*. IEEE. 2016, pp. 1570–1575.

[41] Hiroaki Inotsume et al. "Modeling, analysis, and control of an actively reconfigurable planetary rover for traversing slopes covered with loose soil". In: *Journal of Field Robotics* 30.6 (2013), pp. 875–896.

[42] Yasuyuki Yamada et al. "Development of a Blade-type Crawler Mechanism for a Fast Deployment Task to Observe Eruptions on Mt. Mihara". In: *Journal of Field Robotics* 33.3 (2016), pp. 371–390.

[43] Eduardo Suescun-Florez et al. "Geotechnical properties of BP-1 lunar regolith simulant". In: *Journal of Aerospace Engineering* 28.5 (2014), p. 04014124.

[44] Robert P Mueller. "Lunabotics mining competition: Inspiration through accomplishment". In: *Earth and Space 2012: Engineering, Science, Construction, and Operations in Challenging Environments*. American Society of Civil Engineers, 2012, pp. 1478–1497.

[45] Robert P Mueller and Paul J Van Susante. "A Review of Extra-Terrestrial Mining Robot Concepts". In: *Earth and Space 2012: Engineering, Science, Construction, and Operations in Challenging Environments*. American Society of Civil Engineers, 2012, pp. 295–314.

[46] Laila A Rahmatian and Philip T Metzger. "Soil test apparatus for lunar surfaces". In: *Earth and Space 2010: Engineering, Science, Construction, and Operations in Challenging Environments*. 2010, pp. 239–253.

[47] JY Wong. "Predicting the performances of rigid rover wheels on extraterrestrial surfaces based on test results obtained on earth". In: *Journal of Terramechanics* 49.1 (2012), pp. 49–61.

[48] Taizo Kobayashi et al. "Mobility performance of a rigid wheel in low gravity environments". In: *Journal of Terramechanics* 47.4 (2010), pp. 261–274.

[49] Ya Zhao et al. "DEM study on the discharge characteristics of lognormal particle size distributions from a conical hopper". In: *AIChE Journal* 64.4 (2018), pp. 1174–1190.

[50] Yongzhi Zhao et al. "Simulation and modeling of segregating rods in quasi-2D bounded heap flow". In: *AIChE Journal* 64.5 (2018), pp. 1550–1563.

[51] Siying Liu and Joseph J McCarthy. "Validating granular segregation rate models". In: *AIChE Journal* 63.9 (2017), pp. 3756–3763.

[52] H Katsuragi, K Anki Reddy, and K Endo. "Shape dependence of resistance force exerted on an obstacle placed in a gravity-driven granular silo flow". In: *AIChE Journal* (2018).

[53] AbdulMobeen Faqih et al. "Flow-induced dilation of cohesive granular materials". In: *AIChE journal* 52.12 (2006), pp. 4124–4132.

[54] Yanjie Li, Yong Xu, and Shengyao Jiang. "DEM simulations and experiments of pebble flow with monosized spheres". In: *Powder technology* 193.3 (2009), pp. 312–318.

[55] Yanjie Li, Yong Xu, and Colin Thornton. "A comparison of discrete element simulations and experiments for 'sandpiles' composed of spherical particles". In: *Powder Technology* 160.3 (2005), pp. 219–228.

[56] Miguel Florian-Algarin and Rafael Méndez. "Blend uniformity and powder phenomena inside the continuous tumble mixer using DEM simulations". In: *AIChE Journal* 61.3 (2015), pp. 792–801.

[57] Sushil S Shirsath et al. "Simulation study of the effect of wall roughness on the dynamics of granular flows in rotating semicylindrical chutes". In: *AIChE journal* 61.7 (2015), pp. 2117–2135.

[58] Watson L Vargas et al. "Suppressing the segregation of granular mixtures in rotating tumblers". In: *AIChE journal* 54.12 (2008), pp. 3124–3132.

[59] Shiliang Yang et al. “DEM study of granular flow characteristics in the active and passive regions of a three-dimensional rotating drum”. In: *AIChE Journal* 62.11 (2016), pp. 3874–3888.

[60] Brenda Remy et al. “Experiments and simulations of cohesionless particles with varying roughness in a bladed mixer”. In: *Chemical Engineering Science* 65.16 (2010), pp. 4557–4571.

[61] OS Sudah et al. “Simulation and experiments of mixing and segregation in a tote blender”. In: *AIChE Journal* 51.3 (2005), pp. 836–844.

[62] Atul Dubey, Aditya U Vanarase, and Fernando J Muzzio. “Impact of process parameters on critical performance attributes of a continuous blender—A DEM-based study”. In: *AIChE Journal* 58.12 (2012), pp. 3676–3684.

[63] Brenda Remy, Johannes G Khinast, and Benjamin J Glasser. “Discrete element simulation of free flowing grains in a four-bladed mixer”. In: *AIChE Journal* 55.8 (2009), pp. 2035–2048.

[64] Sandesh Kamath et al. “Flow of granular matter in a silo with multiple exit orifices: Jamming to mixing”. In: *Physical Review E* 90.6 (2014), p. 062206.

[65] L Orefice and JG Khinast. “DEM study of granular transport in partially filled horizontal screw conveyors”. In: *Powder Technology* 305 (2017), pp. 347–356.

[66] Justin W Fernandez, Paul W Cleary, William McBride, et al. “Effect of screw design on hopper draw down by a horizontal screw feeder”. In: *Seventh International Conference on CFD in the Minerals and Process Indistries*. 2009.

[67] Philip J Owen and Paul W Cleary. “Screw conveyor performance: comparison of discrete element modelling with laboratory experiments”. In: *Progress in Computational Fluid Dynamics, An International Journal* 10.5-6 (2010), pp. 327–333.

[68] PJ Owen and PW Cleary. “Prediction of screw conveyor performance using the Discrete Element Method (DEM)”. In: *Powder Technology* 193.3 (2009), pp. 274–288.

[69] QF Hou, KJ Dong, and AB Yu. “DEM study of the flow of cohesive particles in a screw feeder”. In: *Powder Technology* 256 (2014), pp. 529–539.

[70] D Kretz et al. “Discrete element method (DEM) simulation and validation of a screw feeder system”. In: *Powder Technology* 287 (2016), pp. 131–138.

[71] Johannes Quist and Carl Magnus Evertsson. "Cone crusher modelling and simulation using DEM". In: *Minerals Engineering* 85 (2016), pp. 92–105.

[72] Michele Marigo and Edmund Hugh Stitt. "Discrete element method (DEM) for industrial applications: Comments on calibration and validation for the modelling of cylindrical pellets". In: *KONA Powder and Particle Journal* 32 (2015), pp. 236–252.

[73] S González et al. "Forced axial segregation in axially inhomogeneous rotating systems". In: *Physical Review E* 92.2 (2015), p. 022202.

[74] Alessandro Leonardi et al. "Granular-front formation in free-surface flow of concentrated suspensions". In: *Physical Review E* 92.5 (2015), p. 052204.

[75] Umberto D'ortona et al. "Influence of rough and smooth walls on macroscale flows in tumblers". In: *Physical Review E* 92.6 (2015), p. 062202.

[76] Umberto D'Ortona, Nathalie Thomas, and Richard M Lueptow. "Influence of rough and smooth walls on macroscale granular segregation patterns". In: *Physical Review E* 93.2 (2016), p. 022906.

[77] Sandip Mandal and D Khakhar. "Sidewall-friction-driven ordering transition in granular channel flows: Implications for granular rheology". In: *Physical Review E* 96.5 (2017), p. 050901.

[78] Tom Leblicq et al. "Discrete element modelling of bendable tubes". In: *International Journal of Mechanical Sciences* 94 (2015), pp. 75–83.

[79] Piotr M Pieczywek and Artur Zdunek. "Compression simulations of plant tissue in 3D using a mass-spring system approach and discrete element method". In: *Soft matter* 13.40 (2017), pp. 7318–7331.

[80] Y Guo et al. "Discrete element simulation studies of angles of repose and shear flow of wet, flexible fibers". In: *Soft matter* 14.15 (2018), pp. 2923–2937.

[81] Eric JR Parteli and Thorsten Pöschel. "Particle-based simulation of powder application in additive manufacturing". In: *Powder Technology* 288 (2016), pp. 96–102.

[82] Haohui Xin, WaiChing Sun, and Jacob Fish. "Discrete element simulations of powder-bed sintering-based additive manufacturing". In: *International Journal of Mechanical Sciences* 149 (2018), pp. 373–392.

[83] Ryuta Yoshimatsu et al. "Field driven charging dynamics of a fluidized granular bed". In: *Soft matter* 12.29 (2016), pp. 6261–6267.

[84] Xiuhong Li et al. "Study on polyurethane media for mass finishing process: Dynamic characteristics and performance". In: *International Journal of Mechanical Sciences* 138 (2018), pp. 250–261.

[85] Wenwei Liu et al. "Adhesive loose packings of small dry particles". In: *Soft Matter* 11.32 (2015), pp. 6492–6498.

[86] Marc Z Miskin and Heinrich M Jaeger. "Evolving design rules for the inverse granular packing problem". In: *Soft Matter* 10.21 (2014), pp. 3708–3715.

[87] Haiyang Zhao et al. "Attenuation of pressure dips underneath piles of spherocylinders". In: *Soft matter* 14.21 (2018), pp. 4404–4410.

[88] Felix Verbücheln, Eric JR Parteli, and Thorsten Pöschel. "Helical inner-wall texture prevents jamming in granular pipe flows". In: *Soft matter* 11.21 (2015), pp. 4295–4305.

[89] Arman Pazouki et al. "Compliant contact versus rigid contact: A comparison in the context of granular dynamics". In: *Physical Review E* 96.4 (2017), p. 042905.

[90] C Windows-Yule and DJ Parker. "Center of mass scaling in three-dimensional binary granular systems". In: *Physical Review E* 89.6 (2014), p. 062206.

[91] C Windows-Yule, GJM Douglas, and DJ Parker. "Competition between geometrically induced and density-driven segregation mechanisms in vibrofluidized granular systems". In: *Physical Review E* 91.3 (2015), p. 032205.

[92] François Guillard, Yoël Forterre, and Olivier Pouliquen. "Origin of a depth-independent drag force induced by stirring in granular media". In: *Physical Review E* 91.2 (2015), p. 022201.

[93] Nathalie Thomas and Umberto D'ortona. "Evidence of reverse and intermediate size segregation in dry granular flows down a rough incline". In: *Physical Review E* 97.2 (2018), p. 022903.

[94] Stanislav Parez, Einat Aharonov, and Renaud Toussaint. "Unsteady granular flows down an inclined plane". In: *Physical Review E* 93.4 (2016), p. 042902.

[95] Laure Lemrich et al. "Dynamic induced softening in frictional granular materials investigated by discrete-element-method simulation". In: *Physical Review E* 96.6 (2017), p. 062901.

[96] Hendrik Otto et al. “CFD–DEM simulation and experimental investigation of the flow behavior of lunar regolith JSC-1A”. In: *Particuology* (2018).

[97] Jerome B Johnson et al. “Analysis of Mars Exploration Rover wheel mobility processes and the limitations of classical terramechanics models using discrete element method simulations”. In: *Journal of Terramechanics* 73 (2017), pp. 61–71.

[98] Viktor Milkevych et al. “Modelling approach for soil displacement in tillage using discrete element method”. In: *Soil and Tillage Research* 183 (2018), pp. 60–71.

[99] Mustafa Ucgul, John M Fielke, and Chris Saunders. “Defining the effect of sweep tillage tool cutting edge geometry on tillage forces using 3D discrete element modelling”. In: *Information Processing in Agriculture* 2.2 (2015), pp. 130–141.

[100] Dhaval Kumar A Patel, Bhavesh P Patel, and Mehul Kumar A Pate. “A critical review on kinematics of hydraulic excavator backhoe attachment”. In: *International Journal of Mechanical Engineering and Robotics Research* 4.2 (2015), p. 188.

[101] Mohammed Khair Al-Solihat and Meyer Nahon. “Flexible multibody dynamic modeling of a floating wind turbine”. In: *International Journal of Mechanical Sciences* 142 (2018), pp. 518–529.

[102] OA Kudryavtsev and SB Sapozhnikov. “Numerical simulations of ceramic target subjected to ballistic impact using combined DEM/FEM approach”. In: *International Journal of Mechanical Sciences* 114 (2016), pp. 60–70.

[103] Barthelemy Harthong et al. “Contact impingement in packings of elastic–plastic spheres, application to powder compaction”. In: *International Journal of Mechanical Sciences* 61.1 (2012), pp. 32–43.

[104] CJ Coetzee. “Calibration of the discrete element method and the effect of particle shape”. In: *Powder Technology* 297 (2016), pp. 50–70.

[105] Rahul Bharadwaj, William R Ketterhagen, and Bruno C Hancock. “Discrete element simulation study of a Freeman powder rheometer”. In: *Chemical Engineering Science* 65.21 (2010), pp. 5747–5756.

[106] CJ Coetzee. “Particle upscaling: Calibration and validation of the discrete element method”. In: *Powder Technology* 344 (2019), pp. 487–503.

[107] Mustafa Ucgul, John M Fielke, and Chris Saunders. "Three-dimensional discrete element modelling of tillage: Determination of a suitable contact model and parameters for a cohesionless soil". In: *Biosystems Engineering* 121 (2014), pp. 105–117.

[108] Mustafa Ucgul, John M Fielke, and Chris Saunders. "Three-dimensional discrete element modelling (DEM) of tillage: Accounting for soil cohesion and adhesion". In: *Biosystems Engineering* 129 (2015), pp. 298–306.

[109] Mustafa Ucgul, Chris Saunders, and John M Fielke. "Discrete element modelling of tillage forces and soil movement of a one-third scale mouldboard plough". In: *Biosystems Engineering* 155 (2017), pp. 44–54.

[110] Jerome B Johnson et al. "Discrete element method simulations of Mars Exploration Rover wheel performance". In: *Journal of Terramechanics* 62 (2015), pp. 31–40.

[111] Richard A Schultz. "Brittle strength of basaltic rock masses with applications to Venus". In: *Journal of Geophysical Research: Planets* 98.E6 (1993), pp. 10883–10895.

[112] Kamran Kardel et al. "Experimental and theoretical modeling of behavior of 3d-printed polymers under collision with a rigid rod". In: *Additive Manufacturing* 14 (2017), pp. 87–94.

[113] Marie Violay et al. "Effect of glass on the frictional behavior of basalts at seismic slip rates". In: *Geophysical research letters* 41.2 (2014), pp. 348–355.

[114] Baishan Peng. "Rockfall trajectory analysis: Parameter determination and application". In: (2000).

[115] Mieczyslaw Gregory Bekker. *Theory of land locomotion*. University of Michigan Press, 1956.

[116] Mieczyslaw Gregory Bekker. *Introduction to Terrain-Vehicle Systems. Part I: The Terrain. Part II: The Vehicle*. Tech. rep. MICHIGAN UNIV ANN ARBOR, 1969.

[117] Mieczyslaw Gregory Bekker. "Mechanics of locomotion and lunar surface vehicle concepts". In: *Sae Transactions* (1964), pp. 549–569.

[118] Jo Yung Wong. *Theory of ground vehicles*. John Wiley & Sons, 2008.

[119] Francisco J Comin et al. "Trafficability assessment of deformable terrain through hybrid wheel-leg sinkage detection". In: *Journal of Field Robotics* 34.3 (2017), pp. 451–476.

[120] Alberto Gallina et al. "Parameter identification of a planetary rover wheel–soil contact model via a Bayesian approach". In: *Journal of Field Robotics* 31.1 (2014), pp. 161–175.

[121] Jeffrey Aguilar et al. "A review on locomotion robophysics: the study of movement at the intersection of robotics, soft matter and dynamical systems". In: *Reports on Progress in Physics* 79.11 (2016), p. 110001.

[122] Ryan D Maladen et al. "Undulatory swimming in sand: subsurface locomotion of the sandfish lizard". In: *science* 325.5938 (2009), pp. 314–318.

[123] Ryan D Maladen et al. "Mechanical models of sandfish locomotion reveal principles of high performance subsurface sand-swimming". In: *Journal of The Royal Society Interface* 8.62 (2011), pp. 1332–1345.

[124] Yang Ding et al. "Mechanics of undulatory swimming in a frictional fluid". In: *PLoS computational biology* 8.12 (2012), e1002810.

[125] Yang Ding, Nick Gravish, and Daniel I Goldman. "Drag induced lift in granular media". In: *Physical Review Letters* 106.2 (2011), p. 028001.

[126] Ross L Hatton et al. "Geometric visualization of self-propulsion in a complex medium". In: *Physical review letters* 110.7 (2013), p. 078101.

[127] Chen Li, Tingnan Zhang, and Daniel I Goldman. "A terradynamics of legged locomotion on granular media". In: *science* 339.6126 (2013), pp. 1408–1412.

[128] Tingnan Zhang and Daniel I Goldman. "The effectiveness of resistive force theory in granular locomotion". In: *Physics of Fluids* 26.10 (2014), p. 101308.

[129] Yasemin Ozkan Aydin et al. "Geometric Mechanics Applied to Tetrapod Locomotion on Granular Media". In: *Conference on Biomimetic and Biohybrid Systems*. Springer. 2017, pp. 595–603.

[130] Ken Kamrin. "Nonlinear elasto-plastic model for dense granular flow". In: *International Journal of Plasticity* 26.2 (2010), pp. 167–188.

[131] Sachith Dunatunga and Ken Kamrin. "Continuum modelling and simulation of granular flows through their many phases". In: *Journal of Fluid Mechanics* 779 (2015), pp. 483–513.

[132] Sachith Dunatunga and Ken Kamrin. "Continuum modeling of projectile impact and penetration in dry granular media". In: *Journal of the Mechanics and Physics of Solids* 100 (2017), pp. 45–60.

[133] Hesam Askari and Ken Kamrin. "Intrusion rheology in grains and other flowable materials". In: *Nature materials* 15.12 (2016), p. 1274.

[134] James Slonaker et al. "General scaling relations for locomotion in granular media". In: *Physical Review E* 95.5 (2017), p. 052901.

[135] Baptiste Darbois Texier, Alejandro Ibarra, and Francisco Melo. "Helical Locomotion in a Granular Medium". In: *Physical review letters* 119.6 (2017), p. 068003.

[136] Rogelio Valdés et al. "Self-propulsion of a helical swimmer in granular matter". In: *Physical Review Fluids* 4.8 (2019), p. 084302.

[137] Chemical Rubber Company. *Handbook of tables for applied engineering science*. Chemical Rubber Company, 1970.

[138] BM Tymrak, M Kreiger, and Joshua M Pearce. "Mechanical properties of components fabricated with open-source 3-D printers under realistic environmental conditions". In: *Materials & Design* 58 (2014), pp. 242–246.

[139] Carsten Güttler et al. "Normal collisions of spheres: A literature survey on available experiments". In: *arXiv preprint arXiv:1204.0001* (2012).

[140] Samuel F Foerster et al. "Measurements of the collision properties of small spheres". In: *Physics of Fluids* 6.3 (1994), pp. 1108–1115.

[141] YC Zhou et al. "Rolling friction in the dynamic simulation of sandpile formation". In: *Physica A: Statistical Mechanics and its Applications* 269.2-4 (1999), pp. 536–553.

[142] ASTM G194-08. *Standard Test Method for Measuring Rolling Friction Characteristics of a Spherical Shape on a Flat Horizontal Plane*. Tech. rep. ASTM, 2013.

[143] David Carrington Motley. "Physical experimentation and actuated wheel design for granular locomotion using Resistive Force Theory". PhD thesis. Massachusetts Institute of Technology, 2016.

[144] RY Yang et al. "DEM simulation of the flow of grinding media in IsaMill". In: *Minerals Engineering* 19.10 (2006), pp. 984–994.

[145] Nicolas Taberlet et al. "On axial segregation in a tumbler: an experimental and numerical study". In: *Journal of Statistical Mechanics: Theory and Experiment* 2006.07 (2006), P07013.

[146] RL Stewart et al. "Simulated and measured flow of granules in a bladed mixer—a detailed comparison". In: *Chemical Engineering Science* 56.19 (2001), pp. 5457–5471.

[147] Ebrahim Alizadeh, Francois Bertrand, and Jamal Chaouki. "Comparison of DEM results and Lagrangian experimental data for the flow and mixing of granules in a rotating drum". In: *AIChE Journal* 60.1 (2014), pp. 60–75.

[148] Stef Lommen, Dingena Schott, and Gabriel Lodewijks. "DEM speedup: Stiffness effects on behavior of bulk material". In: *Particuology* 12 (2014), pp. 107–112.

[149] Andrew Thoesen, Sierra Ramirez, and Hamid Marvi. "Screw-generated forces in granular media: Experimental, computational, and analytical comparison". In: *AIChE Journal* 65.3 (2019), pp. 894–903.

[150] Xiuzhi Wang et al. "Vibratory finishing co-simulation based on ADAMS-EDEM with experimental validation". In: *The International Journal of Advanced Manufacturing Technology* 96.1-4 (2018), pp. 1175–1185.

[151] YE Ko and CK Song. "Vehicle modeling with nonlinear tires for vehicle stability analysis". In: *International Journal of Automotive Technology* 11.3 (2010), pp. 339–344.

[152] Xue Jun Wang et al. "The research of the numerical simulation on the granular ballast bed tamping". In: *Advanced Materials Research*. Vol. 479. Trans Tech Publ. 2012, pp. 1395–1398.

[153] Robin Briend, Peter Radziszewski, and Damiano Pasini. "Virtual soil calibration for wheel–soil interaction simulations using the discrete-element method". In: *Canadian Aeronautics and Space Journal* 57.1 (2011), pp. 59–64.

[154] YC Chung and JY Ooi. "Confined compression and rod penetration of a dense granular medium: discrete element modelling and validation". In: *Modern Trends in Geomechanics*. Springer, 2006, pp. 223–239.

[155] Scott Moreland et al. "Soil behavior of wheels with grousers for planetary rovers". In: *2012 IEEE Aerospace Conference*. IEEE. 2012, pp. 1–8.

[156] Scott Jared Moreland. "Traction Processes of Wheels on Loose, Granular Soil". PhD thesis. Doctoral Dissertation, Carnegie Mellon University, 2013.

[157] Krzysztof Skonieczny, Scott J Moreland, and David S Wettergreen. "A grouser spacing equation for determining appropriate geometry of planetary rover wheels". In: *2012 IEEE/RSJ International Conference on Intelligent Robots and Systems*. IEEE. 2012, pp. 5065–5070.

[158] Mark E Rentschler, Shane M Farritor, and Karl D Iagnemma. "Mechanical design of robotic in vivo wheeled mobility". In: *Journal of Mechanical Design* 129.10 (2007), pp. 1037–1045.

[159] Hiroaki Inotsume, Krzysztof Skonieczny, and David S Wettergreen. "Analysis of grouser performance to develop guidelines for design for planetary rovers". In: *Proceedings of the 12th International Symposium on Artificial Intelligence, Robotics and Automation in Space (i-SAIRAS 2014)*. 2014.

[160] Andrew Thoesen et al. "Revisiting Scaling Laws for Robotic Mobility in Granular Media (Under Review)". In: *2020 IEEE International Conference on Robotics and Automation (ICRA)*. IEEE. 2020, pp. 1–6.

[161] PBS Lissaman. "Low-Reynolds-number airfoils". In: *Annual review of fluid mechanics* 15.1 (1983), pp. 223–239.

[162] Andrew Thoesen, Teresa McBryan, and Hamidreza Marvi. "Helically-driven granular mobility and gravity-variant scaling relations". In: *RSC advances* 9.22 (2019), pp. 12572–12579.

[163] Andrew Thoesen, Sierra Ramirez, and Hamid Marvi. "Screw-Powered Propulsion in Granular Media: An Experimental and Computational Study". In: *2018 IEEE International Conference on Robotics and Automation (ICRA)*. IEEE. 2018, pp. 1–6.

[164] Gareth Meirion-Griffith and Matthew Spenko. "A New Pressure-Sinkage Model for Small, Rigid Wheels on Deformable Terrains". In: *Proceedings of the Joint 9th Asia-Pacific ISTVS Conference and Annual Meeting of Japanese Society for Terramechanics Sapporo, Japan, September*. Vol. 27. 2003.

[165] Andrew Thoesen et al. "Predictive Performance of Granular Scaling Laws for Lightweight Rovers (Under Review)". In: IEEE. 2019.

APPENDIX A

MATHEMATICAL MODEL OF AN ARCHIMEDES SCREW WITH CARTESIAN COORDINATES

To address the forces of granular media on a uniform Archimedes screw with analytical methods, it first becomes necessary to define the screw in Cartesian space to describe its motion. To be more specific mathematically, we are using a right-handed helicoid. The equation of a helicoid is given by defining the Cartesian coordinates with their parameterized counterparts:

$$x = \ r\cos(\theta) \quad y = \ r\sin(\theta) \ z = \ p\theta \tag{A.1}$$

This defines the x, y, z coordinates based on the radius of the helix, the chosen pitch, and the rotation with respect to the z-axis. We are then able to define the center locations of discretized plates as shown in 49. With the surface curvature defined by the coordinates, as well as location, we can determine the direction of the normals. We obtain the normal vectors for the primary planes by using the respective Jacobian of each component:

$$J_x = \begin{vmatrix} \partial y/\partial r & \partial z/\partial r \\ \partial y/\partial \theta & \partial z/\partial \theta \end{vmatrix} = psin(\theta) \tag{A.2}$$

$$J_y = \begin{vmatrix} \partial z/\partial r & \partial x/\partial r \\ \partial z/\partial \theta & \partial x/\partial \theta \end{vmatrix} = -pcos(\theta) \tag{A.3}$$

$$J_z = \begin{vmatrix} \partial x/\partial r & \partial y/\partial r \\ \partial x/\partial \theta & \partial y/\partial \theta \end{vmatrix} = r \tag{A.4}$$

From the magnitude of the normal vectors in eq(A.5), the unit normal vectors are then developed. These are the direction cosines for the surface normals. These are the cosines of the angle away from a primary axis. For instance, if $z_n = 1$, then its angle away from the z-axis is 0; it is aligned entirely on the z-axis. The x_n and y_n would then be 0, and their respective angles 90° because the normal vector is perpendicular to both directions.

$$L = \sqrt{psin(\theta)^2 \ + pcos(\theta)^2 \ + r^2} = \ \sqrt{p^2 \ + r^2} \tag{A.5}$$

$$x_n = \frac{psin(\theta)}{\sqrt{p^2 \ + r^2}} \quad y_n = \frac{-pcos(\theta)}{\sqrt{p^2 \ + r^2}} \quad z_n = \frac{r}{\sqrt{p^2 \ + r^2}} \tag{A.6}$$

In 49, the normal vectors of a target helix have been generated and laid over a CAD model for verification.

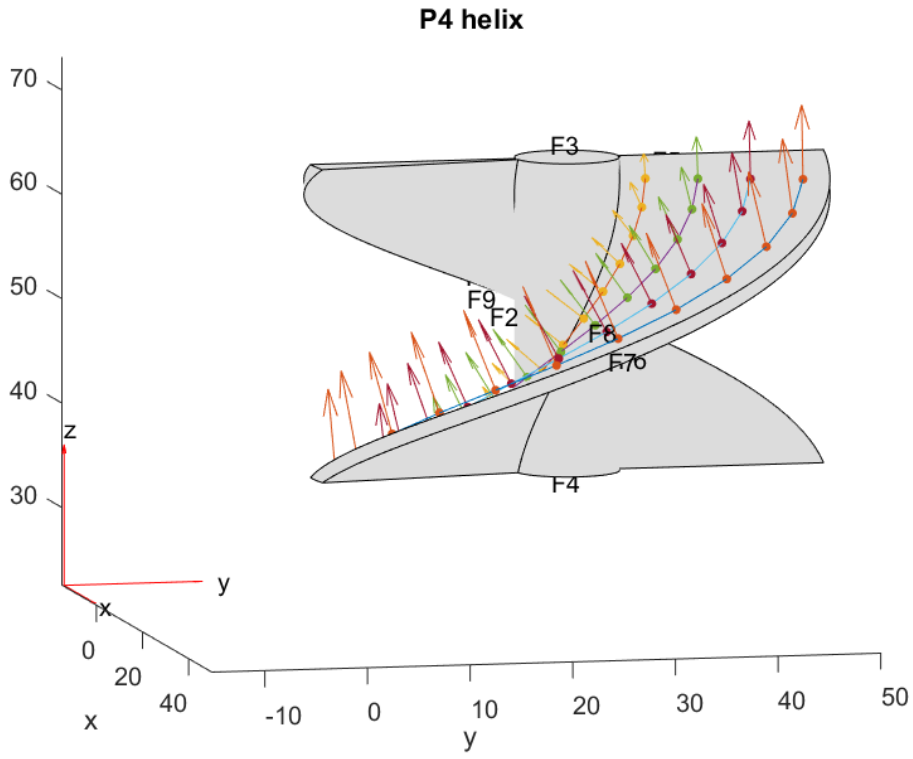

Figure 49. Normal vectors of helix paths are laid over a CAD model

A.0.1 Applying the RFT Model

The equations for resistive force theory [127] are simplified below. β and γ are the angle of a horizontal plate away from the horizontal plane, and the angle of attack of velocity from the horizontal plane, respectively. These angles are evaluated from a perspective defined by assuming a horizontal screw pushing material sideways. While the screw rotates, the material sees a sideways movement in small, discrete timesteps. In this fashion, $\gamma = 0$ consistently. β of each plate varies depending on the position around the screw radially. z_n, therefore, determines how our approximated plates are tilted towards the main axis of the screw. This happens in a radial fashion around the screw axis and our evaluation relies on a key assumption from later work [133] in

testing granular intruders: that horizontal tilting of an intruder's orientation results in similar forces to vertical tilting of an intruder's orientation. If there is sideways motion, then β applied to pitch or yaw produces roughly similar forces in that axial direction.

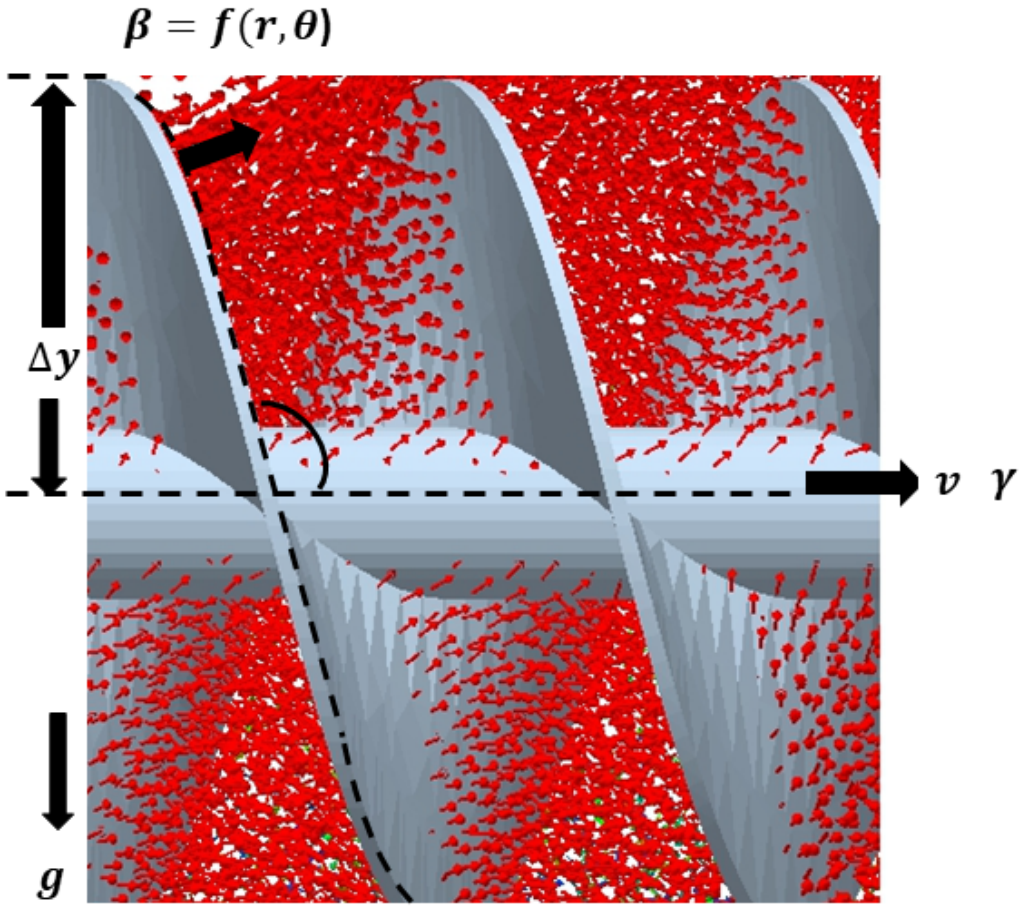

Figure 50. Reinterpretation of the plate superposition equations using two dimensional approximation of three dimensional helical intruder

Two α parameters, which are the depth-independent, pressure factors for each section in both an axial and outward direction are functions of these angles. Since $\gamma = 0$, the equations from the resistive force theory [127] for α simplify to those below

$$\alpha_{i,Outward} = A_{00} + A_{10}\cos(2\beta) \ + B_{11}\sin(2\beta) \ + B_{-11}\sin(-2\beta) \tag{A.7}$$

$$\alpha_{i,Thrust} = C_{11}\cos(2\beta) \ + C_{01} + D_{11}\sin(2\beta) \tag{A.8}$$

These α are then multiplied by the respective surface areas for each plate, leading to the depth-independent force. The results are multiplied by their respective depth with matrices and summed:

$$F_{Thrust} = \sum \overline{\alpha}_{i,\ Thrust} * \overline{A}_i \tag{A.9}$$

$$F_{Outwards} = \sum \ \overline{\alpha}_{i,\ Outwards} * \overline{A}_i \tag{A.10}$$

We also explored how discretizing plates may affect the results. The MATLAB code was tested at discretized plate dimensions of 1-5 mm sides with no difference observed in the estimated forces.